



**Universität Hamburg**

**DER FORSCHUNG | DER LEHRE | DER BILDUNG**

# Biodegradable Nanoassemblies for Biomedical Applications

**Dissertation**

zur Erlangung des Doktorgrades

an der Fakultät für Mathematik, Informatik und

Naturwissenschaften

Fachbereich Chemie

der Universität Hamburg

vorgelegt von

M.Sc. Miao Feng

- Hamburg, 2024



GUTACHTER DER DISSERTATION:

Prof. Dr.Wolfgang J. Parak

Prof. Dr.Nils Huse

MITGLIEDER DER PRÜFUNGSKOMMISSION:

Prof. Dr.Wolfgang J. Parak

Prof.Dr.Tobias Beck

Prof.Dr.Wolfgang Maison

DATUM DER DISPUTATION: 21.06.24

LEITER DES FACHBEREICHS PHYSIK:

Prof. Dr. Markus Fischer

DEKAN DER MIN-FAKULTÄT:

Prof. Dr.-Ing. Norbert Ritter



## Bibliography

<b>Personal information</b>			
Name	Miao	Family name	Feng
Birthplace	Baiyin, Guansu, China	Nationality	Chinese
<b>Education</b>			
12.2020-03.2024	University of Hamburg, AG Biophotonics (Prof. Dr. Wolfgang J. Parak), Germany		
	Doctor of Natural Sciences		
09.2017-06.2020	Xidian University, China		
	Master of Science		
09.2013-06.2017	Soochow university, China		
	Bachelor of Engineering		



## **Abstract**

Degradable drug delivery carriers hold immense research value and promising application prospects in tumor therapy. The development of nanoparticles aims to overcome the limitations of therapeutic efficacy. As inorganic nanoparticles, polymer vesicles, and liposomes are increasingly tailored in specific designs, they exhibit more personalized approaches to drug transportation, where the delivery efficiency of nanodelivery systems determines the clinical efficacy of cancer treatment and diagnosis.

While smaller nanoparticles penetrate deeper into the tumor sites, they exhibit poorer retention ability, whereas larger nanoparticles tend to accumulate around tumor blood vessels, but have limited penetration ability. If a nanodelivery system can achieve both high permeability and prolonged retention simultaneously, the efficiency of drug delivery would be significantly amplified. Inspired by this concept, we developed a strategy that combines small nanoparticles into larger biodegradable nanocomponents, harnessing the benefits of both larger and smaller nanoparticles.

This thesis primarily focuses on the design and construction of various degradable nanodelivery systems, and quantitatively comparing the delivery efficiency of biodegradable nanocomponents with free nanoparticles at tumor sites. We synthesized gold nanoclusters by cationic polymer mediated self-assembly which forms particles of approximately 100 nm to validate this concept. Extensive characterization of monodispersed and positively charged nanoparticles reveals pH-dependent swelling properties, strong fluorescence enhancement, and excellent colloidal stability and photostability in water, buffer solutions, and culture media. In vitro studies on Hela cells demonstrate significantly enhanced absorption of composite nanoparticles within the endocytic compartment compared to free Au NPs(1.7 nm). In contrast to extracellular excretion with equivalent cellular gold content, the rate of "escape" of free Au NPs(1.7

nm) from cells is higher than that of composite particles. ICP-MS measurements confirms a 5.6-fold enhancement in cellular uptake of gold elements compared to free Au NPs(1.7 nm), thereby achieving enhanced cell drug transportation combined with efficient fluorescence detection. Furthermore, we observe the degradation of nanoparticles within cells and subsequent fluorescence release using two-photon fluorescence microscopy. Nano-composite particles encapsulating quantum dots/FITC are synthesized, and upon cellular uptake of these composite nanoparticles, initially red quantum dots and green fluorescent molecules co-localized within cells. However, as the nanoparticles degrade within lysosomes, the fluorescence moieties embedded in the polymer matrix no longer co-localize with the quantum dots encapsulated in the composite nanoparticles. With this design we can compare the different intracellular fates of autofluorescent nanoparticles and fluorescent molecules. In conclusion, our study presents a novel strategy of combining small nanoparticles into larger biodegradable nanocomponents to capitalize on the advantages of both larger and smaller sized nanoparticles. This approach holds significant promise for enhancing drug delivery efficiency in tumor therapy.



## Zusammenfassung

Abbaubare Wirkstoffträger haben einen immensen Forschungswert und vielversprechende Anwendungsaussichten in der Tumorthherapie. Die Entwicklung von Nanopartikeln zielt darauf ab, die Einschränkungen der therapeutischen Wirksamkeit zu überwinden. Da anorganische Nanopartikel, Polymervesikel und Liposomen zunehmend spezifisch gestaltet werden, zeigen sie personalisiertere Ansätze für den Wirkstofftransport, wobei die Effizienz der Nanoliefersysteme die klinische Wirksamkeit der Krebsbehandlung und -diagnose bestimmt. Während kleinere Nanopartikel tiefer in die Tumorstellen eindringen, zeigen sie eine geringere Retentionsfähigkeit, während größere Nanopartikel dazu neigen, sich um Tumorblutgefäße anzusammeln, jedoch eine begrenzte Penetrationsfähigkeit haben. Wenn ein Nanoliefersystem gleichzeitig hohe Permeabilität und verlängerte Retention erreichen kann, würde die Effizienz der Wirkstoffabgabe signifikant erhöht werden. Inspiriert von diesem Konzept haben wir eine Strategie entwickelt, die kleine Nanopartikel in größere bioabbaubare Nanokomponenten kombiniert und die Vorteile sowohl größerer als auch kleinerer Nanopartikel nutzt.

Diese Arbeit konzentriert sich hauptsächlich auf das Design und den Aufbau verschiedener abbaubarer Nanoliefersysteme und vergleicht quantitativ die Effizienz der Wirkstoffabgabe von bioabbaubaren Nanokomponenten mit freien Nanopartikeln an Tumorstellen. Zunächst synthetisierten wir Gold-Nanocluster durch kationische Polymer-vermittelte Selbstorganisation, bei der Partikel von etwa 100 nm Größe entstehen, um das Konzept zu validieren. Eine umfangreiche Charakterisierung von monodispersen und positiv geladenen Nanopartikeln zeigt pH-abhängige Quelleigenschaften, starke Fluoreszenzverstärkung sowie ausgezeichnete kolloidale Stabilität und Photostabilität in Wasser, Pufferlösungen und Kulturmedien. In-vitro-Studien an Hela-Zellen zeigen eine

signifikant verbesserte Aufnahme von KompositNanopartikel im endozytischen Kompartiment im Vergleich zu freien Au NPs(1.7 nm). Im Gegensatz zur extrazellulären Ausscheidung mit gleichwertigem zellulären Goldgehalt ist die Rate des "Ausbruchs" von freien Au NPs(1.7 nm) aus den Zellen höher als die von KompositNanopartikel. ICP-MS-Messungen bestätigen eine 5,6-fache Verbesserung der zellulären Aufnahme von Gold gegenüber freien Au NPs(1.7 nm) und erreichen so einen verbesserten zellulären Wirkstofftransport in Kombination mit effizienter Fluoreszenzdetektion. Darüber hinaus beobachten wir die Degradation von Nanopartikeln innerhalb von Zellen und anschließende Fluoreszenzfreisetzung unter Verwendung der Zwei-Photonen-Fluoreszenzmikroskopie. Nano-Komposit-Partikel, die Quantenpunkte/FITC umschließen, werden synthetisiert, und nach der zellulären Aufnahme dieser Komposit-Nanopartikel sind anfangs rote Quantenpunkte und grüne fluoreszierende Moleküle innerhalb von Zellen kollokalisiert. Wenn sich die Nanopartikel jedoch in den Lysosomen abbauen, werden die in der Polymermatrix eingebetteten kollokalisieren die Fluoreszenzmoieties, die in der Polymermatrix eingebettet sind, nicht mehr mit den in den Komposit-Nanopartikeln eingeschlossenen Quantenpunkten. Mit diesem Design können wir die verschiedenen intrazellulären Schicksale von autofluoreszenten Nanopartikeln und fluoreszierenden Molekülen vergleichen. Zusammenfassend präsentiert unsere Studie eine neuartige Strategie, kleine Nanopartikel in größere bioabbaubare Nanokomponenten zu kombinieren, um die Vorteile sowohl größerer als auch kleinerer Nanopartikel zu nutzen. Dieser Ansatz birgt ein signifikantes Potenzial zur Verbesserung der Wirkstoffabgabeffizienz in der Tumorthherapie.

## Table of Contents

Bibliography .....	i
Abstract.....	iii
Zusammenfassung .....	v
Abbreviations .....	xi
1.Scope of the Work.....	1
2. Introduction .....	3
2.1. The Rise of Nanomedicine .....	4
2.2. “EPR” Effect of Nanomedicine .....	5
2.3. Classification of Nanomedicine Carriers .....	7
2.3.1. Micellar Carriers.....	7
2.3.2. Lipid Nanoparticles (LNPs) .....	8
2.3.3. Inorganic Material Nanocarriers .....	11
2.4. Various properties influence the fate of nanomedicines.....	16
2.4.1. Size Effects .....	16
2.4.2. Morphology Effects.....	16
2.4.3. Surface Potential Effects .....	17
3. Motivation.....	19
4. The Main Research Content .....	21
4.1. Innovative Strategy of Highly Permeable and Highly Deliverable Nanomedicine Based on Gold Nanoparticles.....	21
4.2. Quantum Dots and FITC Labelled Nanocomposite as a Platform for Biodegradation Studies.....	22
5. Quantification of improved delivery and clearance of nanoparticles due to endosomal/lysosomal degradation .....	23
5.1. Introduction.....	23
5.2. Major Reagents.....	24
5.3 Key Instruments.....	26

5.4. Experiments and Methods.....	27
5.4.1. Synthesis of 100 nm PMA-coated Au Nanoparticles (Au NPs (100 nm)) .....	27
5.4.2. Synthesis of Gold Nanoclusters.....	28
5.4.3. Synthesis of Hybrid Structure with Gold Nanoclusters.....	28
5.4.4. Synthesis of Polyelectrolyte Capsule-AuNP(Au NPs (50 nm)@PSS/PAH) .....	29
5.4.5. Quantum Yield Measurements .....	30
5.4.6. Dynamic Contact Angle Measurement.....	31
5.4.7. Thermogravimetric Analysis.....	32
5.4.8. Cell Viability of Nanoparticles .....	33
5.5. Results and Discussions .....	33
5.5.1. Physicochemical Characterizations of NPs .....	34
5.5.2. Quantitative Analysis the Content of Au Elements .....	44
5.5.3. Cell Viability of Nanoparticles .....	47
5.5.4. Cell Proliferation upon Exposure to NPs .....	49
5.6. Endo and Exocytosis Studies Based on NPs with PSS/PAH Encapsulation using ICP-MS .....	51
5.6.1. Endocytosis Studies Quantification Inside the Cell Based on ICP-MS.....	51
5.6.2. Cell Exocytosis Studies Based on NPs with PSS/PAH encapsulation.....	55
5.7. Endo and Exocytosis Studies Based on NPs with PLAG encapsulation .....	56
5.7.1. Endocytosis Studies Based on NPs with PLAG encapsulation.....	56
5.7.2. Exocytosis Studies Were Conducted Using the Same Exposure Concentration .....	60
5.7.3. Exocytosis Studies Using the Different Exposure Concentration.....	63
5.8. Degradation Studies Using TEM.....	66
5.9. Summary.....	67
6. Quantum Dots and FITC Labelled Nanocomposite as a Platform for Biodegradation Studies .....	69
6.1. Introduction.....	69

6.2. Major Reagents.....	70
6.3. Key Instruments.....	72
6.4. Experiments and Methods.....	72
6.4.1. Synthesis of Hydrophobic CdSe@ZnS NPs.....	72
6.4.2. Synthesis of QDs/FITC@mPEG-PLGA NPs .....	74
6.4.3. Characterization of QDs@mPEG-PLGA NPs .....	75
6.4.4. Analyze the DLS Data Using DLS APP.....	75
6.4.5. pH-dependent Degradation of QDs/FITC@mPEG-PLGA NPs.....	76
6.4.6. Cell Culture and Cell Viability .....	76
6.4.7. Biodegradation by Laser Scanning Microscope .....	77
6.5. Results and Discussions .....	78
6.5.1. The Characterization of NPs.....	78
6.5.2. Colloidal Stability of Nanocomposite .....	83
6.5.3. Degradation Behaviors of QDs/FITC@mPEG-PLGA NPs Monitored by Fluorescence .....	86
6.5.4. TEM Evolution of NPs During the Degradation Process .....	88
6.5.5. Cell Viability of Nanocomposite .....	89
6.5.6. Bioimaging of Hela Cells Using NPs Nanocomposite .....	91
6.6. Summary.....	95
Appendix: .....	97
A1. Upconverting Nanoparticles.....	97
A.1.1. Synthesis of Tm-doped Upconversion Nanoparticles. ....	97
A.1.2. Surface Modification of Poly(isobutylene-alt-maleic anhydride) PMA .....	98
A.1.3. Characterization of Colloidal Properties .....	98
A.1.4. Results .....	99
List of Hazardous Substances .....	103
Acknowledgements.....	107
Reference .....	109

Eidesstattliche Versicherung/Declaration on Oath ..... 118

## Abbreviations

AuNPs	Gold Nanoparticles
Au NPs(1.7 nm)	Gold Nanoclusters
PEG <sub>2000</sub>	Polyethylene glycol 2000
HAuCl <sub>4</sub>	Tetrachloroauric acid
CaCO <sub>3</sub>	Calcium Carbonate
CTAB	Cetyltrimethylammonium Bromide
DMEM	Dulbecco's Modified Eagles Medium
DMSO	Dimethyl Sulfoxide
FITC	Fluorescein Isothiocyanate
HCl	Hydrogen Chloride
HNO <sub>3</sub>	Nitric Acid
LbL	Layer-by-Layer
NPs	Nanoparticles
PSS	Poly (styrene sulfonate)
PAH	Poly (allylamine hydrochloride)
PBS	Phosphate Buffered Saline
PMA	Poly(isobutylene-alt-maleic anhydride)
SiO <sub>2</sub>	Silicon Dioxide
UCNP	Upconverting Nanoparticles
SPR	Surface Plasmon Resonance
DDS	Drug Delivery Systems
MRI	Magnetic Resonance Imaging
Hela	Henrietta Lacks
PEG	Poly(ethylene glycol)

QDs	Quantum Dots
SPIONs	Super Paramagnetic Iron Oxide NPs
TEM	Transmission Electron Microscopy
SEM	Scanning Electron Microscopy
DLS	Dynamic Light Scattering
DDA	Dodecyl amine
DSA	Drop Shape Analysis
GSH	L-glutathione
QY	Quantum Yields
CA	Contact Angle
SSA	Specific Surface Area
DDT	1- dodecanethiol
TGA	Thermogravimetric Analysis
BSA	Bovine Serum Albumin
TOPO	Trioctylphosphine Oxide
TOPSe	Trioctylphosphine Selenide
HPA	Hexylphosphonic Acid
FRET	Förster Resonance Energy Transfer
PVA	Polyvinyl Alcohol
InAs	Indium Arsenide
ZnS	Zinc Sulfide
CdSe	Cadmium Selenide
CdO	Cadmium Oxide
UV-Vis	Ultraviolet-visible Spectroscopy
MRI	Magnetic Resonance Imaging
SFE	Surface Free Energy



ODE	1-octadecene
kDa	Kilodalton
mm	Millimeters
nm	Nanometer
SSA	Specific Surface Area
PL	Photoluminescence
OA	Oleic Acid
NaCl	Sodium Chloride
μL	Microliter
mL	Milliliter
ICP-MS	Inductively Coupled Plasma Mass Spectrometry



## **1.Scope of the Work**

Due to the current efficiency issues in nanoparticle delivery systems, the main objective of our research work is to develop a more efficient potential approach for nanomedicine. Therefore, we have developed a biodegradable nanocomposite through an environmentally friendly synthesis method, which allows small-sized nanoparticles to be encapsulated within a degradable nano-framework. Additionally, by quantitatively characterizing the fate of nanoparticles inside cells, we can more accurately compare the delivery efficiency of nanoparticles with the same size but different structures and compositions, as well as free nanoparticles and nanocomposites. This can be achieved by synthesizing free nanoparticles, subsequently encapsulating them in biodegradable polymer materials, and comparing cellular uptake at the same exposure time under different concentrations. Understanding the delivery process and efficiency of nanoparticles is essential for any nanomedicine candidate. From this perspective, ICP-MS provides us with more accurate data on cellular uptake. Furthermore, achieving biodegradability is crucial for the future clinical applications of nanoparticle delivery systems. Using two-photon microscopy, we can observe the degradation process of the nanocomposites used in this study within cells over time. Our ultimate goal is to introduce potential candidates for nanomedical applications.



## 2. Introduction

The word “nanotechnology” was seeded by renowned physicist Richard Feynman in his talk “There is plenty of room at the bottom”, in which he described the possibility of synthesis via direct manipulation of atoms. In nature, there are some naturally occurring substances at the nanoscale, such as proteins, DNA molecules, and viruses. Due to their extremely small size, they are much smaller than the resolution of optical microscopes, making them invisible to the human eye or conventional microscopes. Taking the COVID-19 pandemic as an example, using the high affinity between the receptor-binding domain (RBD) of viral spike proteins and the ACE2 receptors on host cells, enveloped SARS-CoV-2 virus with a diameter of about 100 nm infects host cells[1]. The virus hijacks host cells and replicates more viral RNA through a series of membrane fusion processes to further propagate the infection. The currently widely used mRNA vaccines, with an average diameter of 100 nm, consist of lipid nanoparticles as the shell surrounding mRNA strands as the core[2]. These vaccines trigger an immune response in the body to help people fight against the virus which play a crucial role in ending the global pandemic. There are also some examples for the clinical use of NPs based on their intrinsic functionality. Superparamagnetic iron oxide NPs (SPIONs), which provide high contrast in magnetic resonance imaging (MRI)[3]. SPION-based contrast agent ferumoxytol (do not contain gadolinium), which provide contrast in the transverse relaxation time  $T_2$ [4]. Iron oxide NPs, which have capacity to convert incident light into local heat[5].

Nowadays, nanotechnology allows for the design of more complex NPs, in particular, hybrid materials integrating different functional incorporation. The promising prospects of organic/inorganic hybrids NPs in nanomedicine have inspired researcher to construct nano for drug delivery systems (DDS), gene transfection vehicles, and biomarker sensing detectors. Therefore, there is an urgent need to study the properties of existing

nanomaterials and explore novel functional nanomaterials and their applications in the fields of life sciences and chemical engineering.

## **2.1. The Rise of Nanomedicine**

The increasing interest in applying nanotechnology to cancer research is largely attributed to its unique and attractive functionalities in drug delivery, diagnosis and imaging, development of synthetic vaccines, and miniature medical devices. Additionally, certain nanomaterials possess therapeutic properties in themselves, further enhancing their potential in cancer treatment[6]. Therapeutic drugs generally suffer from poor bioavailability, significant adverse reactions, and inconvenient intravenous administration[7-9]. Thus, nanomedicine, which involves drugs encapsulated in materials such as liposomes, NPs, or polymer micelles, has become increasingly important[10-12]. These nanocarriers can protect the drug from degradation, modulate drug pharmacokinetics and biodistribution, and improve targeted delivery to diseased areas at the cellular and tissue levels. However, currently using NPs as drug delivery carriers still involves several critical challenges: (a) an appropriate design of the delivery model, including its structure, composition, and physicochemical properties, to achieve optimal encapsulation and drug release efficiency. (b) the currently available nanomedicines face issues such as uncontrolled "burst release" of loaded drugs after administration, variability in drug loading (i.e., the proportion of drug transporters), and low drug-to-transporter ratios (often expressed as a percentage, usually less than 5%)[13]. (c) to achieve desired biodistribution, higher therapeutic efficiency, and lower long-term toxicity *in vivo*. NPs that already use in today's clinical way have gradually realized the challenges and opportunities that lie ahead (Figure 2.1). The promising capabilities of

nanotechnology have opened up new avenues for innovative and effective approaches to tackle cancer, making it a fascinating and rapidly evolving field of study[14].

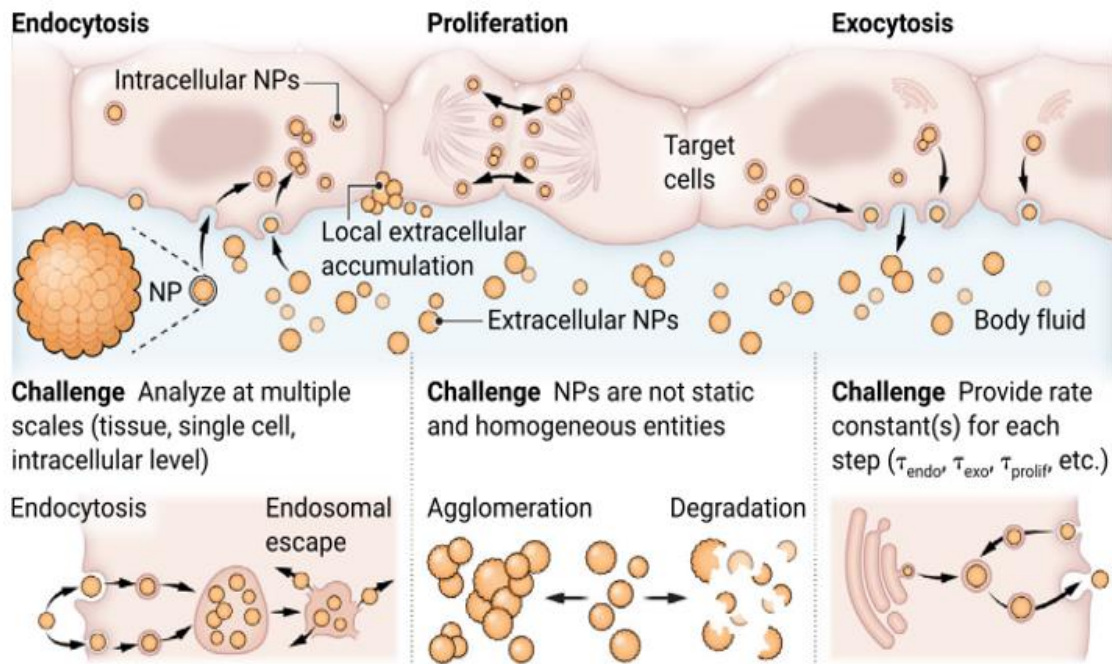


**Figure 2.1.:** The fate of nanomedicine, Cited from reference 14.

## 2.2. “EPR” Effect of Nanomedicine

The ability of nanomedicine to reach the tumor site depends on the 'high penetration and long retention effect' (EPR effect). The EPR effect was first reported by Japanese scientists Matsumura and Maeda in 1986, and later was defined by Torchilin[15-17]. According to previous studies, the vascular structure of most solid tumors is incomplete and defective, with various vascular permeability factors highly expressed internally. Consequently, solid tumors exhibit enhanced vascular permeability, providing ample nutrients

and oxygen to the tumor and promoting rapid tumor tissue growth. Exploiting this property, macromolecules larger than 40 kDa can selectively penetrate from tumor blood vessels into the tumor parenchyma, leading to their accumulation in the tumor tissues[18-20].

In addition, increased interstitial fluid pressure, tumor matrix density, fibroblasts, macrophages, and other characteristics and factors can influence the extent of the EPR effect. Recent studies have shown that the EPR effect is heterogeneous, and its strength varies depending on the type, stage, and microenvironment of the tumor, as shown in Figure 2.2.

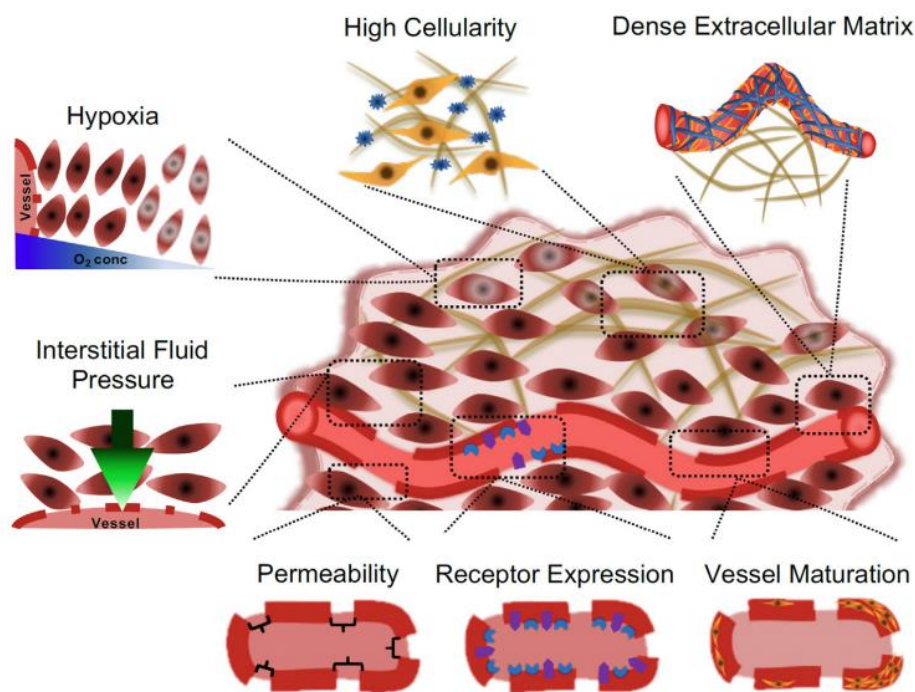


**Figure 2.2.:** Biological barriers contributing to heterogeneity in EPR-mediated tumor targeting. Cited from reference 17.



## **2.3. Classification of Nanomedicine Carriers**

Researchers have designed and developed a series of nanomedicine carriers, which can be roughly classified based on their components and preparation methods as follows:

### **2.3.1. Micellar Carriers**

Most anti-tumor drugs are poorly soluble in aqueous solution, therefore they can be encapsulated in the hydrophobic core of micelle molecules through hydrophobic interactions, hydrogen bonds, electrostatic interactions, van der Waals forces, etc[21]. In aqueous solution, amphiphilic polymers aggregate hydrophobic structures through hydrophobic-hydrophobic interactions, wrapping them together to form a hydrophobic core, while distributing hydrophilic parts outside to form a hydrophilic shell, thus obtaining micellar. When micelles interact with the biological environment, the hydrophilic shell plays a crucial role. Utilizing hydrophilic segments with anti-adsorption properties can reduce binding of serum components, maintain the integrity of micelle, thereby avoiding leakage and loss of drugs in systemic circulation. The Figure 2.3 shows a schematic of the formation of micelles from amphiphilic molecules, their loading of poorly soluble drugs, and some possible ways to further modify the micelles to improve their performance as drug carriers. There are currently some micelles used in clinical applications like PEG-PLGA micelles. Due to the size and surface properties conferred by PEG corona, PEG-PLGA amphiphilic micelles can be easily transported in the bloodstream. Currently, mixed micelles obtained from monoolein and taurocholate with Mn-mesoporphyrin has been shown as a contrast agent for T1-weighted magnetic imaging[22].

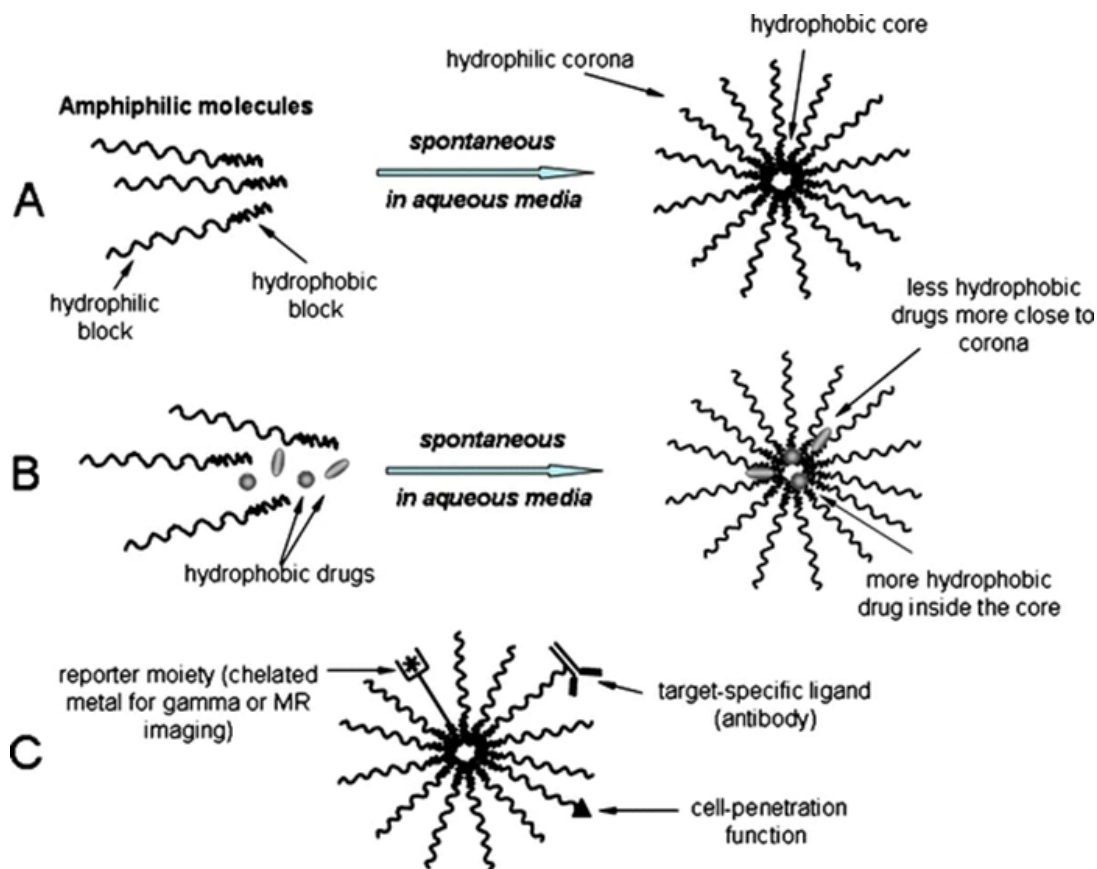


**Figure 2.3.:** (A) Spontaneous micelle formation from amphiphilic molecules in aqueous solution; (B) Micelle loading with hydrophobic drugs; (C) Multifunctional pharmaceutical micelle. Cited from reference 21.

### 2.3.2. Lipid Nanoparticles (LNPs)

Lipid nanoparticles consist of one or more bilayer membrane structures, with hydrophilic regions encapsulated between an inner core and a central bilayer. Its main components are usually natural phospholipids, thus it exhibits high biocompatibility and low toxicity, and can fully degrade within the body. Due to its structure, liposomes can encapsulate or

incorporate almost any drug molecule, regardless of its physicochemical properties or molecular size. Lipid-soluble drugs can be accommodated within the bilayer membrane of liposomes, while water-soluble drugs can be accommodated within their hydrophilic region. Moreover, synthetic liposomes and lipid nanoparticles (LNPs) are widely used in drug delivery and vaccines. Lipid nanoparticles have successfully entered the clinic for the delivery of mRNA; in particular, lipid nanoparticle mRNA vaccines are now in clinical use against coronavirus disease 2019 (COVID-19), which marks a milestone for mRNA therapeutics[23].

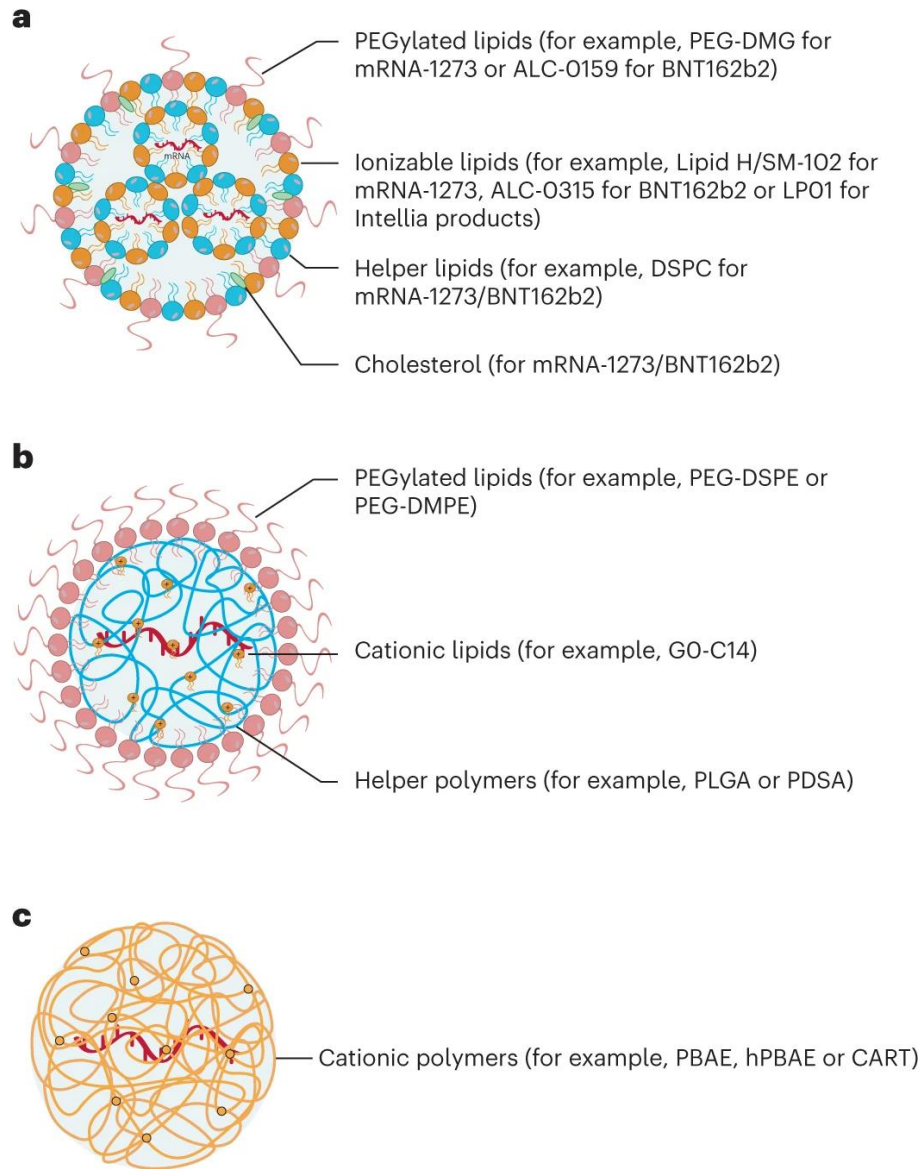


**Figure 2.4.:** mRNA delivery vehicles based on lipids nanoparticles, LNPs often consist of four basic components: a PEGylated lipid, a helper lipid, cholesterol and a cationic or ionizable lipid. Cited from reference 22.

### 2.3.3. Inorganic Material Nanocarriers

Inorganic nano-carriers are widely used in imaging studies. They are typically composed of metallic elements or other non-degradable compounds. These inorganic nanoparticles can be prepared with a variety of sizes, structures, and geometric shapes. Additionally, they possess unique properties such as magnetic, thermal, and electrical characteristics, enabling them to exhibit stimuli-responsive release, photothermal, photodynamic, magneto-thermal, and magneto-dynamic functionalities.

#### Colloidal gold nanoparticles (AuNP)

Colloidal AuNPs have been used by artists for centuries due to their physical optical properties[24]. AuNPs exhibit distinct absorption and scattering of light, resulting in colors ranging from vivid red (for spherical particles less than 100 nm) to blue-black (for larger spherical particles or nanorods). This color variation depends on factors such as particle size, shape, local refractive index, and aggregation state[25, 26]. As one of the key core materials for nanoparticles, the method of synthesizing gold nanoparticles using gold chloroaurate as a precursor is already highly developed. The most common chemical route is precipitation AuNPs in aqueous solution. Gold precursor salts are first reduced to form ions, which then act as nuclei. These nuclei continue to grow, eventually forming nanoparticles. Polte et.al presented using synchrotron radiation provides time-resolved in situ information on the formation of AuNPs[27]. The mechanism of AuNPs formation is proposed, involving distinct steps such as nucleation and subsequent monomer attachment, leading to particle growth. One successful and common method to obtain spherical AuNP is based on the reduction of tetrachloroauric acid ( $\text{HAuCl}_4$ ), known as the Turkevich citrate method[28]. The synthesis of rods shaped NPs requires a more complex two-step process, involving the use of cetyltrimethylammonium bromide (CTAB).

Considered the toxicity of CTAB, for use in any biological application, the CTAB layer must exchange with, or encapsulated by a more biocompatible coating[29]. By choosing the surfactant molecules, it is possible to adjust the surface properties. Often poly(ethylene glycol) (PEG) is used as a ligand exchange materials, after surface modification, the biocompatibility of particles will be improved, and the dispersion and stability will be increased. In our group, we utilize an amphiphilic molecule called PMA for surface modification[30-33]. This enables us to modify the surface of hydrophobic nanoparticles, achieve phase transition, and provides many prospects for the subsequent applications of nanoparticles in aqueous environments.

#### Gold nanoclusters (Au NPs(1.7 nm))

Among the different gold nanomaterials, a specific type of NPs, gold nanoclusters (Au NPs(1.7 nm)), with sizes up to hundreds of Au atoms have been extensively investigated in bio-nanotechnology applications due to their well-defined structure, high water solubility, low biological toxicity. Fluorescent Au NPs(1.7 nm) have shown high compatibility, superior photostability and exhibited near-infrared with long lifetime and large stokes shift. Researchers have found when the size of the gold core becomes comparable to the Fermi wavelength of an electron (0.5 nm), electron excitation levels would start to emerge[34, 35]. Based on those properties of Au NPs(1.7 nm), a platform which is discussed in terms of imaging, therapy, and theranostic applications can be integrated.

Molly et al. have synthesized  $\sim 2$  nm catalytic Au NPs(1.7 nm) modified with orthogonal protease substrates that are responsive to multiple enzymes. And they also demonstrated that Au NPs(1.7 nm) templated with peptide can be filtered by the kidneys and still have the high efficiency[36].

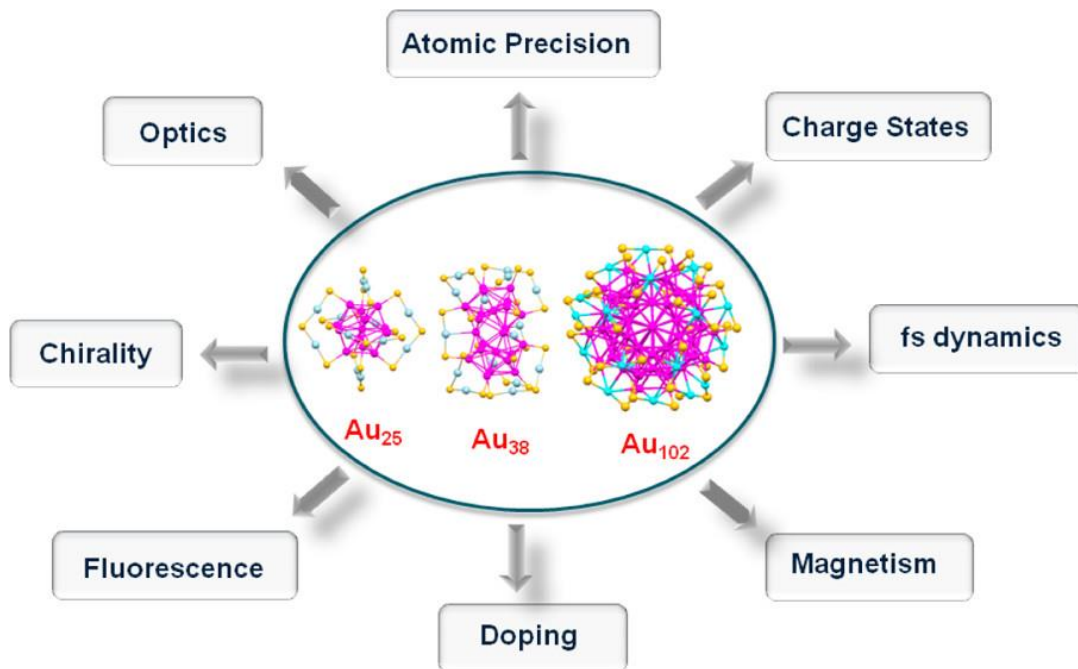


**Figure 2.5.:** The several typical sizes of gold nanoclusters and illustrate the novel properties of metal nanoclusters imparted by quantum size effects. Cited from reference 33.

### Quantum dots (QDs)

This year's Noble Prize in Chemistry has been awarded to Moungi Bawendi, Louis Brus, and Alexei Ekimov, for the discovery and synthesis of quantum dots. At a conference, Brus described a research field brimming with potential applications and he has designed a method utilizing "wet chemistry" to manufacture colloidal semiconductor particles with diameters of just a few nanometers[37]. These entities are named quantum dots (QDs), meaning their properties (such as optical absorption and emission spectra) are governed by quantum mechanical effects. The extremely small size implies an energy shift of the

topmost electron band relative to its value in bulk materials, a shift dependent on the particle size itself[38]. Through this method, the color of light emitted can be adjusted by controlling their size. Inorganic quantum dots (QDs) can be understood as zero-dimensional semiconductor nanocrystal structures that bind excitons in three-dimensional space. As the name suggests, these are inorganic materials, mainly composed of elements from groups II-VI, III-V, and IV-VII, such as cadmium selenide (CdSe), zinc sulfide (ZnS), indium arsenide (InAs), etc[39]. The term 'QDs' refers to their small size, which can be conceptualized as a point. This characteristic imparts unique properties to QDs that are lacking in macroscopic materials, including volume effect, surface effect, quantum size effect, and macroscopic quantum tunneling[40, 41]. Moreover, quantum dots, in comparison to traditional small molecule dyes, exhibit high color purity, improved fluorescence brightness and photostability[42]. They possess natural advantages such as broadband absorption, narrow-band emission, and the ability to adjust spectral properties by controlling size. Since their discovery in the early 1980s, quantum dots have been used in inorganic ion sensing, biomacromolecule sensing, cell staining and therapy, and in vitro and in vivo imaging applications due to their unique optical properties[43].



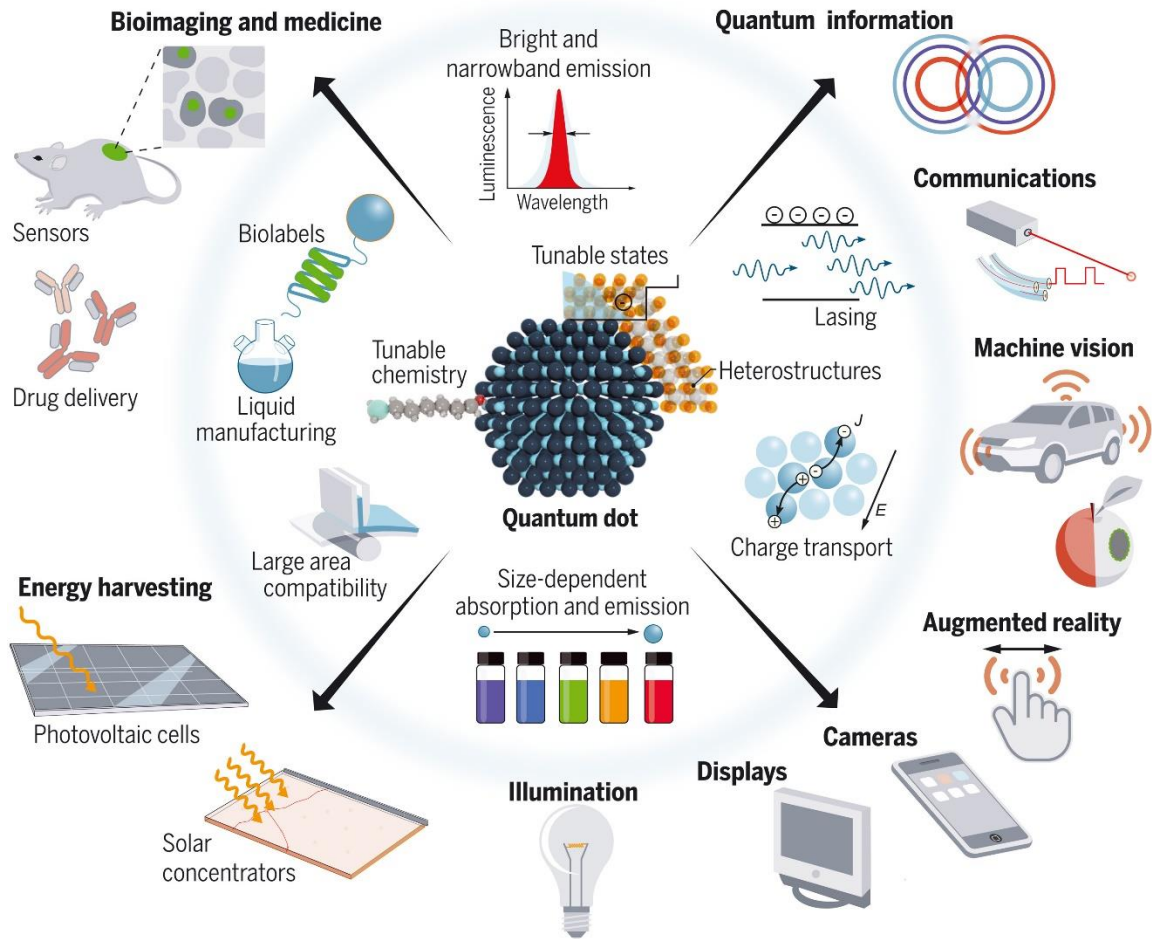


**Figure 2.6.:** The Quantum dots are semiconductor particles and electronic properties that differ from those of larger particles via quantum mechanical effects. Cited from reference 43.

## **2.4. Various properties influence the fate of nanomedicines**

### **2.4.1. Size Effects**

The size of nanomedicine is a crucial physical and chemical property that can significantly influence various biological effects when used *in vivo*, including the half-life of blood circulation, vascular extravasation, and macrophage uptake (Figure 2.7). For instance, NPs smaller than 6 nm are rapidly eliminated by the kidneys following intravenous injection, while 200 nm NPs are mainly retained in spleen. Kataoka et al. have demonstrated that polymeric micelles smaller than 100 nm can penetrate hyperpermeable tumor tissues[44]. Some reports have confirmed that nanoparticles with a size of approximately 100 nm are most likely to enter cells through endocytosis, primarily due to their large volume-to-surface area ratio[45-47]. The tunable surface area-to-volume ratio of nanoparticles, which allows for effective functionalization, such as attaching targeting molecules, drugs, or imaging agents. This balance in size and surface area facilitates efficient interactions with cell membranes.

### **2.4.2. Morphology Effects**

Nanoparticles can exhibit various shapes, including spherical, rod-shaped, star-shaped, and others. The morphology of nanoparticles also influences their performance in physiological environments. Mitragotri et al. demonstrated that geometric parameters of nanomedicines, such as curvature and aspect ratio, can directly affect the ability of nanoparticles to be taken up and internalized by macrophages[48]. Discher et al. demonstrated that filamentous polymer micelles have a circulation time of up to one week, whereas spherical polymer micelles only exhibit a circulation time of 2-3 days. This difference is primarily attributed to the alignment of filamentous micelles with the direction of blood flow[49]. Fan et al. found that nanospikes on nanoparticles regulate

the recruitment of myosin IIA to the cell membrane during cellular uptake, thereby increasing the efficiency of cellular uptake, as revealed by bimodality (plasma and fluorescence) imaging[50].

### **2.4.3. Surface Potential Effects**

The surface charge of NPs is another crucial physical characteristic, by optimizing the surface charge can extend their circulation time and selectively enhance the accumulation at specific sites. In complex biological environments, proteins interact with and adhere to the surface of NPs, forming a protein crown structure on their surface, often referred to as a 'protein corona'[51-53]. Kataoka et al. demonstrated the advantage of prolonged circulation for neutral and anionic polymer micelles, revealing that negatively charged particles exhibit reduced accumulation in the liver and spleen. Conversely, positively charged nanoparticles tend to have a higher rate of nonspecific uptake in most cells. Studies have found that positively charged particles can also enter endosomes for drug release through mechanisms like the proton sponge effect, thus reducing drug degradation by the endosome[54, 55].

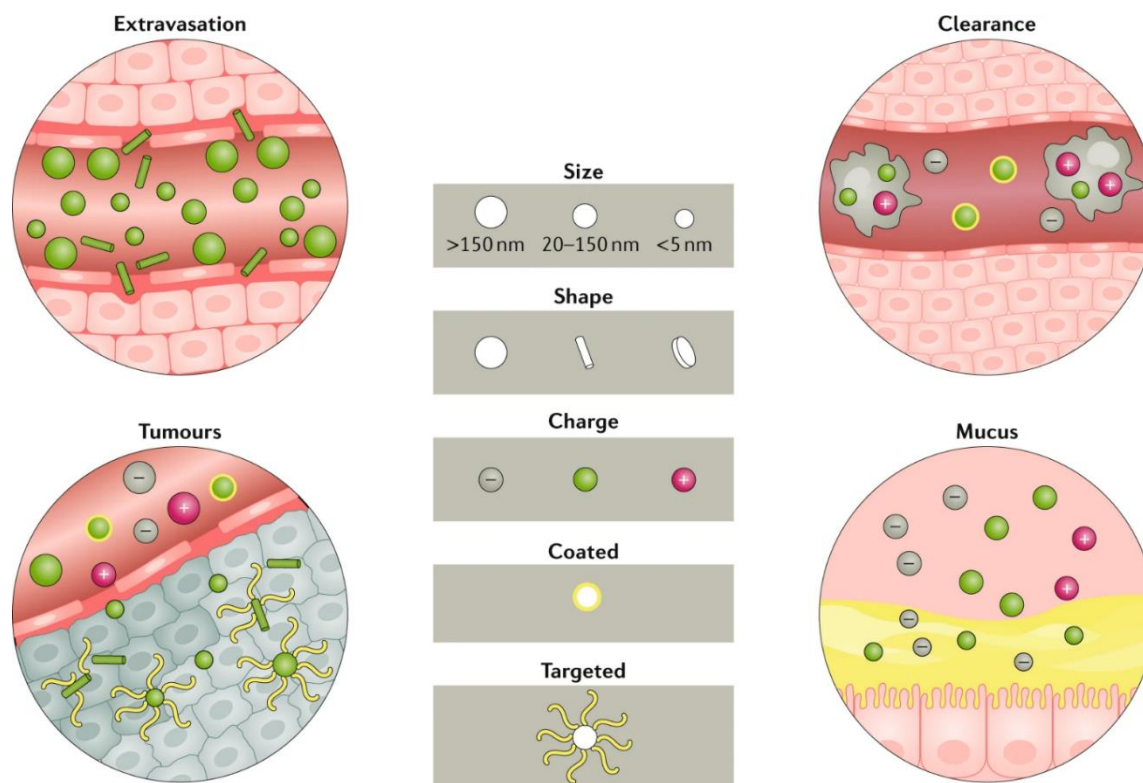


**Figure 2.7.:** Factors such as size, shape, charge and surface coating determine what happens to nanoparticles in the circulation, including clearance, and how the NPs interact with local barrier such as the tumor microenvironment or mucus layers. Cited from reference 53.

### **3. Motivation**

Cancer stands as one of the malignant diseases that significantly threaten human life and health in modern society, thus there is an urgent demand for the development of safe and efficient treatment methods to confront this formidable challenge. Many drugs need to reach specific cells or organelles within the body to exert their therapeutic effects effectively[56, 57]. Besides, without efficient cell uptake, drugs may remain in the extracellular space, where they might not be able to reach their intended targets or may be cleared from the body before exerting their effects[58, 59]. To address the above issues, some studies are dedicated to designing hybrid nanoparticles for the diagnosis and treatment of tumors. Nanoparticle size is a key factor influencing their ability to penetrate and remain in tissues. While small nanoparticles can penetrate deep into tumor tissue, they are often not retained well, whereas larger nanoparticles tend to accumulate around tumor blood vessels. Therefore, assembling smaller nanoparticles into larger structures is advantageous for extending blood circulation time and increasing accumulation in tumors compared to individual smaller nanoparticles. After administration, the first step involves the internalization and degradation of nano-hybrids within cells, which is a prerequisite for monitoring it in vivo biological behavior. In other words, gaining knowledge about cellular degradation is advantageous for scientists in designing more functional biological nanomaterials. Unfortunately, until now, there has been little research quantitatively compare the efficiency of different nanodelivery models. Targets for potential cancer treatments typically reside within tumor cells, emphasizing the pivotal role of endocytosis efficiency in determining therapeutic outcomes. Efficient endocytosis in tumor cells can lead to excellent therapeutic effects even at low doses, while minimizing damage to normal tissues. Based on these considerations, it is crucial to develop a drug delivery system with high efficiency in cellular uptake and also study them in quantitative way, it will offer valuable insights into the design of future nanodelivery system.



## **4. The Main Research Content**

Post intravenous injection, nanomedicines undergo a sequence of intricate extracellular processes before reaching tumor cells, encompassing circulation in the bloodstream and penetration from outside blood vessels deep into the tumor tissue. On one hand, nanomedicines can remain stable in the bloodstream circulation. On the other hand, upon reaching tumor tissues, the tumor's unique microenvironment can induce changes in the nanoparticles, enhancing cellular uptake or facilitating rapid drug release. In this context, degradable polymers emerge as indispensable contributors to drug delivery systems, enhancing drug solubility, increasing utilization, and sustaining high biocompatibility.

The comprehensive research is structured into two main segments:

### **4.1. Innovative Strategy of Highly Permeable and Highly Deliverable Nanomedicine Based on Gold Nanoparticles**

The delivery efficiency of nanomedicines constitutes a pivotal factor influencing their therapeutic efficacy. The size and various characteristics of nanoparticles play a crucial role in determining their tissue penetration and retention. While small nanoparticles possess the capability to penetrate deeper into the tumor parenchyma, their retention is less effective[60]. Conversely, larger nanoparticles tend to distribute around tumor blood vessels. Consequently, the assembly of such nanoparticles proves beneficial for prolonged blood circulation and enhanced tumor accumulation, owing to their larger size compared to individual smaller nanoparticles[61, 62].

In this study, we quantitatively compare the cellular endocytosis efficiency of small nanoparticles aggregated in a polymer matrix to form larger particles, with that of conventional small nanoparticles. Additionally, we investigate their fate after entering the cell and assess cellular exclusion efficiency.

#### **4.2. Quantum Dots and FITC Labelled Nanocomposite as a Platform for Biodegradation Studies**

In order to further understand the mechanism of action of nanoparticles in cells, we need to track the movement trajectory and degradation release of nanoparticles in cells. mPEG-PLGA is a commonly employed polymer blend for crafting polymer nanoparticles. The combination of PEG's hydrophilicity and PLGA's biocompatibility renders it an ideal carrier for drug delivery. In this study, we co-encapsulate both quantum dots and fluorescent molecules within polymer vesicles to create a nanocomposite.

The focus of our investigation lies in elucidating the degradation process of polymersomes at the cellular level. Specifically, we study the degradation process by examining the phenomenon in which fluorophores and quantum dots cease to colocalize after endocytosis.



## **5. Quantification of improved delivery and clearance of nanoparticles due to endosomal/lysosomal degradation**

### **5.1. Introduction**

Over the past few decades, a diverse array of nanoparticles has been developed and extensively applied in the field of biomedical research, encompassing areas such as biological imaging[63-65], biosensing[26, 66, 67], drug delivery[45, 68, 69], and therapy[70-72]. With deep research into the mechanism of action of nanoparticles in cells, precise quantification of intracellular NPs has become particularly crucial. This is not only an indicator of assessing the efficiency of NPs in executing their intended functions but also a critical aspect in evaluating their biological safety[73-75]. Meanwhile, control over factors such as NPs delivery efficiency and degradation rate are paramount for their medical applications within the human body. It is well-known that small-sized NPs exhibit deeper penetration in tumor tissues but are accompanied by a short-lived circulation time in the bloodstream. Conversely, larger-sized NPs demonstrate more efficient circulation in the bloodstream. Therefore, a recent emerging strategy involves designing NPs with small particles as components inside larger, degradable nanostructures. These structures disassemble into multiple small nanoparticles under the influence of the tumor microenvironment or external stimuli, encompassing inorganic, organic, and hybrid NPs. Based on their structures, these nano-complexes can be broadly classified into three categories: a). Aggregation of small NPs, where small particles directly aggregate to form larger ones with surface chemistry essentially identical to the small ones[76-79]. b). Decoration of small NPs on a bigger core, achieved through physical adsorption and chemical bonding of small-sized NPs onto organic or inorganic NPs[80]. c). Small NPs coated with a sheddable shell, typically constructed from PEGylated liposomes, polymersomes, or other negatively charged polymers[81-83]. Regard the delivery

efficiency of NPs, i.e., the quantification of NPs within cells, various proven techniques exist[83, 84]. In this study, we employed inductively coupled plasma mass spectrometry (ICP-MS) for quantitative comparison, renowned for its high sensitivity in detecting substances containing metals or metal oxides.

In this research, we designed two systems to quantify and compare their intracellular uptake and extracellular efflux in HeLa cells. In the first system, we utilized polyelectrolyte capsule as a core, loaded with 50 nm gold NPs to form nanoassemblies. Preliminary results indicate that, at the same exposure concentration, nanoassemblies exhibit favorable efficiency in cellular internalization. Subsequently, three types of NPs with identical hydrated sizes were prepared, and their intracellular uptake and extracellular exocytosis in HeLa cells were quantitatively compared over the same duration. Through the electrostatic force between the amino groups of poly-L-arginin and the carboxyl groups of gold nanoclusters, multiple gold nanoclusters were aggregated to form nanoassemblies with diameter of approximately 100 nm. In the intracellular uptake experiments, we simultaneously quantitatively analyzed the uptake efficiency of the three types of NPs (plain gold nanoclusters, colloidal gold NPs, gold nanoclusters formed nanoassemblies) types in HeLa cells.

## 5.2. Major Reagents

Name	CAS	Company	Function
Poly-L-arginin hydrochlorid	#26982-20-7	Sigma Aldrich	For NPs synthesis
Sodium carbonate	#497-19-8	Sigma Aldrich	For Capsule synthesis

Calcium chloride anhydrous	#10043-52-4	Sigma Aldrich	For Capsule synthesis
Poly(sodium4-styrenesulfonate)	#25704-18-1	Sigma Aldrich	For Capsule synthesis
Poly(allylamine hydrochloride)	#71550-12-4	Sigma Aldrich	For Capsule synthesis
Ethylenediaminetetraacetic acid disodium salt dihydrate	#6381-92-6	Sigma Aldrich	For Capsule synthesis
Gold (III) chloride trihydrate	#16961-25-4	Sigma Aldrich	For Gold NPs synthesis
Trisodium citrate	#6132-04-3	Sigma Aldrich	For Gold NPs synthesis
Poly(isobutylene-altmaleic anhydride)	#26426-80-2	Sigma Aldrich	For PMA synthesis
Dodecylamine (DDA)	#124-22-1	Sigma Aldrich	For PMA synthesis
1- dodecanethiol (DDT)	#112-55-0	Sigma Aldrich	For PMA synthesis
L-glutathione	#70-18-8	Sigma Aldrich	For GoldNanocluster synthesis
Chloroform	#67-66-3	Roth	For PMA coating
PEG2000		Rapp Polymere	For Gold NPs synthesis
Trypsin-EDTA 0.05%		ThermoFisher	For cell culture

Fetal bovine serum		Biochrom	For cell culture
Dulbecco's Modified Eagles Medium (DMEM)		ThermoFisher	For cell culture
phosphate-buffered saline		Invitrogen	For cell culture
Resazurin		Sigma-Aldrich	For cytotoxicity

### 5.3 Key Instruments

Name	Model	Company	Function
Dynamic light scattering (DLS)	NANO ZS	Malvern	NPs characterization
UV-vis absorption spectrophotometer	Agilent 8453	Agilent	NPs characterization
Fluorescence Spectrometer	Cary Eclipse	Agilent	NPs characterization
Rotary evaporator	Helzbad Hel-VAP	Heidolph	For NPs synthesis
Laser Scanning Microscope	LSM 980 mit Airyscan 2	ZEISS	For biodegradation studies
Marcoplate reader	FLUOstar Omega	BMG LABTECH	For cellular cytotoxicity studies
Inductively coupled plasma mass spectrometry (ICP-MS)	7700 Series	Agilent	NPs characterization
Transmission electron microscopy (TEM)	JEM-1400PLUS	JEOL	For NPs morphology visualization

Scanning electron microscopy (SEM)	SIGMA	ZEISS	For NPs morphology visualization
------------------------------------	-------	-------	----------------------------------

## 5.4. Experiments and Methods

### 5.4.1. Synthesis of 100 nm PMA-coated Au Nanoparticles (Au NPs (100 nm))

Au NPs with citric ligand were synthesized according to previously published protocols[26]. A solution of sodium citrate (2.2 mM) in 150 mL of Milli-Q water was heated for 15 minutes in a 250 mL three-necked round-bottom flask using a heating jacket under vigorous stirring. A condenser was used to prevent evaporation of the solvent. After boiling the mixture, 1 mL of Gold (III) chloride trihydrate ( $\text{HAuCl}_4$  (25 mM)) is injected. The color of the solution changes from yellow to gray-blue and then to soft-pink within 10 minutes. The obtained NPs ( $\sim 10$  nm,  $\sim 3 \times 10^{12}$  NPs/mL) are coated by negatively charged citric acid ions and are therefore well suspended in Milli-Q water. Immediately after the synthesis of the Au seeds and in the same vessel, the reaction was cooled until the temperature of the solution reached 90 °C. Then, 1 mL of sodium citrate (60 mM) and 1 mL of  $\text{HAuCl}_4$  solution (25 mM) were sequentially injected for 30 minutes. Repeat this process twice as generation 0 (g0). After that, the mixture was diluted by extracting 55 mL of sample and adding 53 mL of Milli-Q water and 2 mL sodium citrate (60 mM) with stirring for 15 minutes. This solution was then used as a seed solution, and the process was repeated several times until the Ultraviolet-visible spectroscopy (UV-vis) to determine the NPs size. Au NPs are hydrophilic, modified using Polyethylene glycol 2000 (PEG<sub>2000</sub>) with sulfhydryl groups and added into the above solution in specific ratio overnight. Using 6000 rpm centrifuge to removed excess PEG<sub>2000</sub>, and then the 1 mL

dodecyl amine (DDA) was dissolved in 50 mL chloroform and added into Au-PEG NPs in the ratio (cDDA/cNP) of  $20 \times 10^6$  for 6 hours[85]. The organic phase was then collected through a separatory funnel. To remove free DDA, centrifuge the organic phase and collect the precipitate. The precipitate is washed 2 more times and dispersed in 20 mL of chloroform. Phase transfer of Au-DDA NPs from chloroform to Milli-Q water using poly(isobutylene-alt-maleic anhydride) (PMA) polymer (Scheme 5.1) were synthesized according to previously published protocols[33].

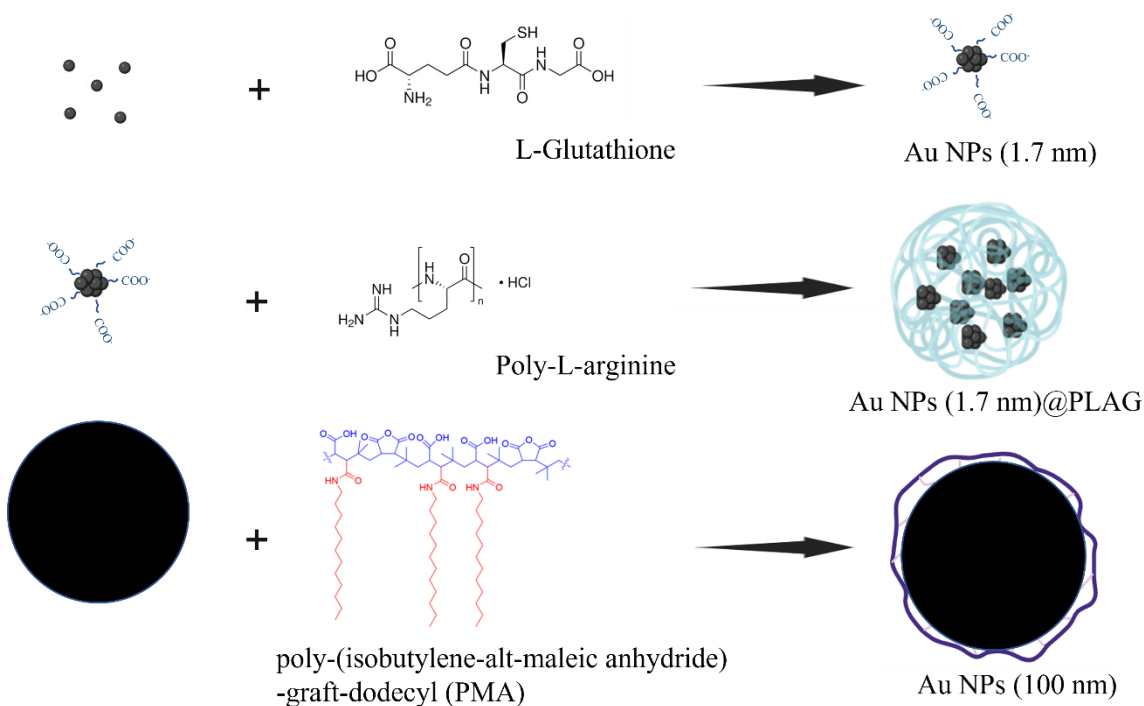
#### **5.4.2. Synthesis of Gold Nanoclusters**

Gold clusters were synthesized by the previously reported method[86]. Briefly, 300 mL of aqueous solution of  $\text{HAuCl}_4$  (2.2 mM) and L-glutathione (GSH) (3 mM) was stirred at  $70^\circ\text{C}$  for 24 hours (Scheme 5.1). When GSH was first mixed with chloroauric acid, the solution changed from clear to brown and after 10 seconds became colorless and clear again. As the stirring time increased, the solution slowly changed from clear to yellow. Finally, the Au NPs(1.7 nm) were passed through ultrafiltration centrifuge tubes (3 kDa) to remove excess GSH and stored at  $4^\circ\text{C}$ .

#### **5.4.3. Synthesis of Hybrid Structure with Gold Nanoclusters**

We designed simple experiments in which gold nanocluster nanocomplexes were prepared by adding poly-L-arginine dropwise to aqueous solutions of gold nanoclusters diluted at different concentrations and stirred for 90 minutes (Scheme 5.1). In a typical experiment, 500  $\mu\text{L}$  of poly-L-arginine (approximately 119  $\mu\text{M}$ ) was added to 20 mL of Au NPs(1.7 nm) (50  $\mu\text{g Au/mL}$ ). We referred to this nanoassembly as Au NPs(1.7 nm)@PLAG. The solution was then dialyzed with a cut-off value of 15 kDa for 48 hours to remove free

Au NPs(1.7 nm) before use, and refrigerated. Samples were also concentrated using a centrifugation solution with a cut-off of 100 kDa.



**Scheme 5.1.:** Synthetic routes of three nanoparticles (Au NPs(1.7 nm), Au NPs(1.7 nm)@PLAG and Au NPs(100 nm))

#### 5.4.4. Synthesis of Polyelectrolyte Capsule-AuNP(Au NPs (50 nm)@PSS/PAH)

Polyelectrolyte capsules prepared by layer-by-layer (LbL) assembly of oppositely charged  $\text{CaCO}_3$  cores and depositing alternating layers of negatively charged poly (sodium 4-

styrenesulfonate) (PSS, Mw = 70 kDa, 10 mg/mL in 0.05 M NaCl, pH 6.5,) and positively charged poly (allylamine hydrochloride) (PAH, Mw = 56 kDa, 10 mg/mL in 0.05 M NaCl, pH 6.5)[87]. First, the synthesis procedure is as follows: 0.615 mL of 0.33 M sodium carbonate ( $\text{Na}_2\text{CO}_3$ ) aqueous solution is added to 0.615 mL of 0.33 M calcium chloride and stirred (1000 rpm) for 30 seconds at room temperature. Then, let the solution sit for 2 minutes. The  $\text{CaCO}_3$  core is first re-suspended in 1 mL of PSS solution, sonicated for 3 minutes, then oscillated for 30 minutes, and finally the solution is centrifuged at 2500 rpm for 1 minute to remove the supernatant. Then 2 mL of Milli-Q water is added for triple washings. This procedure is also applicable for the PAH shell layer.

After assembly of two bilayers, i.e.  $\text{CaCO}_3/(\text{PSS}/\text{PAH})_2$ , 1.5 mL of negatively charged Au-PEG NPs (0.37 mg) were added. The mixture was sonicated for 3 minutes, shaken for 10 minutes, and washed 3 times with Milli-Q water. Finally, the capsules made of  $\text{CaCO}_3/(\text{PSS}/\text{PAH})_2/\text{Au}$  NPs/PAH/PSS were formed. To remove the  $\text{CaCO}_3$  core, the capsules were dissolved in 1.2 mL of 0.2 M ethylenediaminetetraacetic acid aqueous solution (pH 6.5, EDTA disodium salt) solution overnight.

#### 5.4.5. Quantum Yield Measurements

To determine the quantum yields (QY)  $\Phi$  of Au NPs(1.7 nm) and Au NPs(1.7 nm)@PLAG with Rhodamine B, UV-vis absorption spectra were collected and the absorbance values at  $\lambda = 400$  nm for different concentrations of samples were recorded[88]. The emission spectra of Au NPs(1.7 nm) and Au NPs(1.7 nm)@PLAG were recorded with excitation at  $\lambda_{\text{Ex}} = 400$  nm and intensities were integrated from 600 - 620 nm and resultant integrated intensity was plotted with respect to the absorbance values. The gradient  $\text{dI}/\text{A}_{400}$  of each plot has been used in the following equation (eq 5.4.1) to get the QY values.



$$\Phi_X = \Phi_{St} \left( \frac{(\Delta I / \Delta A_{400})_X}{(\Delta I / \Delta A_{400})_{St}} \right) \left( \frac{\eta_X}{\eta_{St}} \right)^2 \quad \text{eq 5.4.1}$$

Where  $\Phi_X$  is the fluorescence quantum yield of the test samples,  $\Phi_{St}$  is the fluorescence quantum yield of the standard Rhodamine B;  $(\Delta I / \Delta A_{400})_X$  and  $(\Delta I / \Delta A_{400})_{St}$  are the gradients from the plot of integrated fluorescence intensity vs absorbance of the test samples and the standard at the same excitation wavelength of 400 nm;  $\eta_X$  and  $\eta_{St}$  are the refractive indices of the solvents of the test samples ( $\eta_{\text{water}} = 1.33$ ) and the solvent of the standard ( $\eta_{\text{ethanol}} = 1.3614$ ), respectively.

#### 5.4.6. Dynamic Contact Angle Measurement

To measure the contact angle (CA) of water, we need to prepare a clean glass slide and secure it on the working platform[89]. Using a syringe, we dispense 50  $\mu\text{L}$  of the nanoparticle solution (through a stainless-steel needle with a diameter of 1.85 millimeters(mm)) onto the glass slide. The shape of the droplet is then recorded using a high-speed camera and analyzed using a Drop Shape Analysis instrument (DSA30, Krüss, Germany) to dynamically measure the contact angle between the droplet and the glass surface (Figure 5.1). The relationship of a CA to the balance between liquid-liquid attraction and liquid-solid attraction is completely quantitative and is expressed by a simple equation. The CA is calculated based on Young's equation (eq 5.4.2), as shown below:

$$\cos(\theta) = (\gamma_{SG} - \gamma_{SL}) / \gamma_{LG} \quad \text{eq 5.4.2}$$

where  $\gamma_{SG}$  is the solid-gas surface tension,  $\gamma_{SL}$  is the solid-liquid surface tension, and  $\gamma_{LG}$  is the liquid-gas surface tension.

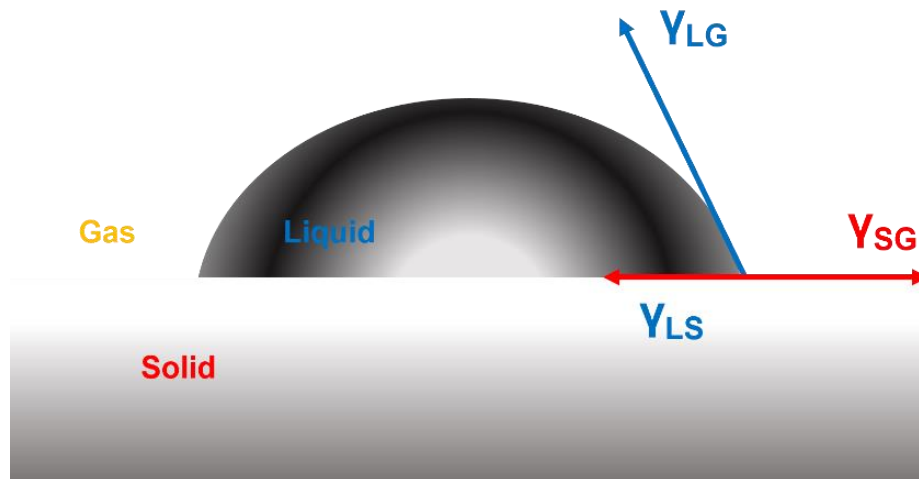


**Figure 5.1.:** Liquid droplet (seed drop) and contact angle on solid surface.

#### 5.4.7. Thermogravimetric Analysis

Thermogravimetric Analysis (TGA) is a simple analytical method that typically does not require special sample preparation techniques. Previous research has shown that TGA can reliably use to characterize nanoparticles[90-92]. In TGA, the sample is heated to high temperatures while continuously measures mass is changed over time. We performed TGA measurements over the temperature range of 100 - 700 °C under a nitrogen atmosphere at a heating rate of 10 °C/min. In an independent experiment, the dried

powered sample was placed in an alumina pan, and another empty pan was as blank. As the test proceeds, both the sample pan and the blank pan are heated or cooled simultaneously, which can provide monitor changes in the sample's mass.

#### **5.4.8. Cell Viability of Nanoparticles**

In vitro viability of the cell exposure to NPs was applied with the resazurin assay[30, 93, 94]. Briefly, Hela cells were seeded in 96 - well plates (Sarstedt, Germany) with a growth area 0.32 cm<sup>2</sup> at a density of 7,500 cells in 100 µL medium per well overnight. The NPs were diluted at different concentrations in DMEM medium. After expose different concentration of NPs for 24 hours. The cells were washed with PBS for three times, and then add 100 µL fresh medium mixed with the resazurin salt solution (10:1) at a concentration of 0.25 mg/mL solution, and the 96 - well plates were incubated at 37 °C for 4 hours. To detect the metabolic activity of cells, the blue resazurin is converted to red fluorescent due to the reduced cellular microenvironment. The emission fluorescence spectra were monitored from 572 nm to 650 nm by Microplate reader Instrument (BMG – FLUOstar Omega) with excitation at 560 nm. The viability V by calculating the fluorescence intensity recorded for each well of cells incubated with NPs. This value was normalized to the fluorescence intensity of well which had not been exposed to NPs[95].

$$V = 100 * OD (\text{control cells}) / OD (\text{test condition}) \quad \text{eq 5.4.3}$$

### **5.5. Results and Discussions**

### 5.5.1. Physicochemical Characterizations of NPs

In our drug delivery research, we strategically employed nanoparticles (NPs) with a size of approximately 100 nm as carriers for delivering cargo. This decision was guided by the remarkable high specific surface area (SSA) demonstrated by these nanoparticles[96]. Initially, gold nanoparticles (Au NPs) were synthesized using the seed growth method. Following each generation, we recorded the UV-vis and DLS spectra of the colloidal Au NPs. Due to Surface Plasmon Resonance (SPR), the absorbance of Au NPs varies depending on their size. SPR is a collective oscillation of free electrons on the metal surface in response to incident light. In the case of Au NPs, changes in size affect the electronic structure and the density of free electrons[89]. The smaller Au NPs tend to exhibit a blue shift, while larger Au NPs show a red shift in their absorption spectra. The UV-vis peak demonstrates a red-shift trend, as depicted in Figure 5.2 We also recorded the dynamic light scattering (DLS) data for each generation of Au NPs. The results indicate a progressive increase in the size of NPs compared to the previous generation. Notably, after generation 9, the size change accelerates even more rapidly (Figure 5.3). Hydrodynamic diameters ( $d_h$ ) and zeta-potentials  $N(\zeta)$  of Au NPs (100 nm), Au NPs (1.7 nm), and Au NPs(1.7 nm)@PLAG were assessed using a Zetasizer Nano (Malvern Instrument Ltd.) employing laser Doppler anemometry (LDA) at 25°C. For this analysis, 500  $\mu$ L of NP samples were utilized for hydrodynamic diameters, while 800  $\mu$ L of samples were diluted with 200  $\mu$ L of  $\text{Na}_2\text{HPO}_4$ - $\text{NaH}_2\text{PO}_4$  buffer solution (200 mM, pH 7.4) for zeta-potential measurements. We surface-modified AuNPs, initially obtained through the seed growth method with a particle size of 100 nm, by coating their surfaces with a layer of PMA polymer. Simultaneously, we synthesized nanocomposites using gold nanoclusters and poly-L-arginine, featuring hydrated particle size comparable to Au NPs(100 nm). The diagram illustrating the measured hydrated particle size and the corresponding zeta potential data is showed in the Figure 5.4.

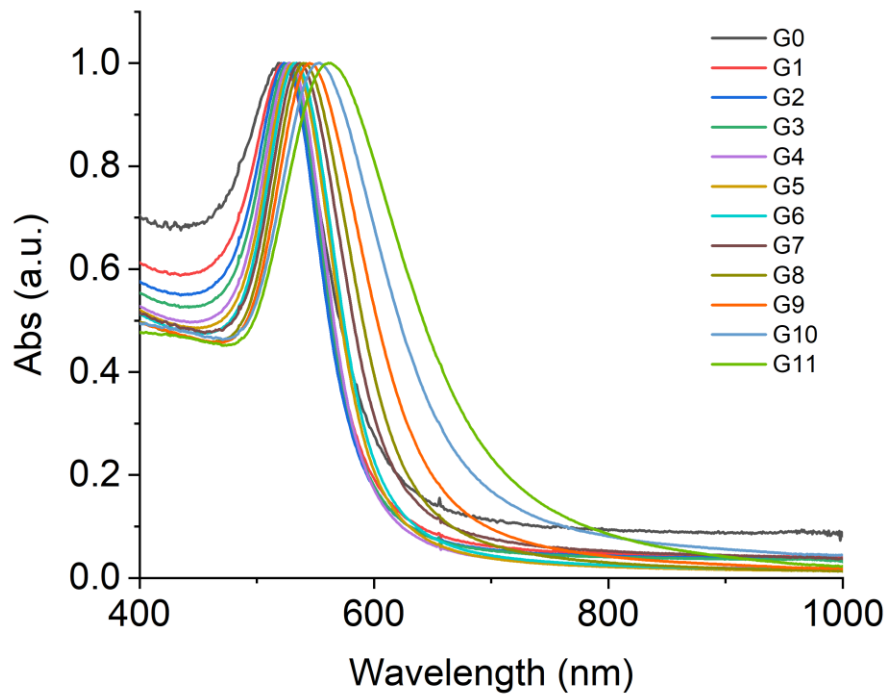


**Figure 5.2.:** The absorbance of gold nanoparticles across each generation.

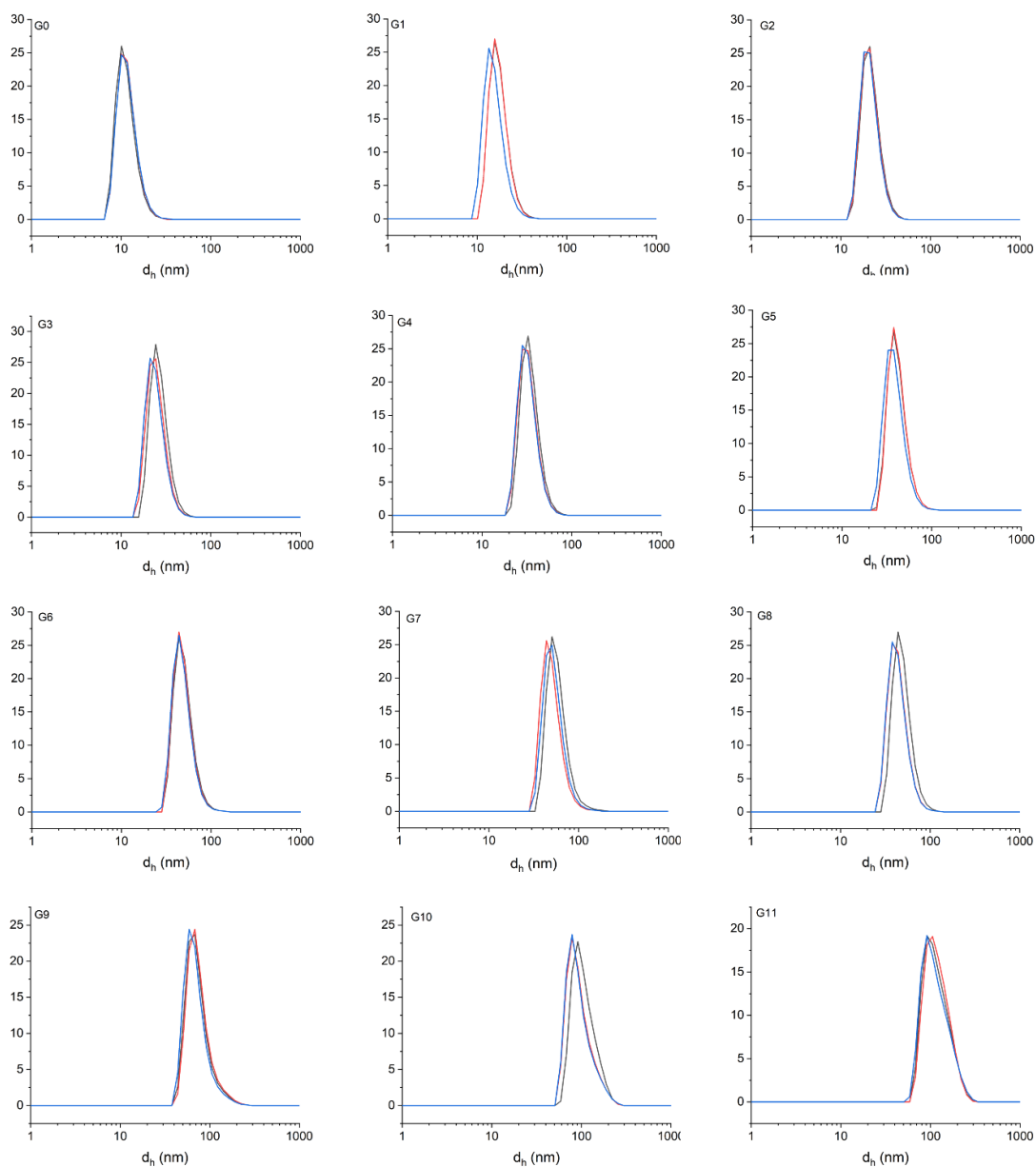


**Figure 5.3.:** The hydrodynamic diameter ( $d_h$ ) of each generation of gold NPs was determined using Dynamic Light Scattering (DLS) in Milli-Q water. Results are shown for  $n = 3$  measurements.

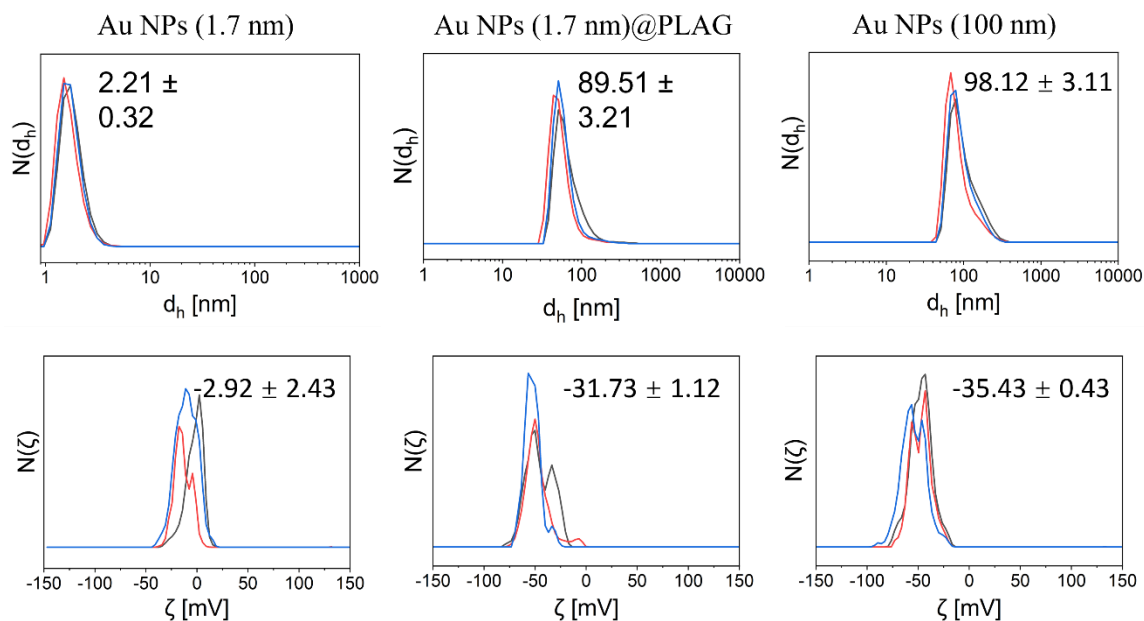


**Figure 5.4.:** The hydrodynamic diameter  $d_h$  of (a) Au NPs(1.7 nm), (b) Au NPs(1.7 nm)@PLAG and (c) Au NPs(100 nm) as determined with DLS in Milli-Q water. Zeta-potential  $N(\zeta)$  distribution of the NPs as measured in Milli-Q water by LDA. Results are shown for  $n = 3$  measurements.

The average size distribution of the diameter ( $d$ ) of nanoparticles (NPs) was determined through the analysis of approximately 100 nm from transmission electron microscopy (TEM). The TEM images were acquired using a JEM-1011 TEM instrument (JEOL, Germany). The corresponding histograms were generated using the open-source software Image J. It is noteworthy that the size of Au NPs(1.7 nm)@PLAG observed in TEM appears smaller than that in DLS. This discrepancy is attributed to the fact that DLS provides the hydrodynamic size, considering the polymer ligands, while TEM captures the core size. Illustrative TEM images of Au NPs(1.7 nm), Au NPs(1.7 nm)@PLAG, and Au NPs(100 nm), along with their respective size distributions, are presented in Figure 5.5.

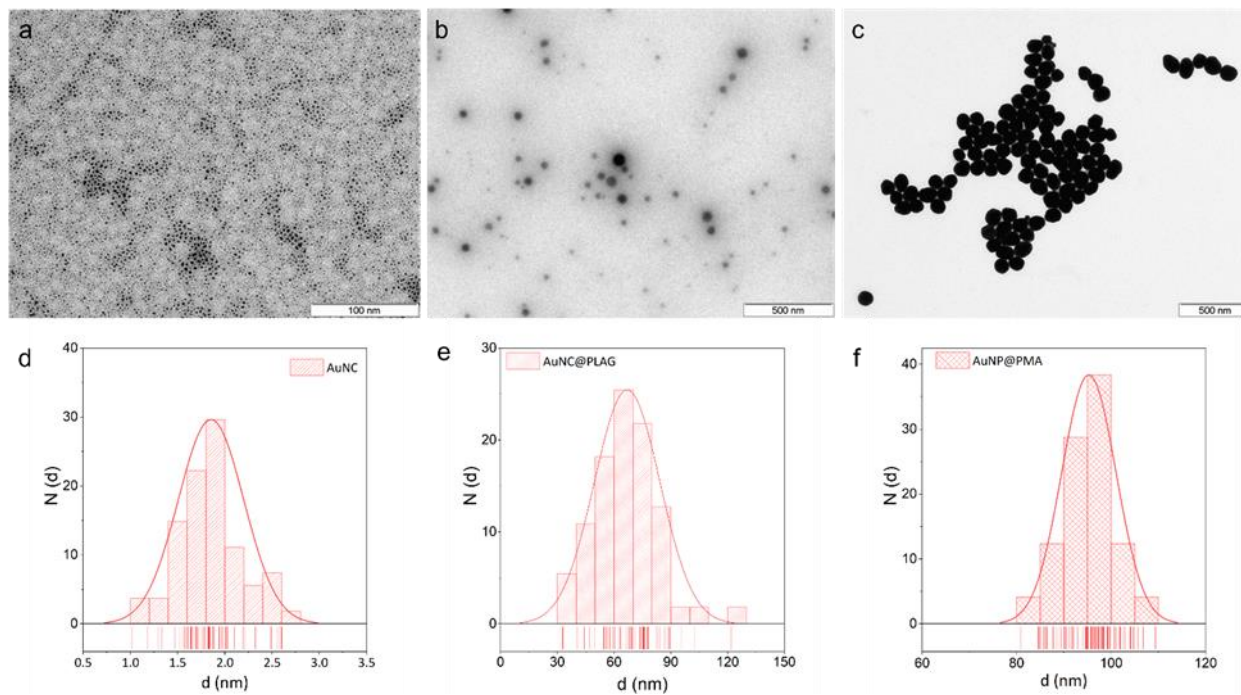


**Figure 5.5.:** Representative TEM image of (a) Au NPs(1.7 nm), (b) Au NPs(1.7 nm)@PLAG and (c) Au NPs(100 nm). The correspond size distribution of NPs.

The optical characterization of Au NPs(1.7 nm) and Au NPs(1.7 nm)@PLAG was conducted using UV-vis and PL spectroscopy. From the absorption spectra (Figure 5.6), it is evident that when free Au NPs(1.7 nm) form nanoassemblies, the intensity of the emission peak at 620 nm strengthens. This enhancement might be attributed to the reduced distance between gold nanoclusters, intensifying the Förster resonance energy transfer (FRET) effect or the AIE effect. Additionally, the emission maximum experiences a slight red-shift (the shift consistently increases from 609 nm for free Au NPs(1.7 nm) to 616 nm for Au NPs(1.7 nm)@PLAG).



Quantum yield calculations were performed based on equation 5.4.1, incorporating the quantum yield of Rhodamine B. This analysis considered the absorption and fluorescence spectra of the test samples (Au NPs(1.7 nm) and Au NPs(1.7 nm)@PLAG), which vary with concentration (Figure 5.6 a, b, d, e). The integrals represent the areas under the respective curves, providing a measure of the efficiency in converting absorbed photons into emitted photons.

To further analyze the system, Origin was employed to determine the slope of the integrated fluorescence area concerning variations in UV absorption intensity, as illustrated in Figure 5.6 c and f.

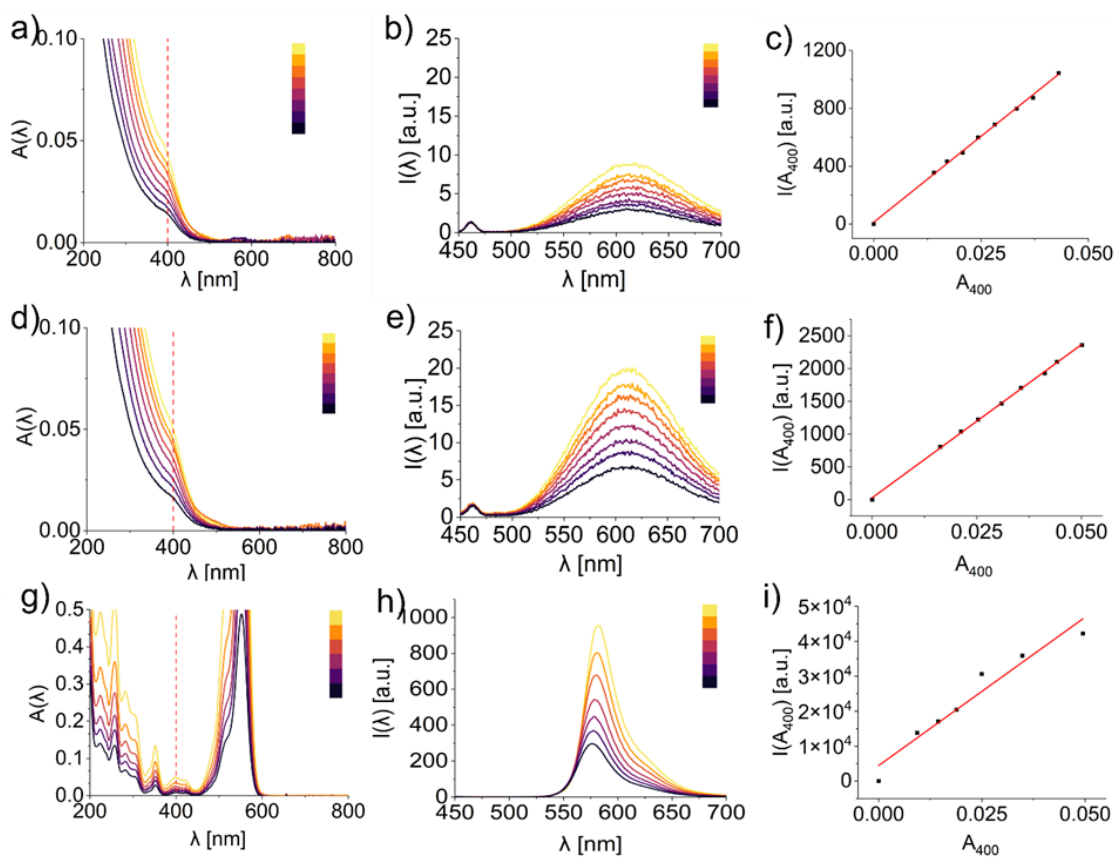


**Figure 5.6.:** (a) UV-vis absorption, (b) PL spectra of different concentrations of Au NPs(1.7 nm). The excitation wavelength is the same as the one at which the absorbance was recorded for the gradient determination (400 nm). (c) Linear plot of integrated PL intensity (taken in the entire wavelength range as shown in the corresponding plot) vs. absorbance at 400 nm with different concentrations of Au NPs(1.7 nm). (d) UV-vis absorption, (e) PL spectra of different concentrations of Au NPs(1.7 nm)@PLAG at 400 nm excitation wavelength. (f) Linear plot of integrated PL intensity vs. absorbance at 400 nm with different concentration of Au NPs(1.7 nm)@PLAG. (g) UV-vis absorption, (h) PL spectra of different concentrations of Rhodamine B. The excitation wavelength is the same as the one at which the absorbance was recorded for the gradient determination (400 nm). (i) Linear plot of integrated PL intensity (taken in the entire wavelength range as shown in the corresponding plot) vs. absorbance at 400 nm with different concentrations of Rhodamine B.

Drop Shape Analysis (DSA) is a method of image analysis used to determine contact angles from images of Milli-Q water droplets or surface tensions or interfacial tensions from images of hanging drops. Additionally, by measuring the contact angles (CA) of different polar liquids, the surface free energy (SFE) of a solid surface can be calculated. DSA involves placing a test liquid droplet on a solid sample (typically used for contact angle measurements) or suspending a droplet on a needle tip (typically used for surface energy measurements). The droplet's image is captured using a camera and then analyzed in software by fitting the contour of the droplet. This process enables the determination of the CA of the droplet on the solid surface or the calculation of the surface tension of the liquid. As illustrated in Figure 5.7, the contact angles for three types of nanoparticles are as follows: for small-sized Au NPs(1.7 nm), it is 25.98°; for Au NPs(1.7 nm)@PLAG, it is

30.85°; and for Au NPs(100 nm), it is 34.68°. These results indicate that different types of nanoparticles exhibit varying wetting behaviors with aqueous. The largest CA is observed for Au NPs(1.7 nm)@PLAG, suggesting relatively weak interactions with aqueous and possessing strong hydrophobicity. Conversely, the smallest CA is found for small-sized Au NPs(1.7 nm), indicating strong interactions with aqueous and good wetting properties. The CA of Au NPs(100 nm) falls between the two, indicating an intermediate level of wetting behavior.

Generally, when the contact angle is less than 90 degrees, these nanoparticles tend to exhibit better adhesion to the cell membrane due to their affinity for the aqueous environment surrounding the cell[97-99]. When hydrophilic nanoparticles come into contact with the cell membrane, they can readily form hydrogen bonds with the hydrophilic head groups of phospholipids, which constitute the lipid bilayer of the cell membrane[100-102].

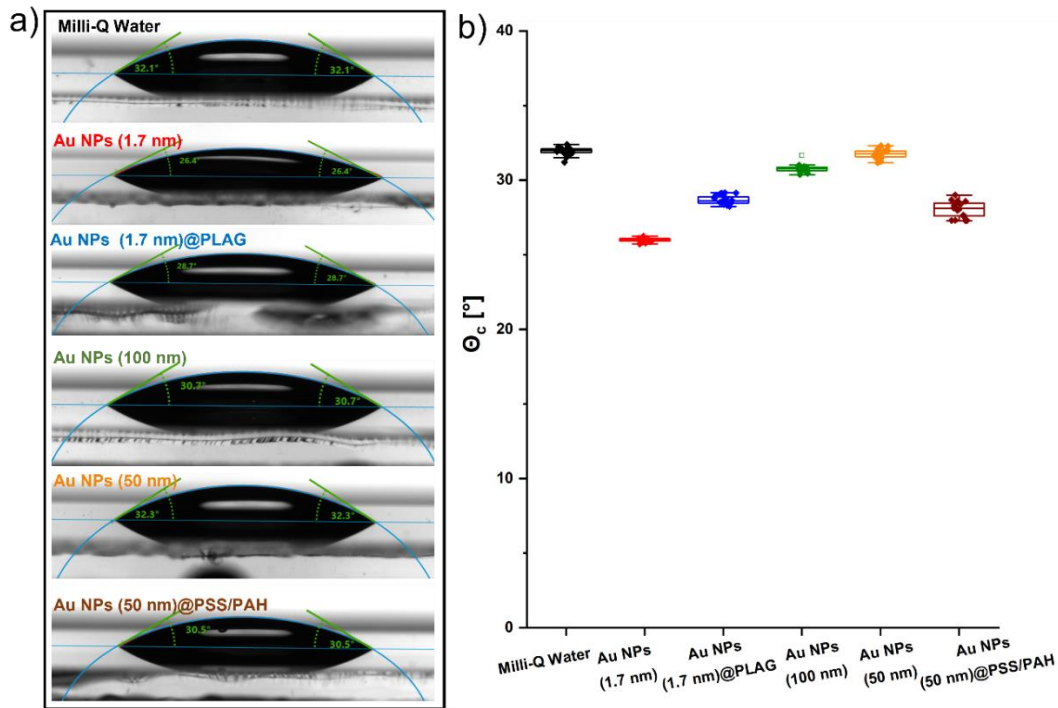


**Figure 5.7.:** (a) The images of CA of 5 nanoparticles (Au NPs(1.7 nm), Au NPs(1.7 nm)@PLAG, Au NPs(100 nm), Au NPs(50 nm) and Au NPs(50 nm)@PSS/PAH) solutions which captured by a high-speed camera. (b) The distribution of data from ten independent measurements,  $n = 10$ .

For thermogravimetric analysis (TGA), the material is heated to a high temperature while simultaneously monitoring the sample's mass, resulting in a decomposition curve. The analysis of the decomposition curve provides information on the oxidation temperature and residual mass of the sample. The oxidation temperature defined here is the temperature at which the majority of the material undergoes decomposition. For carbon-based materials, residual mass or ash content represents the remaining mass of the sample after decomposition. The initial weight loss up to 170 °C is probably due to

removal of water molecules or may be due to the moisture in the sample. In the case of nanomaterials, residual mass may be attributed to inorganic nanoparticles, residual metal catalysts from the synthesis process, or impurities present in the sample. The results for Au NPs(1.7 nm) as compared to Au NPs(1.7 nm)@PLAG are shown in Figure 5.8 Upon heating, the mass of the Au NPs(1.7 nm) decreases, with up to a 65 % mass loss at 500 °C. Interestingly, it is known that Poly-L-Arginin (PLAG), is a secondary amine, and has a pKa close to that of the endosomal compartment within the cell[103, 104]. Which have been reported to be able to enhance transportation into cells. The NPs with polymer matrix (Au NPs (1.7 nm)@PLAG) show a degradation at already lower temperature, which is the onset of polymer desorption. When the temperature rises to 700 °C, the mass loss of Au NPs (100 nm) and Au NPs (50 nm) are negligible, indicating that the residual mass is primarily due to the gold nanoparticles, as gold itself remains stable within this temperature range. In contrast, the shell/matrix Au NPs (1.7 nm)@PLAG exhibits significantly greater mass loss, suggesting that it is primarily composed of carbon-based organic materials, which combust completely at high temperatures, resulting in a 35 % mass loss. Au NPs (50 nm)@PSS/PAH showed that 94 % of the mass could be attributed to Au NPs and 6 % to the mass of Polymer.

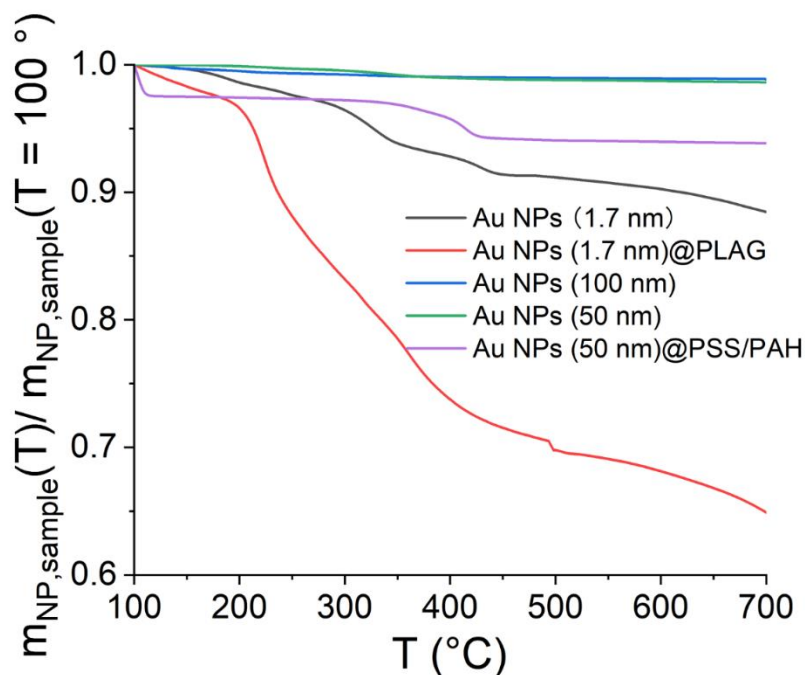


**Figure 5.8.:** TGA experiments quantifying the relative mass loss of 5 nanoparticles (Au NPs(1.7 nm), Au NPs(1.7 nm)@PLAG, Au NPs(100 nm), Au NPs(50 nm) and Au NPs(50 nm)@PSS/PAH).

## 5.5.2. Quantitative Analysis the Content of Au Elements

### 5.5.2.1. Concentration Determination by Inductively Coupled Plasma Mass

#### *Spectrometry (ICP-MS)*

Calibration curves for gold were established using nine concentration points spanning from 2500  $\mu\text{g/mL}$  to 0  $\mu\text{g/mL}$ , employing Agilent element standard solutions. To ensure accuracy and reproducibility, each sample underwent analysis five times. A 10-fold dilution of the NP stock solution was prepared by aspirating 20  $\mu\text{L}$  and adding it to 180  $\mu\text{L}$  of Milli-Q water. Subsequently, 50  $\mu\text{L}$  of the diluted sample underwent digestion with 150

$\mu\text{L}$  of fresh aqua regia ( $\text{HNO}_3$  67 wt %, Fisher Chemical, USA, and  $\text{HCl}$  37 wt %, Fisher Chemical, USA, in a volume ratio of 1:3) overnight. Post-digestion, samples were diluted with 1.8 mL of 2 %  $\text{HCl}$  (37 wt %, Fisher Chemical, USA) to obtain the final sample, which was then transferred to perfluoroalkoxy (PFA) tubes. The elemental concentration of gold was measured using inductively coupled plasma mass spectrometry (ICP-MS) (Agilent 7700 Series, USA).

In this study, mass concentration ( $C_{\text{np}}$ ) serves as the primary metric for quantifying the nanoparticle dose. However, alternative indicators such as number concentration ( $n_{\text{np}}$ ), representing the number of nanoparticles per volume of solution, and molar concentration ( $C_{\text{np}}$ ) can also be utilized.

#### **5.5.2.2. Conjugation Ratio of Capsule-Au**

In our initial experiment, we employed a model system comprising microspheres encapsulated with polyelectrolyte capsules loaded with gold nanoparticles, aiming to quantitatively assess the number of gold nanoparticles within individual polyelectrolyte vesicles.

Initially, a 10  $\mu\text{L}$  aliquot of the diluted sample underwent digestion with 150  $\mu\text{L}$  of freshly prepared aqua regia ( $\text{HNO}_3$  67 wt %, Fisher Chemical, USA, and  $\text{HCl}$  35 wt %, Fisher Chemical, USA) in a volume ratio of 1:3, allowing overnight incubation. The following day, the digested sample was diluted with 1800  $\mu\text{L}$  of diluted nitric acid, and the gold content was quantified using ICP-MS. Concurrently, 10  $\mu\text{L}$  of the diluted samples were assessed using a hemocytometer. Subsequently, we determined the gold content per individual capsule to be 0.632 pg/capsule (mAu(sum)). Utilizing eq 5.5.1, we calculated the total volume of colloidal gold in the diluted sample ( $V_{\text{total}}$ ). Furthermore, leveraging TEM images for information on the radius of the colloidal gold nanoparticles ( $r$ ), we

determined the volume of each individual colloidal nanoparticle ( $V_{NP}$ ) based on equation 5.5.2.

$$v = \frac{mAu}{\rho} \quad \text{eq 5.5.1}$$

$$V_{total} = 0.632e-12 \text{ g} / 19.32 \text{ g/mL} = 3.27e-14 \text{ mL}$$

$$v = \frac{4}{3} \pi r^3 \quad \text{eq 5.5.2}$$

$$V_{NP} = \frac{4}{3} \times 3.14 \times (2e-6 \text{ cm})^3 = 3.35e-17 \text{ mL}$$

Based on the above data, we have obtained the number of gold nanoparticles on each capsule ( $V_{total}/V_{NP}$ ), which is the Conjugation ratio of Capsule-Au. The conjugation ratio of was calculated as 501 NP/capsule. The morphology of Capsules with integrated Au NPs is shown in Figure 5.9.



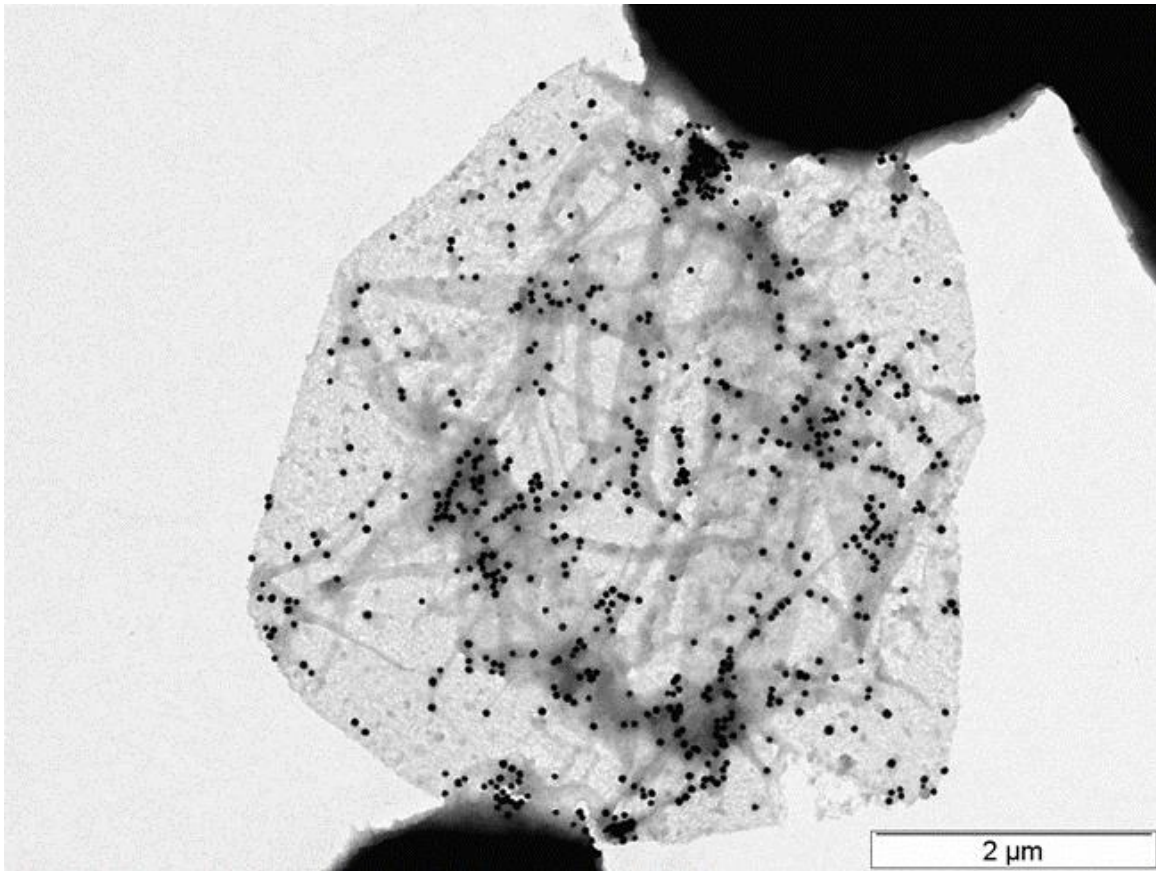


**Figure 5.9.:** TEM images of capsules with integrated Au NPs. Their structure was  $(\text{PSS}/\text{PAH})_2/\text{Au NPs}/\text{PAH}/\text{PSS}$ .

### 5.5.3. Cell Viability of Nanoparticles

The Henrietta Lacks (Hela) cell was selected for this study, and cells were cultured for 24 hours. By individually evaluating the cellular impact of these three nanoparticle variants, we aimed to gain a comprehensive understanding of their actions and toxicity. Data was expressed as mean of triplicate samples and the percentage of cell viability  $V$  was calculated according to eq 5.5.3, where “control cells” are those incubated with DMEM that did not receive any NPs and “test cell” is each well of cells incubated with NPs. The

result of Au NPs(50 nm) and Au NPs(50 nm)@PSS/PAH is presented in Figure 5.10 We found that when the concentration of Au NPs(50 nm)@PSS/PAH reached 50  $\mu\text{g}/\text{ml}$ , significant cell death was caused, and the cell survival rate was reduced by 41.3 %. The result of AuNC, Au NPs(1.7 nm)@PLAG and Au NPs(100 nm) is presented in Figure 5.11.

$$V = 100 * \text{OD (control cells)} / \text{OD (test cells)}$$

eq 5.5.3

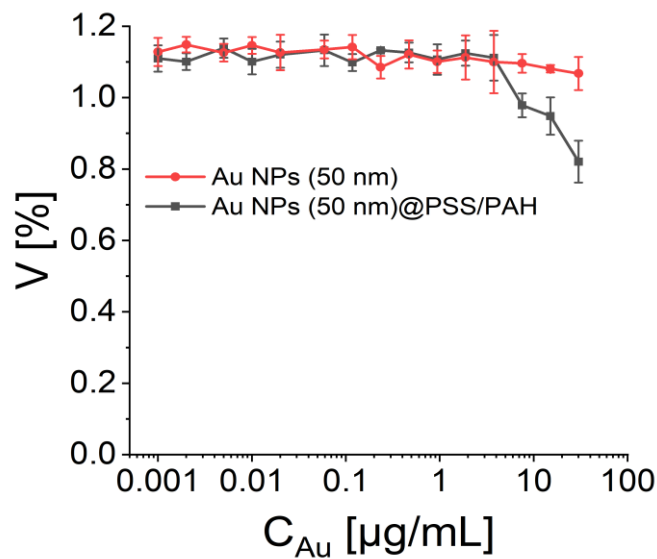


**Figure 5.10.:** Cell viability V of Hela cell exposed to Au NPs (50 nm) and Au NPs (50 nm)@PSS/PAH for 24 hours. Cells were incubated with NPs at different concentrations in DMEM. Data correspond to the mean value and standard deviation of n = 3 measurements.

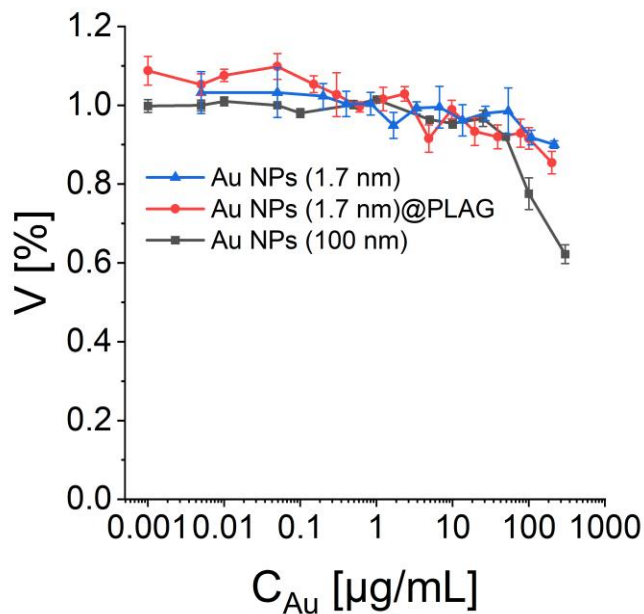


**Figure 5.11.:** Cell viability  $V$  of HeLa cell exposed to Au NPs (1.7 nm), Au NPs (1.7 nm)@PLAG and Au NPs (100 nm) for 24 hours. Cells were incubated with NPs at different concentrations in DMEM. Data correspond to the mean value and standard deviation of  $n = 3$  measurements.

#### 5.5.4. Cell Proliferation upon Exposure to NPs

In the exocytosis studies cells were exposed to NPs at time  $t = 0$  with concentration  $C_{NP}$  and at this time there were  $N_{cell}(t = 0)$  cells present. The cell numbers were determined by first dissolving cells from the plates by trypsinization and then counting cells with a Neubauer counting chamber. Briefly,  $2 \cdot 10^5$  HeLa cells were seeded in 2 mL of DMEM medium in 6 - well plates overnight at  $37^\circ\text{C}$  and 5 %  $\text{CO}_2$ . After 18 hours, the supernatant was collected (2 mL for 6 - well plates) and the cells were washed with PBS for three times. When counting the number of cells in a cell suspension using a counting chamber, the cell

suspension needs to be diluted appropriately (here we used 1:10). This is done to ensure that there are sufficiently few cells in the cells of the counting plate to allow for accurate counting. After this time the cell number increased to  $N_{\text{cell}}(t_{\text{exp}} + 0)$ . Then, the cells were incubated again with fresh medium for the time  $t_{\text{inc}}$ . After this  $t_{\text{inc}}$  the number of cells had increased to  $N_{\text{cell}}(t_{\text{exp}} + t_{\text{inc}})$ . Thus, during the time  $t_{\text{inc}}$  the number of cells had grown by factor  $N_{\text{cell}}(t_{\text{exp}} + t_{\text{inc}})/N_{\text{cell}}(t_{\text{exp}} + 0)$ . Results of Au NPs(50 nm)/Au NPs(50 nm)@PSS/PAH cell exocytosis studies are shown in Figure 5.12. Results of Au NPs(1.7 nm)@PLAG/Au NPs(1.7 nm)/Au NPs(100 nm) cell exocytosis studies are shown in Figure 5.13.

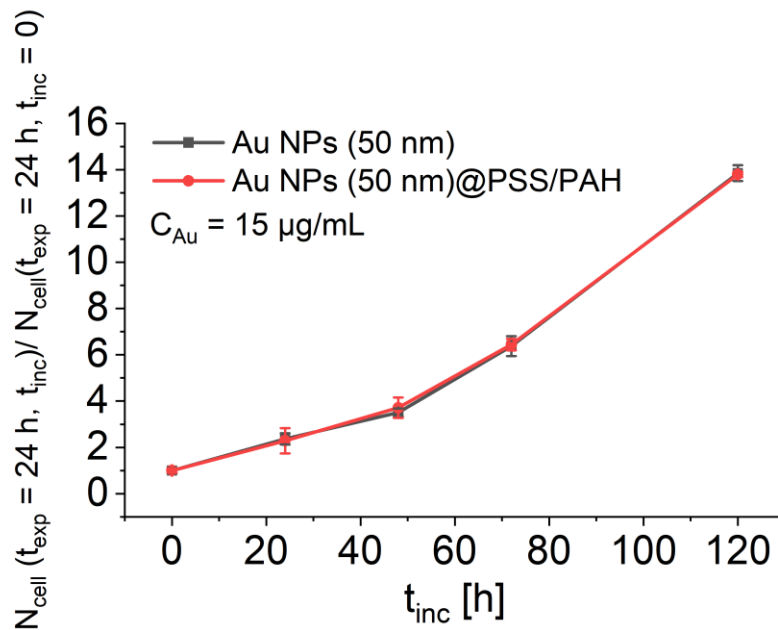


**Figure 5.12.:** Factor  $N_{\text{cell}}(t_{\text{exp}} = 24 \text{ h} + t_{\text{inc}})/N_{\text{cell}}(t_{\text{exp}} = 24 \text{ h} + 0)$  by which the number of cells  $N_{\text{cell}}$  had grown during the incubation time  $t_{\text{inc}}$ .

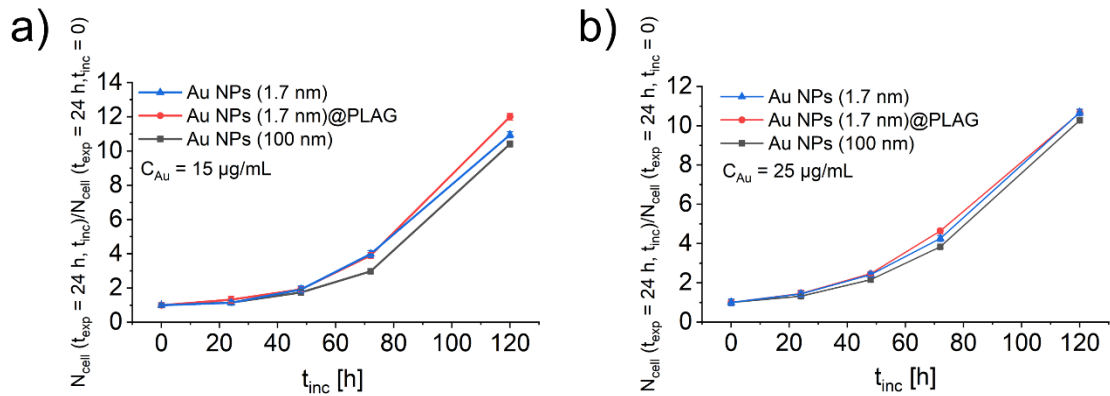


**Figure 5.13.:** Factor  $N_{\text{cell}}(t_{\text{exp}} = 24 \text{ h} + t_{\text{inc}})/N_{\text{cell}}(t_{\text{exp}} = 24 \text{ h} + 0)$  by which the number of cells  $N_{\text{cell}}$  had grown during the incubation time  $t_{\text{inc}}$ .

## 5.6. Endo and Exocytosis Studies Based on NPs with PSS/PAH

### Encapsulation using ICP-MS

#### 5.6.1. Endocytosis Studies Quantification Inside the Cell Based on ICP-MS

The first one comprises polyelectrolyte capsules with integrated gold nanoparticles. The endocytosis efficiency of NPs was assessed by ICP-MS as previously described. Briefly,  $2 \cdot 10^5$  HeLa cells were seeded in 2 mL of medium in 6 - well plates overnight at 37 °C and 5 %  $\text{CO}_2$ . On the second day, the NPs were diluted at different concentrations in DMEM medium and co-incubated for 24 hours. After incubation, the supernatant was collected (2 mL for 6 - well plates) and the cell was washed with PBS for three times. Then added 100  $\mu\text{L}$  of trypsin ethylenediaminetetraacetic acid (0.05% trypsin–EDTA) to each well for 1 minute to detach the cells. Then 1 mL PBS was added to count the number of cells. Finally, the supernatant and cell pellet were collected for ICP-MS measurement. 50  $\mu\text{L}$  of

cell pellet were digested with 150  $\mu\text{L}$  of aqua regia overnight. Samples were then diluted with 1.8 mL of 2 % HCl and then transferred into 6 mL PFA tubes. The samples from the supernatants/cell pellets in the PFA tubes were analyzed by ICP-MS with Argon as flow gas. The obtained experimental results were the mass  $m_{\text{Au}}$  of element gold in the 6 mL solution which  $N_{\text{cell}}$  were detected by counting. Data were shown as mass of element Au found per cell:  $m_{\text{Au}}/N_{\text{cell}}$  [pg/cell], see Figure 5.15 (Cells were counted with a Neubauer counting chamber, data shows in Figure 5.14.). Note that  $C_{\text{intracellular}}$  was the concentration of element Au in cell pellet and  $C_{\text{extracellular}}$  was the concentration of element Au in supernatant.  $C_{\text{added}}$  was the concentration exposed to the cell. Thus, the amount of Au detected in intra/extra cells had grown by factor  $C_{\text{detect}}/C_{\text{added}}$ . The data demonstrated that for low NP concentrations the error in concentration determination was high, leading to errors in the mass balance of detected elements, see Figure 5.16.

The curves shown in Figure 5.16 serve as internal controls.  $C_{\text{Au(intracellular)}}/C_{\text{Au}}$  raises first with increasing concentrations  $C_{\text{Au}}$  to which cells are exposed to NPs, but after a peak  $C_{\text{Au(intracellular)}}/C_{\text{Au}}$  decreases for higher exposure concentrations  $C_{\text{Au}}$ . This is the expected behavior. At low  $C_{\text{Au}}$ , there are not enough NPs in solution which could be internalized by the cells (the lower  $C_{\text{Au}}$ , the lower the probability that a NP touches a cell by Brownian motion and thus the lower the chance for endocytosis). At high  $C_{\text{Au}}$ , there are more NPs in solution that a cell can internalize, i.e. cells are saturated with NPs,  $C_{\text{Au(intracellular)}}$  does not increase anymore and therefore  $C_{\text{Au(intracellular)}}/C_{\text{Au}}$  decreases. The data show, that even under the optimum condition, cells are not able to endocytose all NPs (i.e.  $C_{\text{Au(intracellular)}} \ll C_{\text{Au}}$ ). As additional control the mass balance is visualized. Without losses of NPs (sticking to walls of the petry dishes, pipettes, etc.) and without errors in detection of Au, detection of Au in the extracellular supernatant and the internalized Au should equal the amount of added Au:  $C_{\text{Au(intracellular)}} + C_{\text{Au(extracellular)}} = C_{\text{Au}}$ , or  $C_{\text{Au(intracellular)}}/C_{\text{Au}} + C_{\text{Au(extracellular)}}/C_{\text{Au}} = 1$ . The red lines in Figure 5.16 show the deviations from the values

expected for a mass balanced detection, and the order of the deviations are a quality control for the Au detection. While the data shown in Figure 5.16 show that  $C_{Au(intracellular)}/C_{Au} + C_{Au(extracellular)}/C_{Au} \neq 1$ , the deviations are tolerable and thus data are reliable.

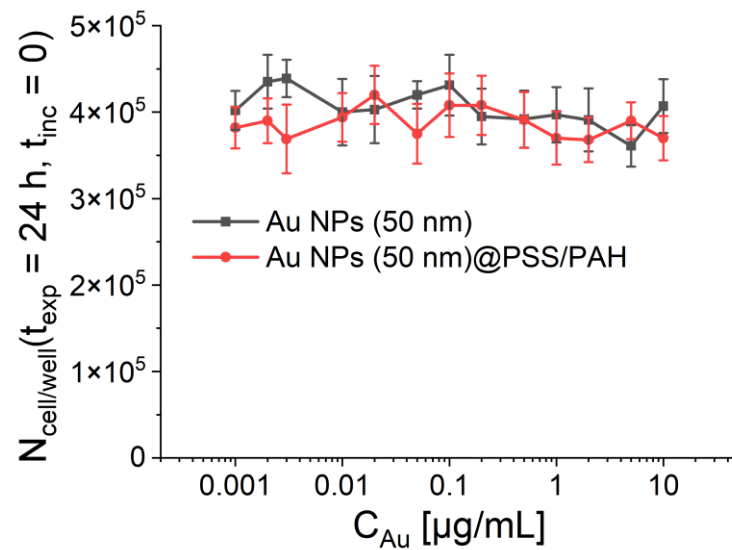


**Figure 5.14.:** Number of cells were exposed to different concentration of NPs (Au NPs(50 nm)/ Au NPs(50 nm)@PSS/PAH) for 24 hours.

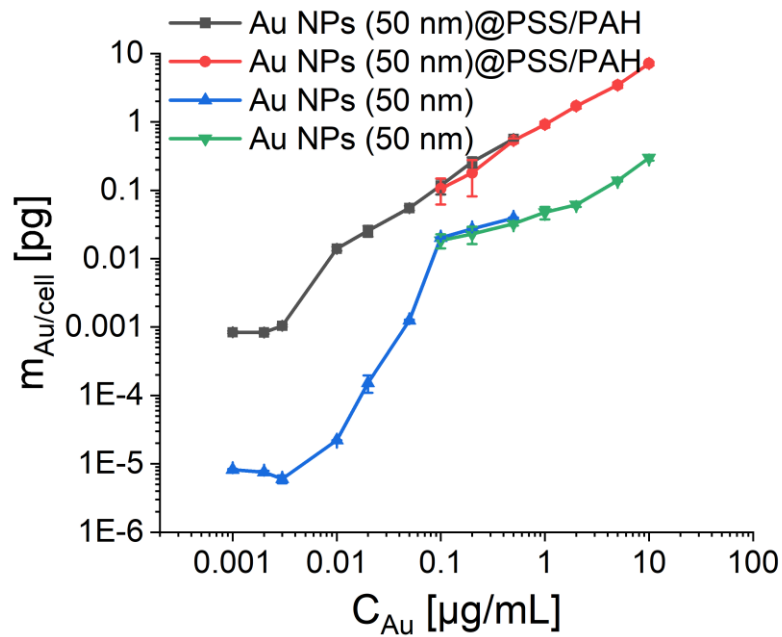


**Figure 5.15.:** Amount  $m_{Au/cell}$  of Au found per cell after exposure of cells to Au NPs (50 nm) and Au NPs (50 nm)@PSS/PAH at exposure concentration  $C_{Au}$  for  $t_{exp} = 24$  h. For both cases, 2 different measurement series are shown, which overlap well.

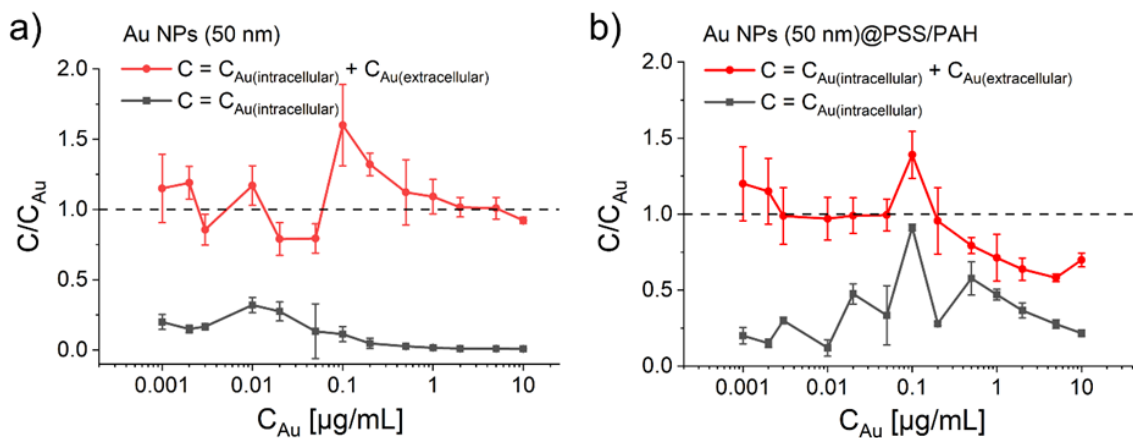


**Figure 5.16.:** Compilation of data from Figure 4.15. The amount of endocytosed NPs in



terms of elemental concentration was detected and divided by the amount of NPs which had been added.

### **5.6.2. Cell Exocytosis Studies Based on NPs with PSS/PAH encapsulation**

To study the degradation efficiency, the cell exocytosis experiment was conducted for evaluation. Briefly, the  $2 \times 10^5$  Hela cells in 2 mL DMEM medium were seeded in 6-well plate overnight at 37 °C and 5 % CO<sub>2</sub>. On the second day, the NPs were diluted at different concentration in DMEM medium and co-incubated for 24 hours. After incubation, the supernatants were discarded and the cells were washed with PBS for three times to remove the noninternalized NPs. Subsequently, the 2 mL fresh DMEM medium was added to each well and incubated for another 24 hours, 48 hours, 72 hours, 120 hours. In case of long incubation times  $t_{inc} = 120$  hours, cells had to be re-seeded during the incubation period, as they had grown to confluence. For the group  $t_{inc} = 120$  hours, after  $t_{inc} = 48$  hours the supernatant above cells was collected. Cells were then washed one time with 2 mL of PBS, detached from the each well with 100  $\mu$ L 0.05 % trypsin-EDTA. After aspiration of the trypsin-EDTA, 1 mL of freshly-medium was added to collect the cells, which were then reseeded in a T-25 flask (growth area per flask 25 cm<sup>2</sup>). The collected supernatant (2 mL) and 2.6 mL of fresh complete cell medium was added, resulting in a final volume of medium of 5.6 mL. Cells were then incubated further for 72 hours, resulting in a total incubation time of  $t_{inc} = 48$  hours + 72 hours = 120 hours. A similar method of digesting the cell pellet was used as §5.6.1. In the first model, we carried out the study model using polyelectrolyte capsules with integrated gold nanoparticles (Au NPs(50 nm)@PSS/PAH). After  $t_{inc} = 120$  hours, the concentration of individual samples was measured by ICP-MS, and the mass of gold element found internalized per cell was

calculated by the formula:  $m_{Au} = C_{(intracellular)}/N_{cell(t_{exp}+t_{inc})}$ . Other presentations of the same data sets but with different representations are shown in (Figure 5.17(b)).

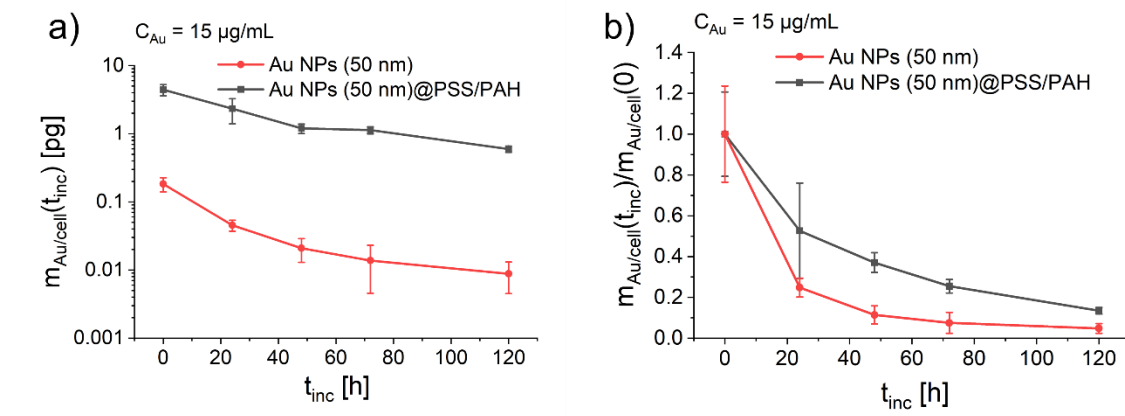


**Figure 5.17.:** (a) After 120 hours of incubation time, the mass of gold elements found internalized per cell, (b) Data corresponding to the ones shown in (a), Here, the data are displayed by dividing the mass of exposed Au elements by the duration of 24 hours of NP exposure.

## 5.7. Endo and Exocytosis Studies Based on NPs with PLAG encapsulation

### 5.7.1. Endocytosis Studies Based on NPs with PLAG encapsulation

We investigated the Au NPs(1.7 nm)@PLAG and Au NPs(100 nm) of the same size. The results of DLS revealed their hydrated particle sizes to be approximately 100 nm, as shown in Figure 5.4. Endocytosis studies on larger gold nanoparticles with similar surface chemistry indicated that internalization was primarily mediated by clathrin-mediated endocytosis[31, 77]. Similar cell endocytosis and fate experiments of NPs as described in

§5.6.1. HeLa cells were seeded in 6 well plates at a density of  $20 \times 10^4$  cell per well. Afterward, the cellular internalization of 2 nm Au NPs(1.7 nm), 100 nm Au NPs(100 nm) and 100 nm Au NPs(1.7 nm)@PLAG was studied for different concentration of NPs (samples were pre-determined for Au element concentration using ICP-MS. Here, all concentrations mentioned are based on the concentration of gold elements) for 24 hours. After incubation, all residual NPs from the medium were washed away and the cells were washed with PBS for three time. Next, 100  $\mu$ L of 0.05% trypsin-EDTA was added to each well and incubated for 1 minute to detach the cells. Subsequently, 1 mL of PBS was added to count the number of cells. Finally, both the supernatant (medium and PBS) and cell pellet were collected for ICP-MS measurement. The quantification of cell endocytosis is presented in Figure 5.18. In the results, we observed a consistently low cellular uptake of individual Au NPs(1.7 nm), while there was a significant increase in cellular uptake after the Au NPs(1.7 nm) were clumped together into nanocomposite. The total internalization amount of Au NPs(1.7 nm) contained in larger nanostructures was almost 9.7 - fold higher compared to the individual Au NPs(1.7 nm) treatment after 24 hours incubation. The corresponding number of cells for each data point are shown in the Figure 5.19. The amount of endocytosed and non-endocytosed NPs in terms of Au element concentration and divided by the amount of Au element were added  $C_{add}$ , which called  $(C_{intracellular} + C_{extracellular} / C_{add})$ . The mount of endocytosed NPs in terms of Au element concentration divided by the amount of Au element added, which was named  $(C_{intracellular} / C_{add})$ . See the Figure 5.20.

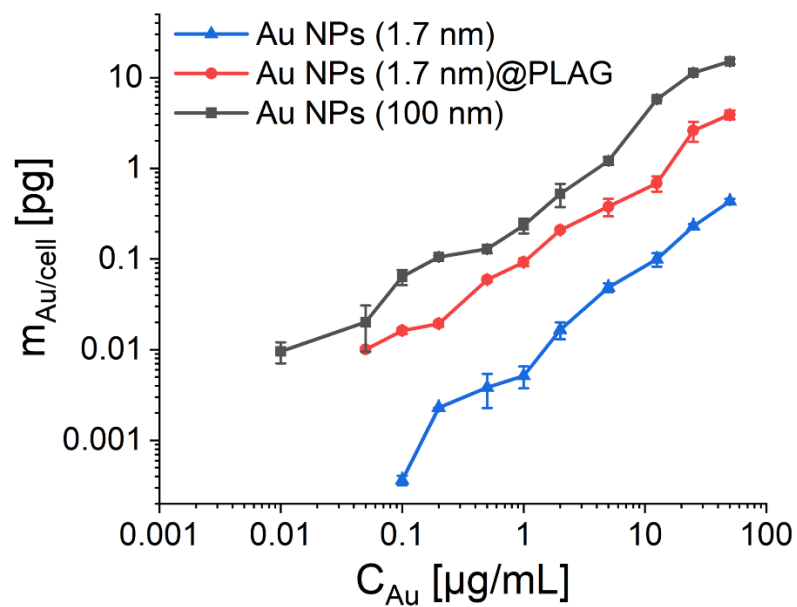


**Figure 5.18.:** Quantification of the uptake of Au NPs(100 nm), Au NPs(1.7 nm)@PLAG and Au NPs(1.7 nm) by HeLa cells. After the exposure time  $t_{exp} = 24$  hours, the cells were pelleted and the mass of Au in the cell pellet were determined by ICP-MS. The data represent the mean value and standard deviation of at least  $n \geq 3$  measurements.

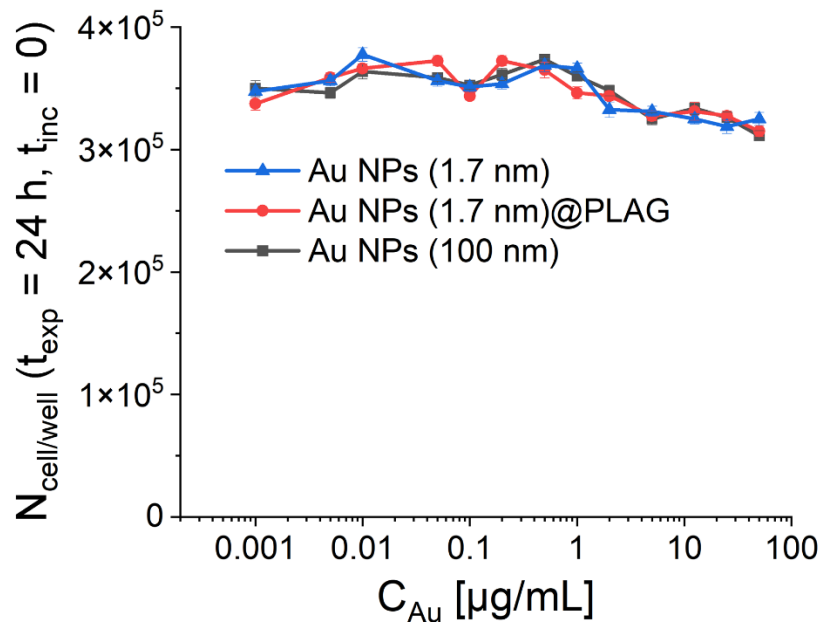


Figure 5.19.: Number of cells were exposed to different concentration of NPs for 24 hours.

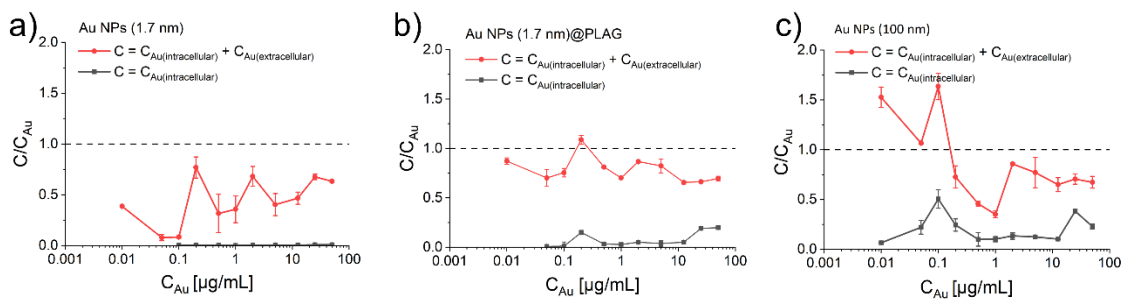


Figure 5.20.: Compilation of data from Figure 5.19. The factor of  $C_{\text{detect}}/C_{\text{add}}$  indicates the relationship between the intracellular and extracellular content of Au elements and the concentration of exposed  $C_{\text{added}}$  after  $t_{\text{exp}}=24$  hours. In the case of correct detection of

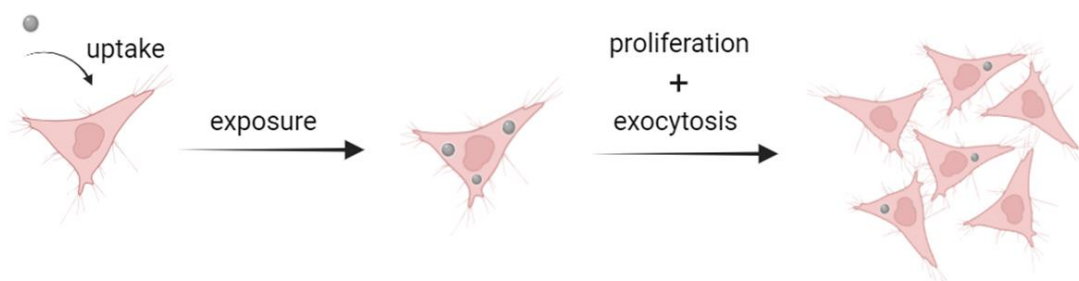
NPs in both the cell pellet and supernatant, the value should be 100 %. However, the data indicates that at low NP concentrations, there is a significant error in concentration determination, leading to inaccuracies in the measured mass balance of the detected elements. As shown in the graph, the data for Au NPs(1.7 nm)@PLAG is close to 100 %, while the data of free Au NPs(1.7 nm) fluctuated more and exhibited higher measurement errors at lower concentrations.

### **5.7.2. Exocytosis Studies Were Conducted Using the Same Exposure**

#### **Concentration**

The cell experiments for exocytosis studies are similar to those for endocytosis experiment described in §5.6. The protocol is illustrated in Scheme 5.2. Firstly, we use nanoparticles at the same concentration (25 µg/mL and 15 µg/mL) and expose the cells to a culture medium containing the nanoparticles for 24 hours ( $t_{\text{exp}} = 24$  hours). Subsequently, the supernatant is aspirated, and the cells are washed with PBS for three times. Then, the 2 mL fresh DMEM medium was added to each well and incubated for 24 hours, 48 hours, 72 hours, 120 hours. In the case of long incubation times, specifically  $t_{\text{inc}} = 120$  hours, cells had to be re-seeded during the incubation period due to reaching confluence. For the group with  $t_{\text{inc}} = 120$  hours, after  $t_{\text{inc}} = 48$  hours, the supernatant above the cells was collected. The cells were then washed once with 2 mL of PBS and detached from each well using 100 µL of 0.05% trypsin-EDTA. After removing the trypsin, 2 mL of medium was added to collect the cell pellet, which was subsequently reseeded in a T-25 flask with a growth area of 25 cm<sup>2</sup> per flask. Finally, 100 µL of 0.05% trypsin-EDTA is added and incubated for 1 minute to detach the cell from each well. The time of cell is  $t_{\text{exp}} + t_{\text{inc}}$ . The cell was collected by centrifugation to the cell pellet. 50 µL of cell pellets were digested overnight with 150 µL of aqua regia. In next day, samples were diluted with

2.8 mL of 2 % HNO<sub>3</sub> and transferred to a 6 mL polypropylene tube. The resulting experimental data represent the mass of Au elements in the 3 mL solution detected by N<sub>cell</sub> counting: mAu [pg/cell].



**Scheme 5.2.:** Work flow for investigating the exocytosis of NPs by cells (exposure with the same concentration of NPs).

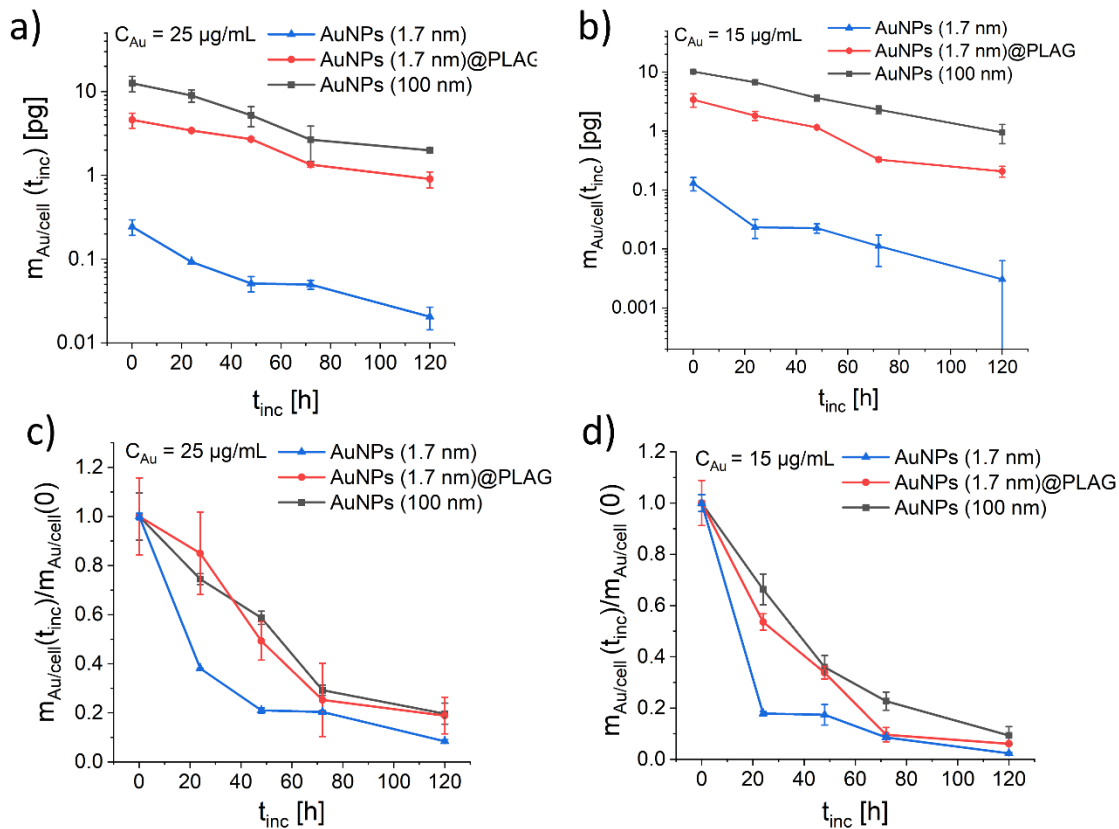


**Figure 5.21.:** a, b) Mass of Au  $m_{Au/cell}$  detected per cell after the time  $t_{inc}$ , in which cells which had been previously loaded with NPs for the time  $t_{exp} = 24$  h at exposure concentration a)  $C_{Au} = 25 \mu\text{g/mL}$  and b)  $C_{Au} = 15 \mu\text{g/mL}$ , were cultivated without the presence of NPs in the medium. c,d) Normalized data from a,b).

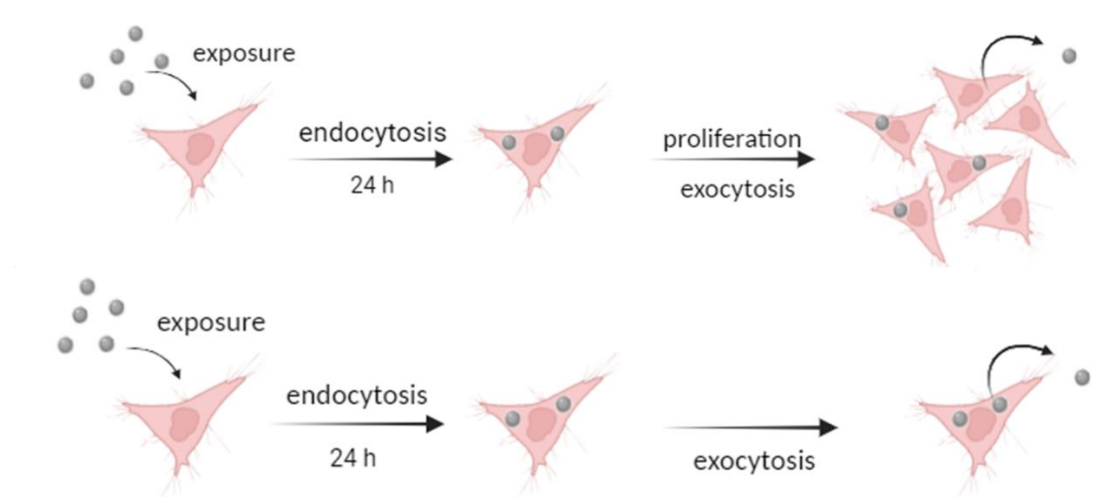
The data obtained above do not exhibit a clear trend, which could be attributed to using the same exposure concentration, resulting in inconsistent intracellular Au concentration during internalization.



### 5.7.3. Exocytosis Studies Using the Different Exposure Concentration

Next, we optimized the experimental design. Here, we selected different exposure concentrations of each NPs based on the cellular uptake concentration (Scheme 5.3). Hela cell were co-incubated with samples of  $C_{Au}(Au\ NPs(1.7\ nm)) = 25\ \mu g/mL$ ,  $C_{Au}(Au\ NPs(1.7\ nm)@PLAG) = 7.5\ \mu g/mL$  and  $C_{Au}(Au\ NPs(100\ nm)) = 2\ \mu g/mL$  for 24 hours. Briefly,  $2 \times 10^5$  Hela cells were seeded in 2 mL of DMEM medium in a 6-well plate and incubated overnight at 37 °C and 5 % CO<sub>2</sub>. On the following day, the NPs were diluted at various concentrations in DMEM medium and incubated with the cells for 24 hours. We used different concentration of NPs exposed the cells and incubated for 24 hours ( $t_{exp} = 24$  hours). After that, the supernatant was removed, and the cells were washed three times with PBS. Subsequently, 2 mL of fresh DMEM medium was added to each well, and the cells were further incubated for 24 hours, 48 hours, 72 hours, and 120 hours. In the case of long incubation times, specifically  $t_{inc} = 120$  hours, cells had to be re-seeded during the incubation period due to reaching confluence. For the group with  $t_{inc} = 120$  hours, after  $t_{inc} = 48$  hours, the supernatant above the cells was collected. The cells were then washed once with 2 mL of PBS and detached from each well using 100  $\mu$ L of 0.05 % trypsin-EDTA. After removing the trypsin, 2 mL of medium was added to collect the cell pellet, which was then reseeded in a T-25 flask with a growth area of 25 cm<sup>2</sup> per flask. Finally, 100  $\mu$ L of 0.05 % trypsin-EDTA was added to each well and incubated for 1 minute to detach the cells. The cells were collected by centrifugation to obtain a cell pellet. 50  $\mu$ L of the cell pellet was digested overnight with 150  $\mu$ L of aqua regia. The next day, the samples were diluted with 2.8 mL of 2 % HNO<sub>3</sub> and transferred to a 6 mL polypropylene tube. The resulting experimental data represents the mass of Au elements in the 3 mL solution detected by  $N_{cell}$  counting:  $m_{Au}$  [pg/cell]. Additionally, we conducted another branch of exocytosis experiments using a cell proliferation blocker (Mitomycin C) to reduce the

number of cells. This was done to compare and eliminate the potential effects of cell efflux caused by an increase in cell numbers. The specific steps of this experiment are as follows: After co-incubation of nanoparticles with cells for 24 hours, the supernatant was aspirated and the cells were washed three times with PBS. 1 mL of DMEM containing the 0.5  $\mu\text{g}$  Mitomycin C was added to the cells, and they were incubated for 1 hour. After 1 hour co-incubation, the supernatant with Mitomycin C was discarded, and the cells were washed three times with PBS. Subsequently, 2 mL of fresh DMEM medium was added to each well, and the cells were further incubated for 24 hours, 48 hours, 72 hours, and 120 hours. Following that, 100  $\mu\text{L}$  of 0.05% trypsin-EDTA was added to each well and incubated for 1 minute to detach the cells. The cells were then collected by centrifugation to obtain a cell pellet. Subsequently, 50  $\mu\text{L}$  of the cell pellet was digested overnight with 150  $\mu\text{L}$  of aqua regia. The next day, the samples were diluted with 2.8 mL of 2 %  $\text{HNO}_3$  and transferred to a 6 mL polypropylene tube. The resulting experimental data represents the mass of gold (Au) elements in the 3 mL solution detected through  $N_{\text{cell}}$  counting:  $m_{\text{Au}}$  [pg/cell].



**Scheme 5.3.:** Work flow for investigating the exocytosis of NPs by cells.

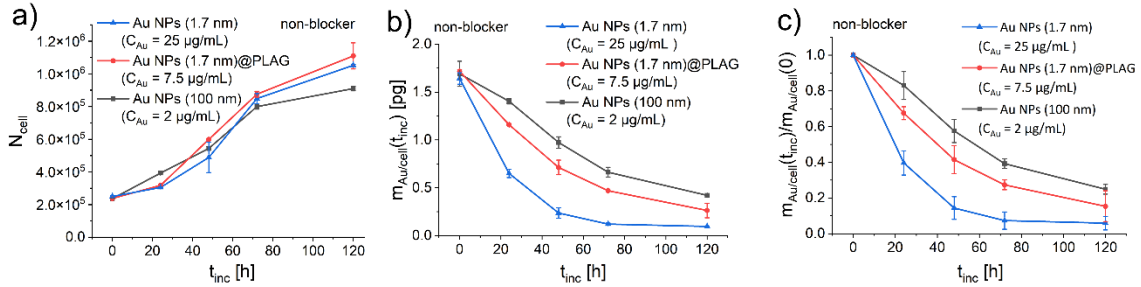


**Figure 5.22.:** a) Quantification of cell proliferation  $N_{cell}(t_{exp} = 24 \text{ hours}, t_{inc})/N_{cell/well}(t_{exp} = 24 \text{ hours}, t_{inc} = 0)$ , similar to Figure S10. b) Mass of Au  $m_{Au/cell}$  detected per cell after the time  $t_{inc}$ , in which cells which had been previously loaded with NPs for the time  $t_{exp} = 24$  hours at exposure concentration  $C_{Au}$  selected differently for the different types of NPs, were cultivated without the presence of NPs in the medium. c) Normalized data from b).

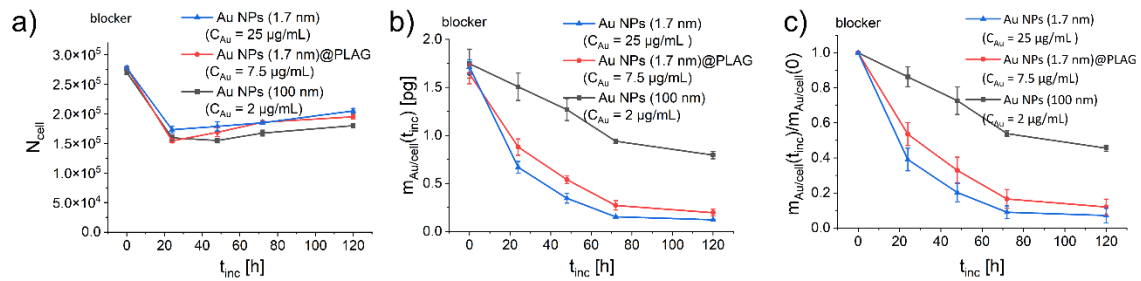


**Figure 5.23.:** a) Quantification of cell proliferation  $N_{cell}(t_{exp} = 24 \text{ hours}, t_{inc})/N_{cell/well}(t_{exp} = 24 \text{ hours}, t_{inc} = 0)$  under presence of a proliferation blocker. b) Mass of Au  $m_{Au/cell}$  detected per cell after the time  $t_{inc}$ , in which cells which had been previously loaded with NPs for the time  $t_{exp} = 24$  hours at exposure concentration  $C_{Au}$  selected differently for the

different types of NPs, were cultivated without the presence of NPs in the medium, but under the presence of a proliferation blocker. c) Normalized data from b).

### 5.8. Degradation Studies Using TEM

To determine the degradation process of Au NPs(1.7 nm)@PLAG upon incubation in different buffers were probed. NPs were immersed in buffers at pH 4.6 (citric acid- $\text{Na}_2\text{HPO}_4$ ) and Milli-Q water at the concentration  $C_{\text{NP}} = 50 \mu\text{g}/\text{mL}$  in the final volume  $V = 0.5 \text{ mL}$ . At exact time point, the samples were sonicated for a short time. A drop of each sample was then dried on the surface of a TEM grid.

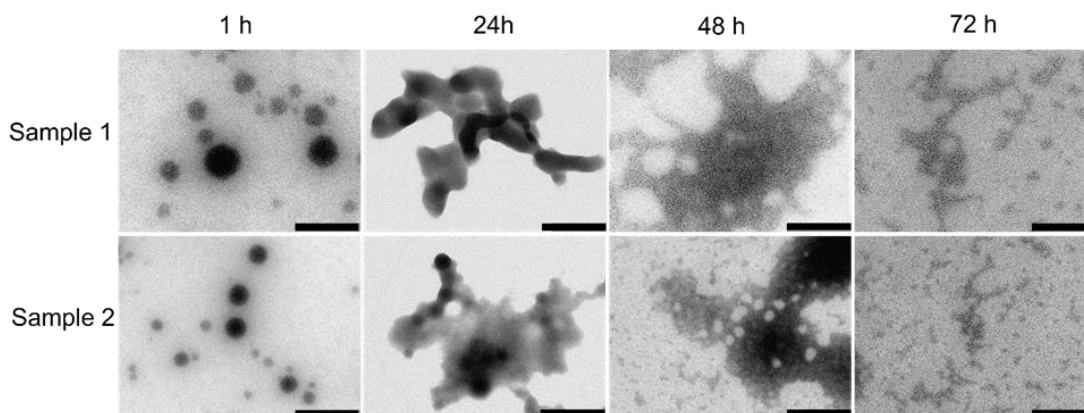


**Figure 5.23.:** TEM images of Au NPs (1.7 nm)@PLAG after exposure to buffer for the time  $t = 1$  hour, 24 hours, 48 hours, 72 hours. The scale bars indicate 100 nm in Sample 1 and 200 nm in Sample 2.

## 5.9. Summary

For a long time, the therapeutic efficacy of nanomedicine has faced significant challenges posed by the complex tumor microenvironment. As mentioned above, the therapeutic efficacy of nanomedicine has faced significant challenges posed by the complex tumor microenvironment. As mentioned above, achieving prolonged circulation in the bloodstream, effective accumulation in tumors through enhanced permeability and retention (EPR) effects, deep penetration into tumors, and efficient cellular uptake simultaneously is nearly impossible for fixed-sized drug delivery system. Recently, the “size relativity” rule has garnered increasing attention within the field of nanomedicine. To overcome multiple biological barriers during the drug delivery, nanomedicine need to be rationally designed. In this work, self-assembled nanoparticles act as multiparticle carriers, which are loaded with numerous ultrasmall therapeutic units.

In summary, we present evidence supporting the superior efficiency of hybrid nanomaterials comprising gold nanocluster in cellular endocytosis compared to individual gold nanocluster. Initially, we successfully synthesized gold nanoclusters around 2 nm, colloidal gold nanoparticles with a size of 100 nm, and hybrid nanocomposite with a size of 100 nm based on gold nanoclusters. The cellular endocytosis efficiency of these nanoparticles was quantitatively assessed using the metal concentration method. Upon comparing the endocytosis efficiency of the aforementioned nanoparticles at the same gold element exposure concentration, it became evident that large-sized hybrid nanocomposite exhibit significantly higher efficiency than small-sized gold nanoclusters. Furthermore, in the examination of cell exocytosis efficiency at the same cell internalization concentration, we observed that the exocytosis efficiency of 100 nm hybrid nanocomposite surpassed that of 100 nm colloidal nanoparticles. This phenomenon can be attributed to the impact of the weakly acidic environment within

intracellular lysosomes, causing nanoassemblies to disintegrate and release small-sized NPs.

## **6. Quantum Dots and FITC Labelled Nanocomposite as a Platform for Biodegradation Studies**

### **6.1. Introduction**

As the fundamental structural and functional unit of living organisms, cells have long been the focus of various research fields. In recent years, foundational research has significantly advanced our understanding of cells at the levels of the entire cell, subcellular structures, and molecular processes[105-108]. Hence, it is imperative to study how the nanomedicines function in cells. In order to further understand the mechanism of action of nanoparticles in cells, it is essential to track their movement trajectory and degradation process, also release of acting molecules within cells[109-111].

Cell tracking, a fundamental technique in cell biology and biomedical research, has evolved significantly over the years. Traditional methods such as transmission electron microscopy (TEM) have provided invaluable insights into cellular structures and dynamics[112, 113]. However, these techniques are often limited in their ability to dynamically track cells in real-time and can be cumbersome, especially when attempting to monitor cellular behavior over extended periods[114, 115]. Additionally, approaches using isotopic elements labeled with radiation, while effective in certain contexts, present safety concerns and are not always suitable for live cell imaging[116-118]. In recent years, advancements in fluorescent imaging technology have revolutionized cell tracking, offering more precise, non-invasive, and real-time monitoring capabilities[119-121]. One such breakthrough involves the use of auto fluorescent nanoparticles and small molecule fluorescent markers, which have emerged as powerful tools in cellular imaging[122]. In the complete system of fluorescence imaging, fluorescent probes, as the core part of basic research, have developed rapidly in recent years. Quantum dots are highly photostable fluorescent semiconductor nanocrystals with a broad absorption spectrum

and a narrow, size-tunable emission spectrum[123-125]. Fluorescein isothiocyanate (FITC), a widely used small molecule fluorescent marker, can be employed to label cells for tracking and visualization in live cell imaging experiments, allowing researchers to monitor cellular behavior and interactions in real-time.

In our study, we synthesized a hybrid NPs, simultaneously encapsulating quantum dots and fluorescent molecules within a nanovesicle. Upon cellular uptake of the composite nanoparticles, in the initial few hours, the fluorescence of red quantum dots and green fluorescent molecules within the cell exhibited co-localization. As the nanoparticles degraded inside the lysosome, the fluorescent groups embedded in the polymer matrix no longer co-localized with the co-embedded quantum dots. We synthesized nanoparticles encapsulated with individual QDs/FITC, introduced them into cells using the same method, and observe the degradation of nanoparticles and subsequent release of fluorescence. This comparative analysis allows us to discern the disparities between auto fluorescent nanoparticles and small molecule fluorescent substances during cellular imaging.

## 6.2. Major Reagents

Name	CAS	Company	Function
Cadmium oxide	#1306-19-0	Sigma Aldrich	For QDs synthesis
Hexylphosphonic acid	#4721-24-8	Sigma Aldrich	For QDs synthesis
Oleic acid	#112-80-1	Sigma Aldrich	For QDs synthesis
Trioctylphosphine oxide	#78-50-2	Sigma Aldrich	For QDs synthesis
Trioctylphosphine	#4731-53-7	Sigma Aldrich	For QDs synthesis
Selenium	#7782-49-2	Sigma Aldrich	For QDs synthesis



1-octadecene	#112-88-9	Sigma Aldrich	For QDs synthesis
Diethylzinc solution	#557-20-0	Sigma Aldrich	For QDs synthesis
Hexamethyldisilathiane	#3385-94-2	Sigma Aldrich	For QDs synthesis
Poly(ethylene glycol) methyl ether-block-poly(lactide-co-glycolide) PEG Mn 2,000, PLGA Mn 4,500		Sigma Aldrich	For nanocomposite synthesis
Polyvinyl alcohol	#9002-89-5	Sigma Aldrich	For nanocomposite synthesis
Bovine Serum Albumin	#9048-46-8	Sigma Aldrich	For nanocomposite synthesis
Fluorescein 5(6)-isothiocyanate	#27072-45-3	Sigma Aldrich	For nanocomposite synthesis
Penicillin-Streptomycin		ThermoFisher	For cell culture
Trypsin-EDTA 0.05%		ThermoFisher	For cell culture
Fetal bovine serum		Biochrom	For cell culture
Dulbecco's Modified Eagles Medium		ThermoFisher	For cell culture
Phosphate-buffered saline		Invitrogen	For cell culture
Resazurin		Sigma-Aldrich	For cytotoxicity

### 6.3. Key Instruments

Name	Model	Company	Function
Dynamic light scattering (DLS)	NANO ZS	Malvern	NPs characterization
UV–vis absorption spectrophotometer	Agilent 8453	Agilent	NPs characterization
Fluorescence Spectrometer	Cary Eclipse	Agilent	NPs characterization
Rotary evaporator	Helzbad Hel-VAP	Heidolph	For NPs synthesis
Sonic Dismembrator	FB-120	Fisherbrand	For NPs synthesis
Laser Scanning Microscope	LSM 980 mit Airyscan 2	ZEISS	For biodegradation studies
Marcoplate reader	FLUOstar Omega	BMG LABTECH	For cellular cytotoxicity studies
Inductively coupled plasma mass spectrometry (ICP-MS)	7700 Series	Agilent	NPs characterization
Transmission electron microscopy (TEM)	JEM-1400PLUS	JEOL	For NPs morphology visualization
Scanning electron microscopy (SEM)	SIGMA	ZEISS	For NPs morphology visualization

### 6.4. Experiments and Methods

#### 6.4.1. Synthesis of Hydrophobic CdSe@ZnS NPs

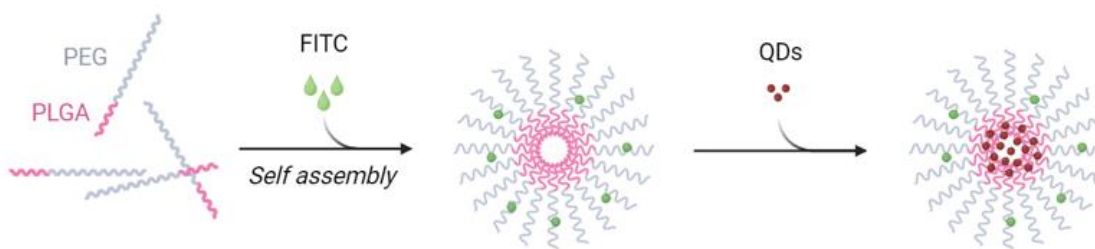
CdSe NPs, so-called quantum dots were synthesized using Cadmium oxide as a precursor, via the procedure described by Peng's group[126, 127]. In a typical synthesis, 0.03 g of

CdO (0.24 mmol), 0.11 g of Hexylphosphonic acid (HPA, 0.66 mmol) and 3.5 g of Trioctylphosphine oxide (TOPO, 9 mmol) were loaded into a 50 mL glass three neck flask connected to a nitrogen line. The mixture was degassed at 120 °C for 20 minutes and then heated to 300 - 320 °C under nitrogen atmosphere for 15 minutes to allow the complete dissolution of CdO in HPA and TOPO leading to a clear and colorless solution. Then, the solution was cooled down to 270 °C, when the desired temperature was reached, 1.2 mL of selenium stock solution was swiftly injected with a syringe. The selenium stock solution was prepared by dissolving 0.0255 g of selenium powder in 1.5 mL of Trioctylphosphine (TOP), to produce a 0.215 M stock solution of Trioctylphosphine selenide (TOP-Se). After injection, the temperature dropped by roughly 10 °C and was maintained then at 250 °C throughout the synthesis of the CdSe core. Every 5 minutes after the injection, the color of the solution turned from colorless to yellow and red, indicating the nucleation of CdSe NPs. UV-vis can be used to determine the growth size of core, when the absorbance value is 592 nm. Once the core had reached the desired size, the reaction could be stopped and washed.

CdSe@CdS NPs, for a shell of CdS grown around the CdSe core[128]. The ODE-S stock solution was prepared by dissolving sulfur powder (0.032 g, 1 mmol) in ODE (10 mL) by sonication for 5 min. CdO (0.0256 g, 2 mmol) and TPA (4.5 mmol) were loaded into a 25 mL three-neck flask with 5 mL ODE. The mixture was heated to 290 °C to obtain a colorless solution. The temperature was reduced to below 150 °C. Purified CdSe core dissolved in ODE was injected into the reaction solution. After the reaction solution was heated to 250 °C, one dose of the ODE-S was dropwise added to the reaction flask at 0.015 mL. The interval between each injection of ODE-S was 15 minutes, and the above step was repeated 5 times. Finally, the final PL emission peak of the CdSe@CdS QDs is approximately 620 nm.

#### 6.4.2. Synthesis of QDs/FITC@mPEG-PLGA NPs

QDs/FITC@mPEG-PLGA NPs was synthesized by the emulsion method (Scheme 6.1). Briefly, 20 mg of mPEG-PLGA dissolved in 1 mL of chloroform, 40  $\mu$ L QDs (CdSe@CdS) and 200  $\mu$ L of Milli-Q water (10 % FITC-BSA) were transferred to a centrifuge tube, and the mixture was emulsified by sonication for 3 minutes. Then the emulsion and polyvinyl alcohol (PVA) solution (2.0 mL, 2 % w/w) were emulsified by sonication for another 5 minutes. The emulsion was then slowly dropped into 10 mL of PVA (0.5 % W/W) and stirred for 10 minutes at room temperature. After vacuum evaporation of the solvent, the NPs were collected by centrifugation at 12,000 rpm for 10 minutes and washed twice using Milli-Q water. The synthesis of QDs@mPEG-PLGA and FITC@mPEG-PLGA nanoparticles is similar to the above step. To unify and simplify the naming of nanoparticles.



**Scheme 6.1.:** Synthetic route of QDs/FITC@mPEG-PLGA nanoparticles.

### 6.4.3. Characterization of QDs@mPEG-PLGA NPs

Hydrodynamic diameters  $d_h$  and zeta-potentials of the QDs/FITC@mPEG-PLGA, QDs@mPEG-PLGA and FITC@mPEG-PLGA were measured on a Zetasizer Nano (Malvern Instrument Ltd.) at 25 °C. For size measurement we used 500  $\mu\text{L}$  of sample, and 800  $\mu\text{L}$  of NP samples were diluted with 200  $\mu\text{L}$  of  $\text{Na}_2\text{HPO}_4\text{-NaH}_2\text{PO}_4$  buffer solution (200 mM, pH 7.4) for zeta-potential measurements.

### 6.4.4. Analyze the DLS Data Using DLS APP

The autocorrelation fit procedure is obtained by DLS originates from the temporal scattering intensity fluctuation based on the scatterer's spatial arrangement. The temporal changing scattering intensity is correlated at certain time points (eq 6.4.1).

$$g_2(\tau) = \frac{[I(t) \cdot I(t+\tau)]}{[I(t)]^2} \quad \text{eq 6.4.1}$$

The  $\tau = (t + \Delta t)$ , the measured intensity  $I(t)$  of a signal at  $\tau=0$  is correlated with itself at a time delay  $I(t+\tau)$ . The normalized intensity correlation is a value between one and zero because of the standardization factor  $[I(t)]^2$ , which is the mean squared of the intensity at the time  $t$ .

#### **6.4.5. pH-dependent Degradation of QDs/FITC@mPEG-PLGA NPs**

The pH-dependent degradation process was assessed by measuring the intensity of UV-vis and fluorescence. Briefly, 10 mg of QDs/FITC@mPEG-PLGA, QDs@mPEG-PLGA and FITC@mPEG-PLGA NP were added to 2 mL of buffer solutions at different pH values, including sodium citrate buffer (citric acid and trisodium citrate, acidic system, pH 3.4) and phosphate-buffered saline (neutral buffer, pH 7.4). The mixture was continuously shaken at room temperature for different time (1 hour, 6 hours, 12 hours, 24 hours, 48 hours). The samples were centrifuged and filtered using a 3 kDa filter (Merck). The filtrate and the sample retained in the filter membrane were collected separately. Both portions of the samples were adjusted to a volume of 1 mL, and their fluorescence and UV-vis absorption spectra were measured.

#### **6.4.6. Cell Culture and Cell Viability**

The human cervical cell line HeLa was provided by ATCC (Manassas, VA, USA) and maintained in Dulbecco's modified Eagle's medium (DMEM, Thermofisher, USA) supplemented with 10 % fetal bovine serum (FBS, Biochrom, Germany), and 1 % penicillin/streptomycin (P/S, Fisher Scientific, Germany) at 37 °C and 5 % CO<sub>2</sub> until the desired cell density was reached. To evaluate the biocompatibility of QDs/FITC@mPEG-PLGA, QDs@mPEG-PLGA and FITC@mPEG-PLGA NP, 7,500 HeLa cells were seeded in 0.1 mL of complete DMEM medium into 96 - well plates (Sarstedt, Germany) with a growth area of 0.34 cm<sup>2</sup> per well overnight. The next day, the medium was removed, and QDs/FITC@mPEG-PLGA, QDs@mPEG-PLGA and FITC@mPEG-PLGA NP in 0.1 mL of fresh DMEM medium with or without added serum were exposed to cells at concentrations. Cell viability was assessed using a previously reported method known as the resazurin assay[129]. Resazurin stock solution was prepared by dissolving resazurin sodium salt

(Sigma Aldrich, No. R7017) in PBS to a concentration of 0.25 mg/mL. After an incubation time (e.g., 24 or 48 hours), cells were washed with PBS ( $V_{\text{PBS}} = 0.1$  mL), and 0.1 mL of resazurin, once added by diluting the resazurin stock solution 10-fold with DMEM medium supplemented with 10 % FBS, was used for the assay. The cells were cultured in medium containing resazurin for 4 hours, during which non-fluorescent resazurin was reduced to highly fluorescent resorufin. Subsequently, a microplate reader (FLUOstar Omega, BMG LABTECH, Germany) was employed to collect the emission fluorescence spectrum of each well in the range of 570 nm to 620 nm, with an excitation wavelength of 560 nm. The results for viability (V) are presented as the fluorescence intensity of cells treated with NPs, normalized to the fluorescence intensity of untreated control cells.

#### **6.4.7. Biodegradation by Laser Scanning Microscope**

In order to determine intracellular degradation of NPs, HeLa cells were seeded into the  $\mu$ -dish (ibidi GmbH, Germany) at a density of  $2 \cdot 10^5$  cells per well in 2 mL DMEM and cultured in the cell culture incubator at 37 °C in 5 % CO<sub>2</sub>. After 12 hours, when the cells had completed adhered to the wells and the previous medium was replaced with the QDs@mPEG-PLGA NPs diluted in DMEM medium supplemented with 10 % FBS or 0 % FBS at a concentration of 400  $\mu\text{g/mL}$ . Subsequently, the suspension containing nonendocytosed NPs was replaced with fresh medium. Finally, the cell images were recorded at different time points (48 hours, 72 hours and 120 hours).

## **6.5. Results and Discussions**

### **6.5.1. The Characterization of NPs**

Initially, we synthesized the CdSe core. In a preheated Cd seed solution, we conducted hot injections of the TOP-se solution at 5-minute intervals. The injection and heating process ceased once the UV-vis peak of the solution reached approximately 592 nm (Figure 6.1 A). Analysis of the UV-vis peak revealed a consistent red shift in position with each injection of the TOP-se solution. Attainment of the desired absorption peak position indicated the achievement of the requisite size for the quantum dot. In our study, we initially synthesized quantum dots with a diameter of 4.5 nm, which were then dissolved in chloroform (Figure 6.2 A)). Subsequently, we conducted emulsion polymerization of the quantum dots and dyes to construct polymer nanomicelles, resulting in the creation of two labeled nanoparticles. Following each synthesis step, we thoroughly characterized the synthesized nanoparticles. The TEM image shows that the diameter of the quantum dots is relatively uniform around 4.5 nm and has good morphology. Using software (Image J, US) to analyze particle sizes, the particle size distribution of the quantum dots is obtained, as shown in the Figure 6.1 (C). After emulsion polymerization, the diameter of nanocomposite is approximately 100 nm, which is also shown in the Figure 6.1 (D).



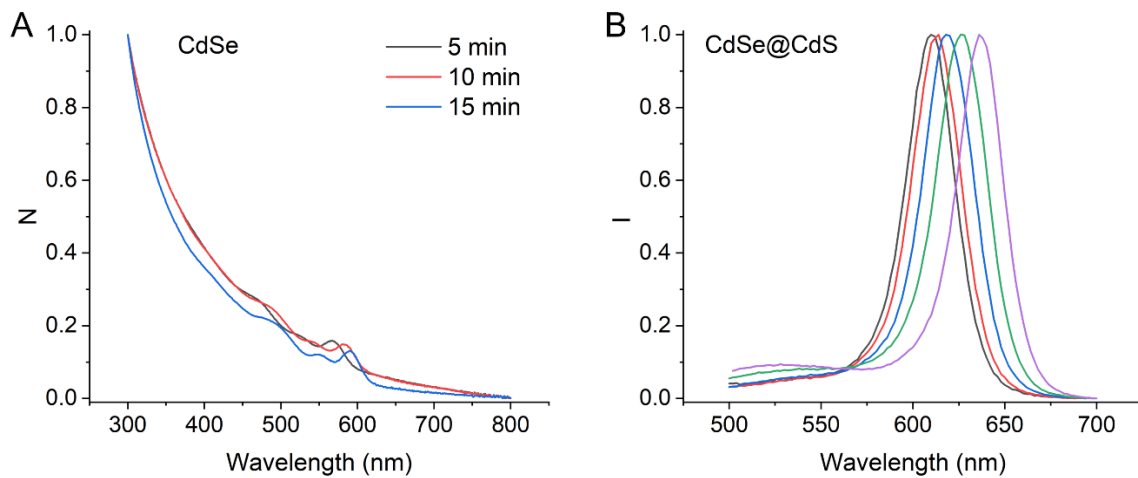


**Figure 6.1.:** (A) UV-vis spectra of the CdSe core at various time points. (B) Photoluminescence (PL) spectra of CdSe@CdS core@shell structures with varying shell growth thickness.

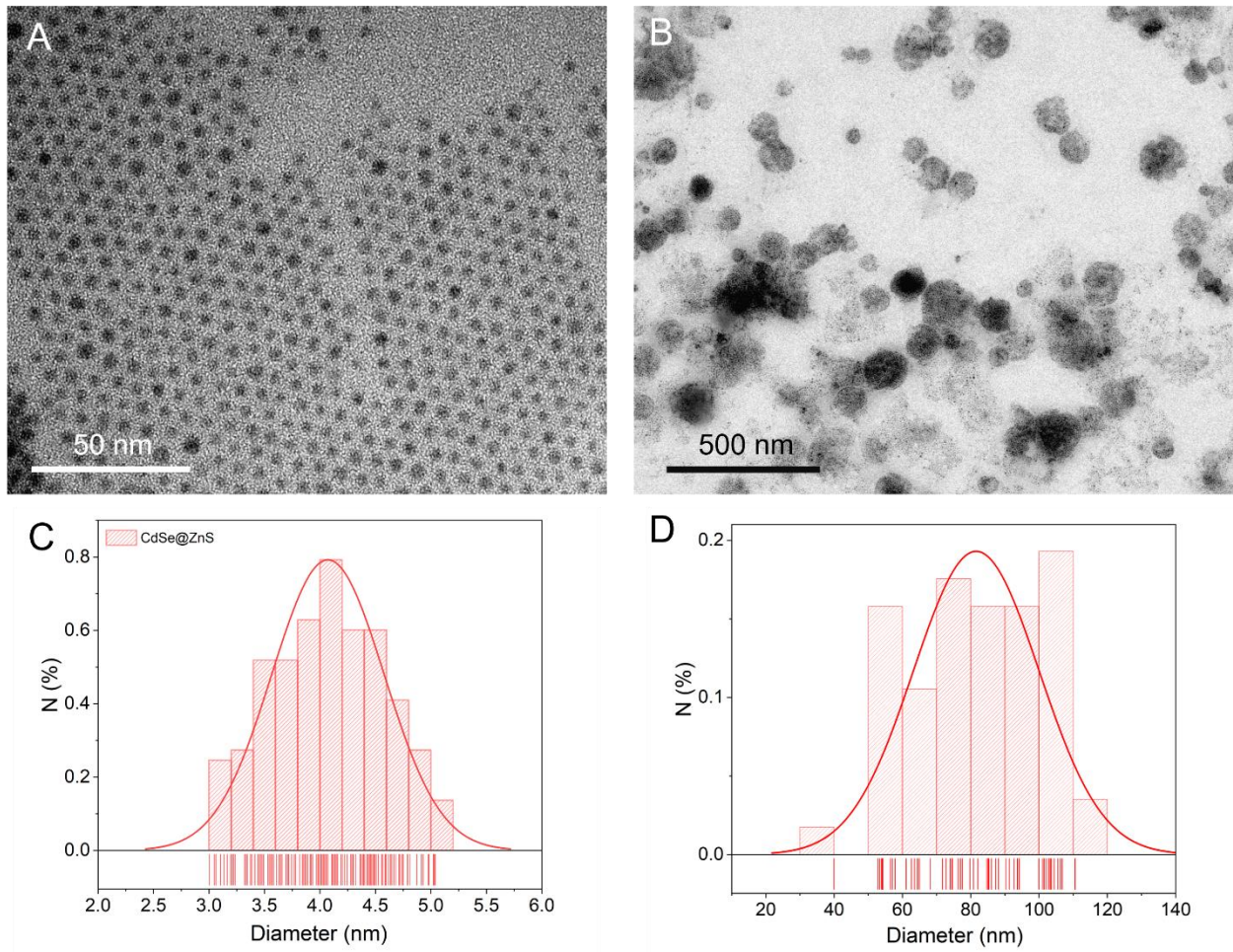


**Figure 6.2.:** The TEM image of QDs (A) and diameter distribution of QDs as measured by TEM (C). and TEM of nanocomposite (B) and diameter distribution of nanocomposite.

Ultrasound is employed to emulsify the two-phase solution, ultimately forming micelles in the hydrophilic phase. The intensity of ultrasound during this synthesis process influences the particle size and uniformity of the final micelles (Figure 6.3). We compared the DLS data of the micelle sizes synthesized at three different amplification strengths. When we use ultrasound amplification at 60 %, the size of the nanocomposite can reach an ultra-large size, exceeding 10  $\mu\text{m}$ . With a decrease in amplification, and keeping the emulsification time constant at 2 minutes, the particle size of the nanoparticles obtained at 20 % amplification is more uniform than that achieved at 40 % amplification. As the amplification increases, microbubbles in the antinodes become smaller, resulting in relatively lower shear. Consequently, shear decreases with the rising sonication frequency[130].

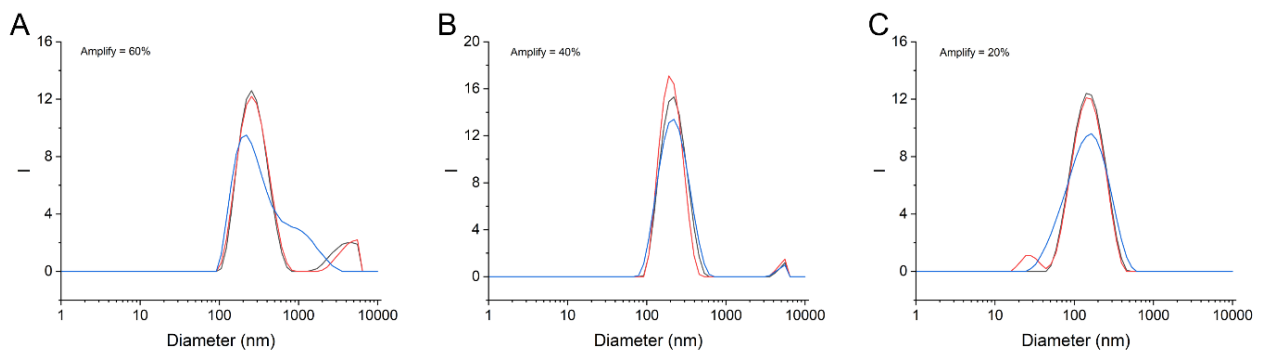


**Figure 6.3.:** The hydrodynamic diameter of nanocomposite as determined with DLS in Milli-Q water. Intensity distribution of amplification of 60 %(A) 40 %(B) and 20 %(C).

For the synthesis of nanoparticles in this research we ultimately chose to use an ultrasound intensity amplification of 20 %. The hydration particle diameter data of QDs/FITC@mPEG-PLGA, QDs@mPEG-PLGA and FITC@mPEG-PLGA are shown in the Figure 6.4. We utilized the DLS App to directly export data measured by the Malvern

particle size analyzer. The fluctuations in dynamic scattering intensity of the particles primarily arise from the change in relative position over time  $g^2(q,t)$ , a result of Brownian motion in the solution.

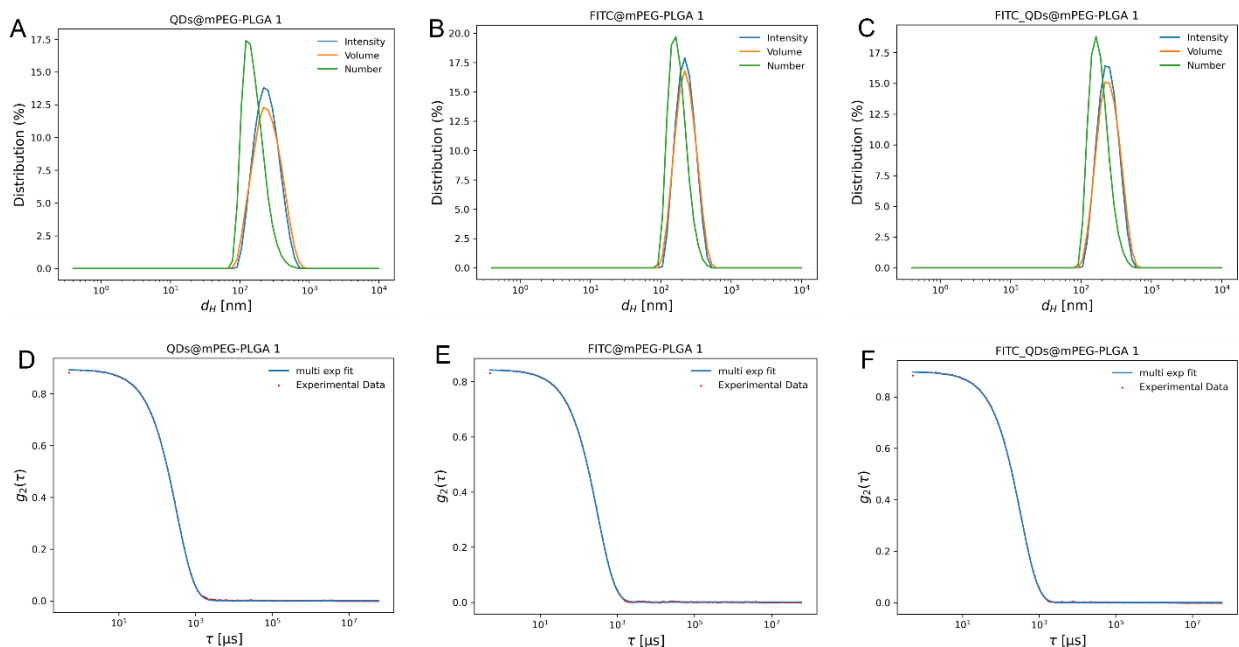


**Figure 6.4.:** The hydrodynamic diameter of nanocomposite as determined with DLS app. (A-C) Utilized the DLS APP to plot Intensity, Volume and Number data combined in one graph. (D-E) depicts the autocorrelation function of fluctuations in particle dynamic information.

### **6.5.2. Colloidal Stability of Nanocomposite**

The aggregation of nanoparticles has a crucial impact on the cellular uptake of nanoparticles. To examine if this could be a possible reason, we tested their colloidal stability. Firstly, we examined the stability of three types of nanoparticles in sodium chloride solution. In biological experiments, salt solutions are often used to provide harsh experimental conditions to test the colloidal stability of a given inorganic nanoparticle, mainly to simulate the internal environment of a biological organism. Typically, a high concentration of salt environment can lead to the aggregation of nanoparticles, which is caused by the weakening of repulsive electrostatic interactions between nanoparticles and the reduced solubility of nanoparticle surface ligands. Therefore, here we used sodium chloride (NaCl) solutions of different concentrations for stability testing. As shown in Figure 6.5 and Figure 6.6, when nanoparticles were exposed to a biologically relevant concentration range of NaCl solution, from 100 mM to 150 mM, even after 24 hours, we did not observe a significant increase in DLS size, indicating the relative stability of the particles.

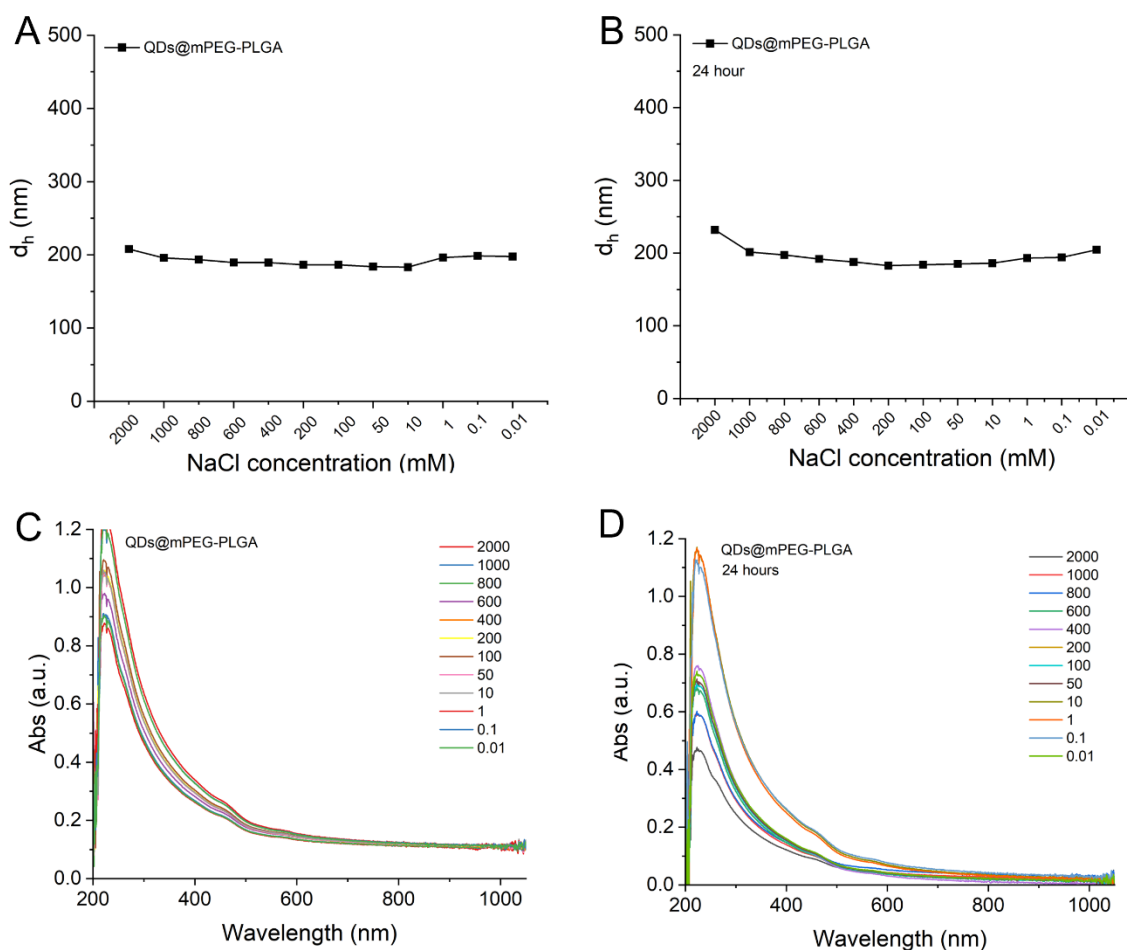


**Figure 6.5.:** The effect of NaCl on the colloidal stability of QDs@mPEG-PLGA was measured by DLS and UV-vis. (A, B) Hydrodynamic diameter ( $d_h$ ) [nm] (number distribution) of QDs@mPEG-PLGA after (A) 0 hour or (B) 24 hours of incubation with NaCl solution at different concentrations. (C, D) UV-vis spectra of QDs@mPEG-PLGA after (C) 0 hour or (D) 24 hours of incubation with NaCl solution at different concentrations.

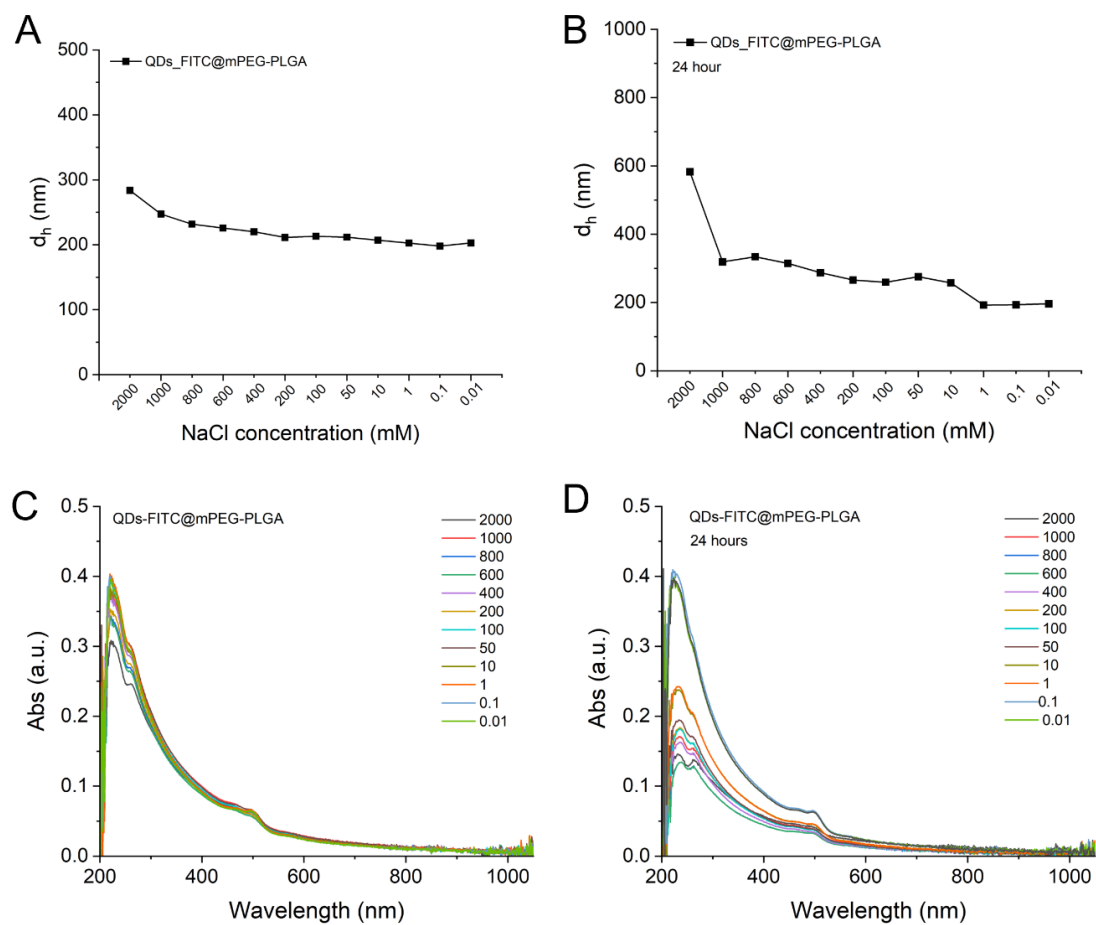
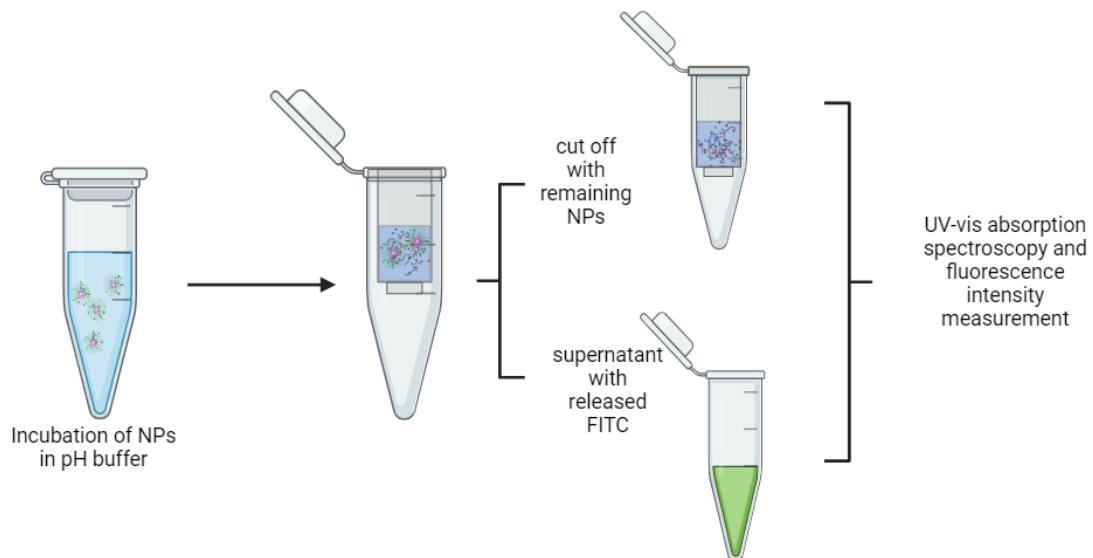


**Figure 6.6.:** The effect of NaCl on the colloidal stability of QDs-FITC@mPEG-PLGA was measured by DLS and UV-vis. (A, B) Hydrodynamic diameter ( $d_h$ ) [nm] (number distribution) of QDs/FITC@mPEG-PLGA after (A) 0 hour or (B) 24 hours of incubation with NaCl solution at different concentrations. (C, D) UV-vis spectra of QDs-FITC@mPEG-PLGA after (C) 0 hour or (D) 24 hours of incubation with NaCl solution at different concentrations.

### **6.5.3. Degradation Behaviors of QDs/FITC@mPEG-PLGA NPs Monitored by Fluorescence**

The pH value is the most characteristic, important, and commonly used internal stimulus in pathological tissues such as tumors and inflammatory tissues. Therefore, exploring the degradation performance and degradation rate of nanoparticles in different pH environments is particularly important. In acidic environments (low pH values), such as within tumor tissues, nanoparticles may undergo faster degradation. This is because acidic environments can induce hydrolysis or degradation reactions in certain materials. This characteristic can be utilized to control drug release, thereby enhancing therapeutic effects and reducing side effects. In neutral or alkaline environments, these nanoparticles may exhibit greater stability, as they are less prone to degradation under these conditions. The design of pH-sensitive nanoparticles can provide a precise drug delivery system, contributing to maximizing therapeutic effects and minimizing impact on surrounding normal tissues. To this end, we have incubated QDs/FITC@mPEG-PLGA in buffered solutions at pH 4.6 and pH 7.4 and analyzed the NP spectrum (fluorescence and UV-Vis) as an indicator of degradation (Scheme 6.2). As illustrated in Figure 6.7, with the effect of acidic conditions, positively charged ions attract the negatively charged segments of the polymer chain, leading to the disintegration of polymer nanoparticles. The degraded nanoparticles undergo centrifugation and filtration with a molecular cut-off capacity of 100 kDa. Owing to their size, QDs face difficulty passing through the filter membrane and entering the lower filtrate, referred to as the supernatant. This is evident when comparing fluorescence spectra. The fluorescence intensity of FITC increases, indicating a significant rise in the amount of FITC in the filtrate. Simultaneously, the fluorescence intensity of particles trapped in the filter membrane remains unchanged. This observation suggests that following nanoparticle degradation, QDs and fluorescent molecules undergo separation, no longer achieving co-localization.





**Scheme 6.2.:** Schematic diagram of the pH-responsive degradation process and analytical methods.

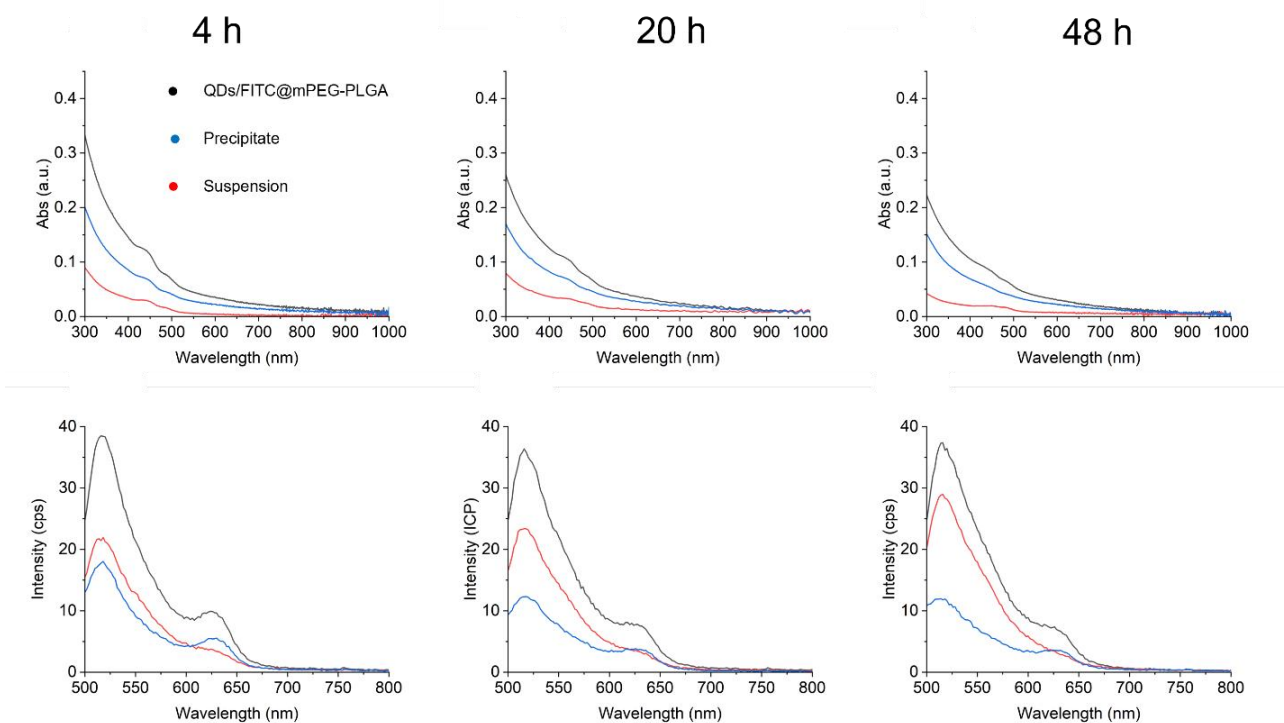


**Figure 6.7.:** The fluorescence and UV-vis spectra of the NPs after degradation in PBS buffer for different times: the blue line represents precipitation, and the red line represents suspension.

#### 6.5.4. TEM Evolution of NPs During the Degradation Process

Subsequently, TEM was used to follow the structural evolution during different time. Briefly, NPs was incubated in 2 mL PBS buffer (pH = 4.6) at 37 °C under mild oscillation. These results indicate that the size of NPs decreases with prolonged degradation time. Additionally, at 80 hours, the erosion of NPs becomes more pronounced, with cracks and defects being more evident compared to the 48 hours (Figure 6.7). The degradation of PLGA may be influenced by hydrophobicity and a semicrystalline structure, which hinder

rapid penetration. The degradation rate is directly proportional to the ester concentration. Therefore, the lactide-rich regions may consist of amorphous or imperfectly oriented crystals, allowing for rapid degradation, while the perfectly crystalline regions degrade at a slower speed.

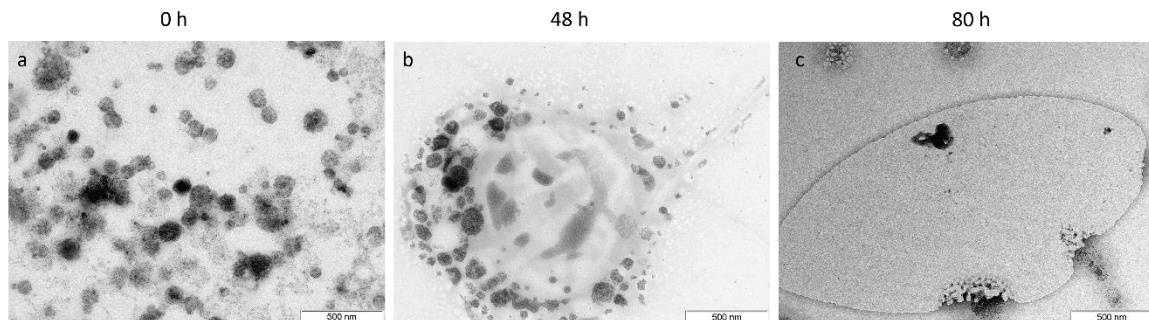


**Figure 6.8.:** One example of the degradation of QDs/FITC@mPEG-PLGA NPs at different time points with label bar 500 nm.

### 6.5.5. Cell Viability of Nanocomposite

To explore the reasonable cultivation range of nanocomposites, we investigated the cytotoxicity of different types of nanocomposites, including QDs@mPEG-PLGA, QDs/FITC@mPEG-PLGA, and FITC@mPEG-PLGA. The cell line chosen for this study was Hela cells, and they were cultured for 24 hours and 48 hours. Separately testing the cell activity of the three types of nanoparticles allows us to gain a clearer understanding of the actions and toxicity of these two nanoparticles. Resazurin, with cell membrane permeability, can enter cells and be reduced to a substance with blue fluorescence inside the cells. As shown in the Figure 6.9 C, it can be observed that the FITC@mPEG-PLGA is non-toxicity, even after co-culturing with cells for 48 hours. However, concerning

quantum dots (QDs) nanoparticles, they are entirely safe for HeLa cells, but at high exposure doses which around 100 mg/mL, they are toxic to HeLa cells. Similarly, from the results Figure 6.9 A, we can see that after co-culturing for 48 hours, QDs@mPEG-PLGA nanoparticles at a concentration of 100 mg/mL caused 35.3 % cell death.

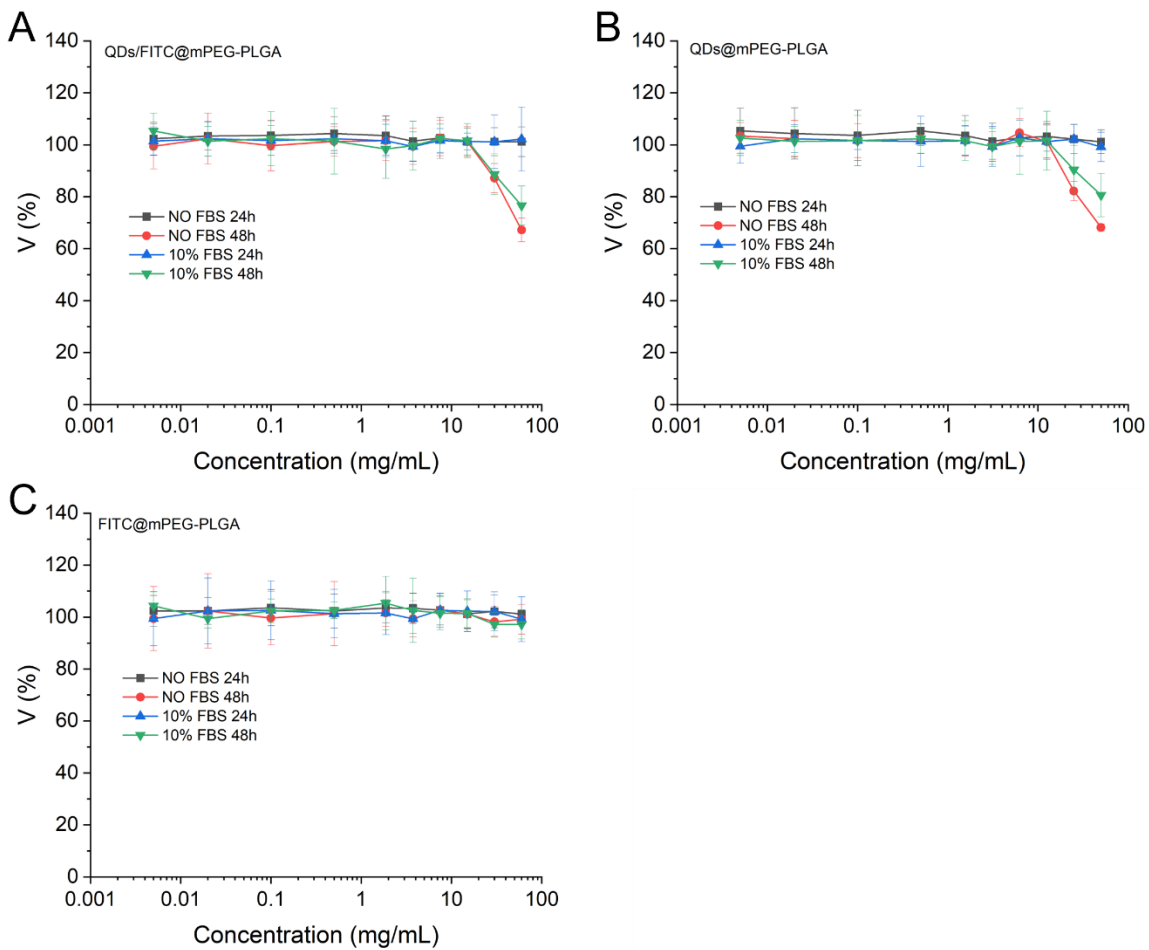


**Figure 6.9.:** Cell viability of HeLa cells after exposed to (A) QDs/FITC@mPEG-PLGA, (B) QDs@mPEG-PLGA and (C) FITC@mPEG-PLGA as measured by resazurin assay. Cells were

incubated with NP at a series of concentrations for 24 or 48 hours in DMEM medium supplemented with and without FBS. Resazurin was added at a final concentration of 0.025 mg/mL and the HeLa cells were further cultured for another 4 hours in cell culture incubator before measured by a microplate reader. Results are showed as percent cell viability  $V$  (%) (mean)  $\pm$  standard deviation (s.d.) from three independent experiments (n=5).

#### **6.5.6. Bioimaging of HeLa Cells Using NPs Nanocomposite**

Most of the nanomaterials-based biomedicine were not translated to the clinics as they failed in the clinical trials due to their non-degradability. Therefore, developing biodegradable materials is extremely important for their potential clinic usage. Therefore, understanding the biodegradability of the bioimaging agents will be crucial to understanding NPs in vivo fate and biodistribution. In this regard, we investigated the biodegradability of QDs/FITC@mPEG-PLGA under a 2-photon microscope, as shown in Figure 6.10. HeLa cells were incubated with NPs for different durations (6 hours and 120 hours), all residual NPs from the medium were washed away and cells were further in fresh cell medium. We conducted a comparative study of intracellular imaging of three types of NPs (QDs/FITC@mPEG-PLGA, QDs@mPEG-PLGA, FITC@mPEG-PLGA) in the same time dimension. The results show that when the exposure time is 6 hours, it can be observed from Figure 6.10 (Figure 6.11 is the lower magnification) that the red fluorescence of QDs and the green fluorescence of FITC are basically co-localized. The entry of NPs into the cytoplasm increased with incubation time. As shown in Figure 6.12, the maximum concentration of NPs was observed along with strong fluorescence localization in the surrounding cell membrane, including cytoplasm, at 24 hours of incubation. Further, the HeLa cells were incubated with 120 hours, the NPs were found to

be degraded within lysosome. This observation is clearly manifested in cellular imaging. Based on the Figure 6.13(Figure 6.14 is the lower magnification), it's evident that FITC fluorescence rapidly diffuses within the cytoplasm, exhibiting a noticeable decrease, approaching disappearance. In contrast, QDs fluorescence consistently remains localized within lysosomes, with its fluorescence intensity relatively higher.

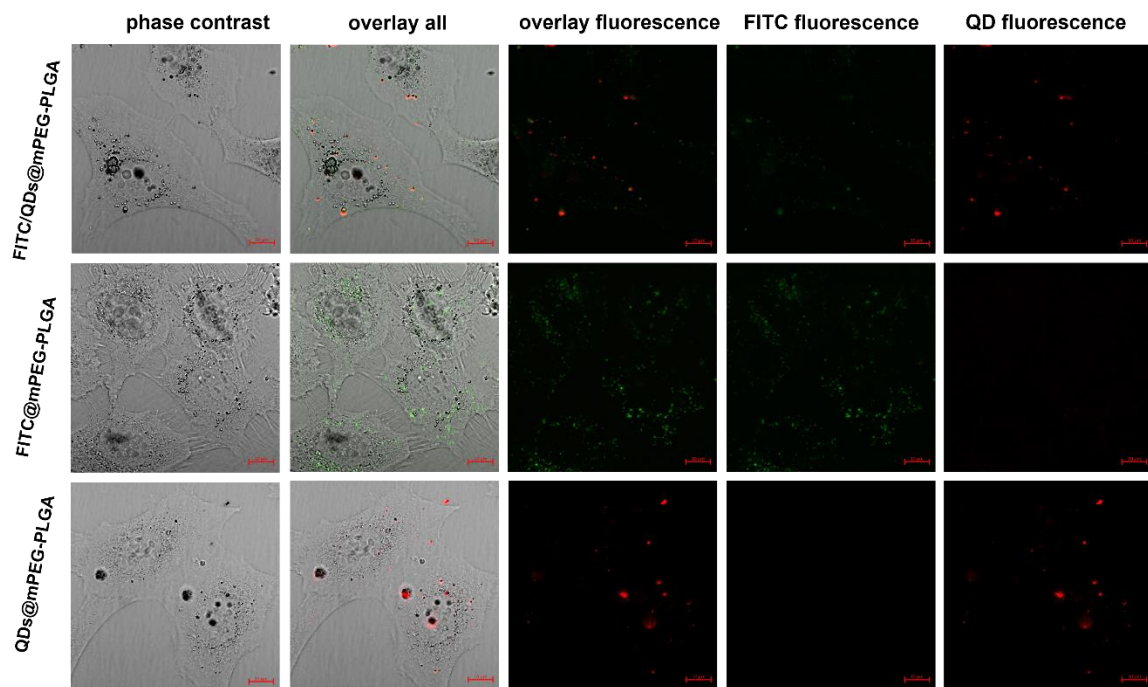


**Figure 6.10.:** The HeLa cell images of NPs (QDs/FITC@mPEG-PLGA, QDs@mPEG-PLGA, FITC@mPEG-PLGA) incubated time for 6 hours. The label bar is 10  $\mu\text{m}$ .

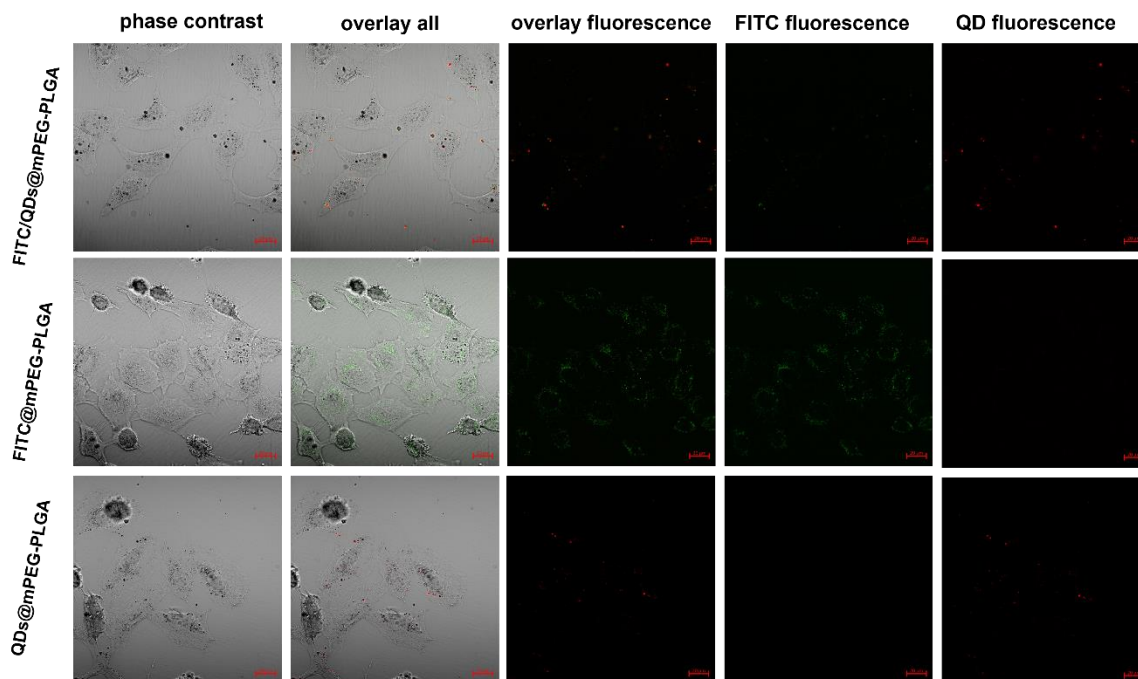


**Figure 6.11.:** The HeLa cell images of NPs (QDs/FITC@mPEG-PLGA, QDs@mPEG-PLGA, FITC@mPEG-PLGA) incubated time for 6 hours. The label bar is 50  $\mu\text{m}$ .

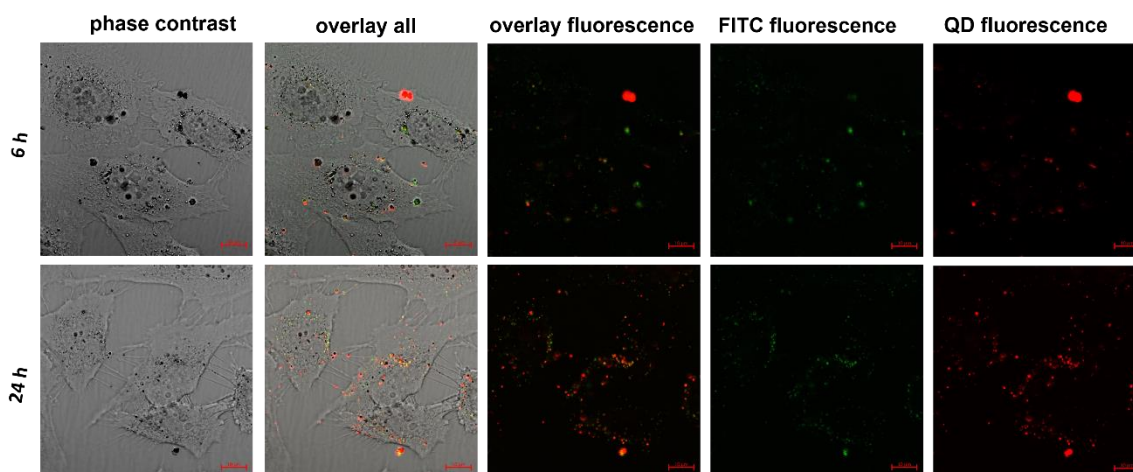


**Figure 6.12.:** The HeLa cell images of QDs/FITC@mPEG-PLGA incubated different times (6 hours and 24 hours). The label bar is 10  $\mu\text{m}$ .

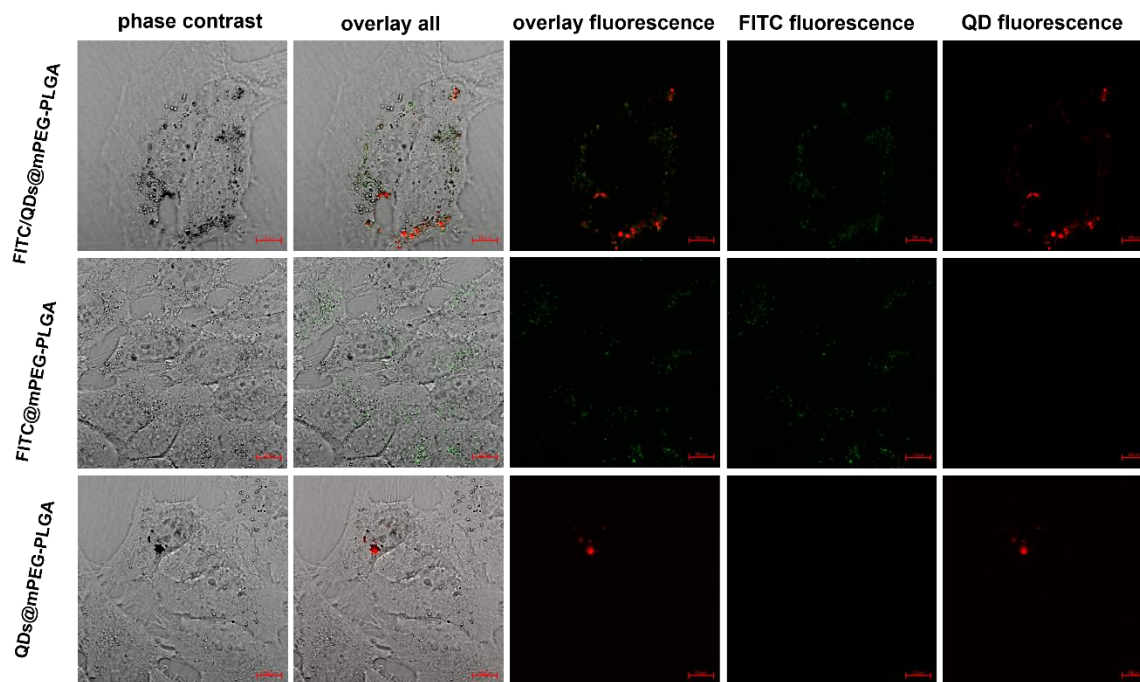


**Figure 6.13.:** The HeLa cell images of NPs (QDs/FITC@mPEG-PLGA, QDs@mPEG-PLGA, FITC@mPEG-PLGA) incubated time for 120 hours. The label bar is 10  $\mu$ m.



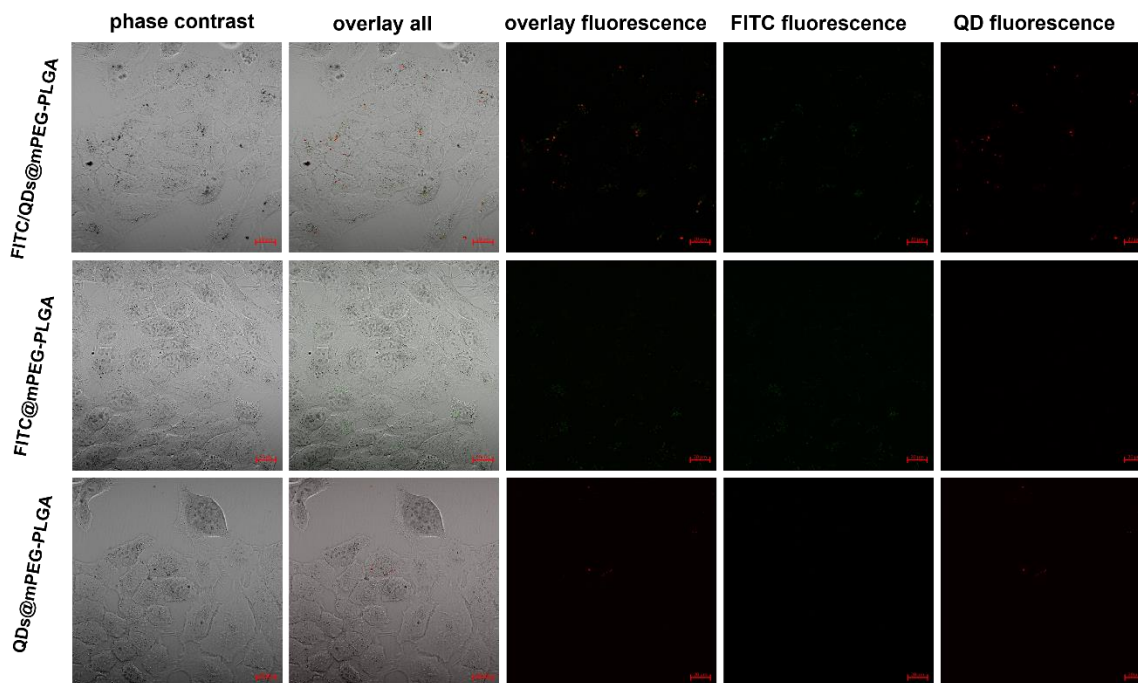


**Figure 6.14.:** The HeLa cell images of NPs (QDs/FITC@mPEG-PLGA, QDs@mPEG-PLGA, FITC@mPEG-PLGA) incubated time for 6 hours. The label bar is 50  $\mu\text{m}$ .

## 6.6. Summary

In this study, we successfully synthesized a novel hybrid nanoparticle that encapsulates small-sized quantum dots and fluorescent molecules within a nanocomposite. Our research results show that upon cellular uptake of these composite nanoparticles, colocalization of red quantum dots and green fluorescent molecules in the cells is observed within the initial few hours. As time progresses and the nanoparticles undergo degradation within the lysosomes, the fluorescent moiety embedded in the polymer matrix no longer colocalizes with the co-embedded quantum dots. This discovery highlights the potential applications of these hybrid nanoparticles, particularly in cellular localization and imaging. Furthermore, our study provides important insights into

understanding the behavior of nanomaterials within biological systems, which is crucial for the development of more effective nanomedicine delivery systems and biomedical imaging techniques. Future research could further explore the performance of these hybrid nanoparticles and evaluate their potential value in biomedical applications.

## **Appendix:**

### **A1. Upconverting Nanoparticles**

#### **A.1.1. Synthesis of Tm-doped Upconversion Nanoparticles.**

NaYF<sub>4</sub>:0.5%Tm, 20% Yb@NaYF<sub>4</sub>:30% Nd, 10%Yb nanocrystals were synthesized using the conventional thermal decomposition method. This type of core-shell structured nanoparticle is synthesized in two steps. Initially, the synthesis involves creating a core with uniform size. Initially, a combined molar quantity of YCl<sub>3</sub> (0.795 mmol), YbCl<sub>3</sub> (0.20 mmol), TmCl<sub>3</sub> (0.005 mmol) and precursors was set to a constant of 1 mmol. Rare earth chlorides, oleic acid (OA, 9 mL), and 1-octadecene (ODE, 15 mL) were combined in a three-necked flask (100 mL). The mixture was heated at 160 °C under vacuum for 30 minutes. After cooling the flask to 25 °C, a methanol solution containing 0.148 g of NH<sub>4</sub>Cl and 0.1 g of NaOH was added dropwise, and the mixture was stirred for approximately 30 minutes. The methanol solution was then evaporated at 60 °C under vacuum. Subsequently, the temperature was raised to 280 °C at a rate of 15 °C min<sup>-1</sup> and maintained at this level for 30 minutes under argon gas protection. After cooling to room temperature, the nanocrystals were collected through centrifugation and washed three times with ethanol/cyclohexane (1/1). Finally, the OA-stabilized core nanocrystals were dispersed in 10 mL of cyclohexane for the next step.

In the second step, YCl<sub>3</sub> (0.6 mmol), YbCl<sub>3</sub> (0.1 mmol), NdCl<sub>3</sub> (0.3 mmol) and CF<sub>3</sub>COONa (1 mmol) were added to a 100 mL three-necked flask to act as a seed for an inert shell. An oleic acid (9 mL) and 1-octadecene (15 mL) mixture with the first step synthetic core nanocrystals was dispersed in 10 mL of cyclohexane. The mixture was heated at 90 °C under vacuum to remove cyclohexane. Subsequently, the solution was heated to 120 °C

and maintained for 30 minutes. The temperature was then increased to 290 °C and held at this level for another 30 minutes. The method for obtaining the precipitated centrifugal purification was the same as for the core nanoparticles described above. Finally, the NaGdF<sub>4</sub>:0.5%Tm@NaYF<sub>4</sub>:20% Yb, 10% Nd nanocrystals were dispersed in 2 mL of trichloromethane for further use.

### **A.1.2. Surface Modification of Poly(isobutylene-alt-maleic anhydride)**

#### **PMA**

We use the same amphiphilic polymer for surface modification. The synthesis steps of poly(isobutylene-alt-maleic anhydride) PMA are consistent with those shown in 5.3.4. PMA and UCNP in a 100 mL flask containing chloroform and evaporate through rotary evaporation. Repeat this evaporation process three times. Add SSB buffer (pH = 12) to the dried flask until all NPs on the flask walls are dissolved. Finally, centrifuge at 9000 rpm for 20 minutes, repeat three times, and purify the NPs.

### **A.1.3. Characterization of Colloidal Properties**

The colloidal properties of the UCNPs were characterized according to our standard protocols[131], including determination of the hydrodynamic diameter ( $d_h$ ) by DLS and the zeta-potential ( $\zeta$ ) by laser doppler anemometry (LDA) the stability in salt-containing solution.

#### A.1.4. Results

As depicted in Figure A 1.1, the TEM image illustrates that NaYF<sub>4</sub>:0.5%Tm, 20%Yb@NaYF<sub>4</sub>:30% Nd, 10%Yb is composed of well-dispersed nanoparticles, exhibiting an average diameter of 40 nm. Analysis of the TEM results reveals the high uniformity in both size and morphology of these nanoparticles. The average sizes of obtained NaYF<sub>4</sub>:0.5%Tm, 20%Yb (Figure A.1.2a), NaYF<sub>4</sub>:0.5%Tm, 20%Yb@NaYF<sub>4</sub>:30% Nd, 10%Yb (Figure A.1.2b) are 21 and 30.6 nm, respectively.

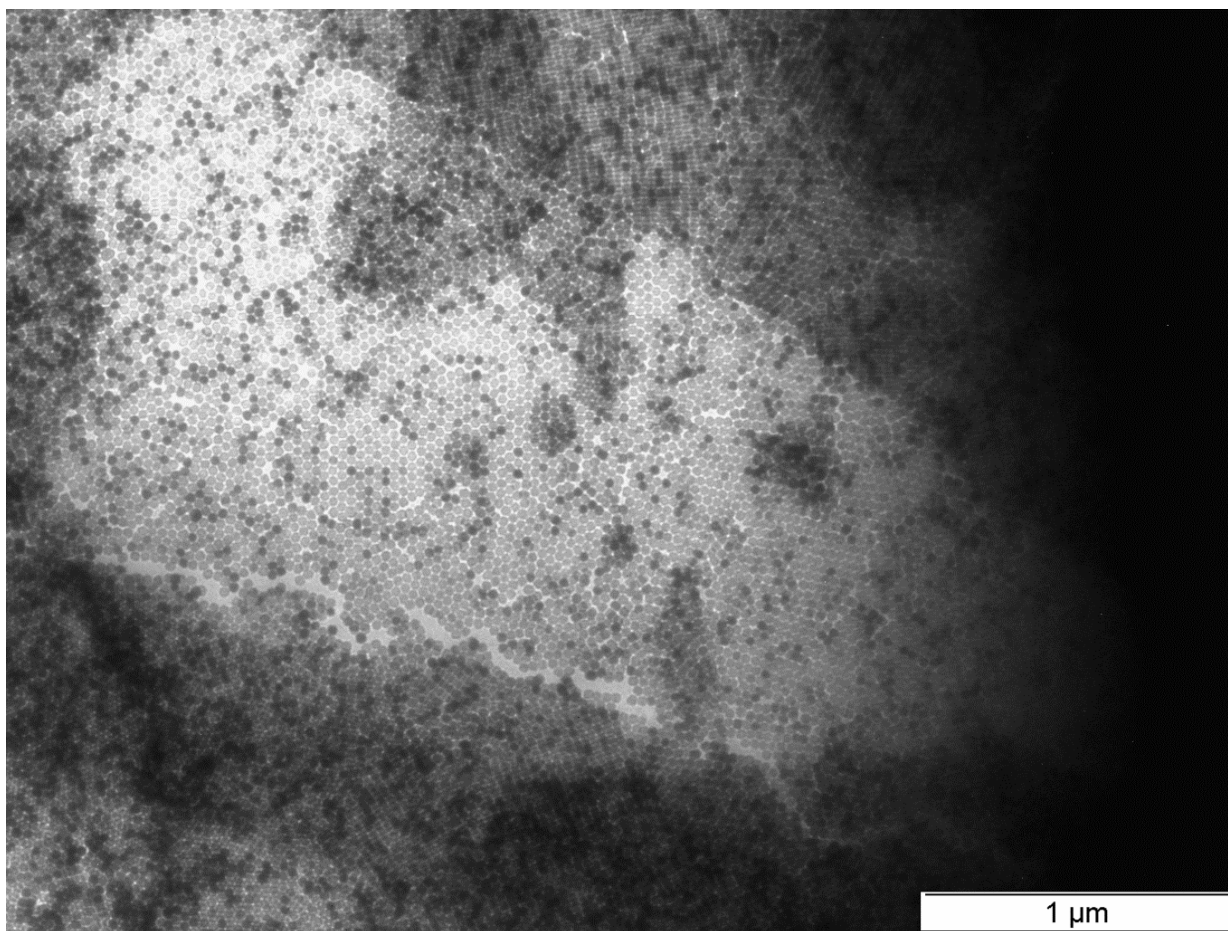


**Figure A.1.1.:** The transmission electron microscopy (TEM) image of UCNP reveals a wide field of view, with a scale bar set at 1 μm.

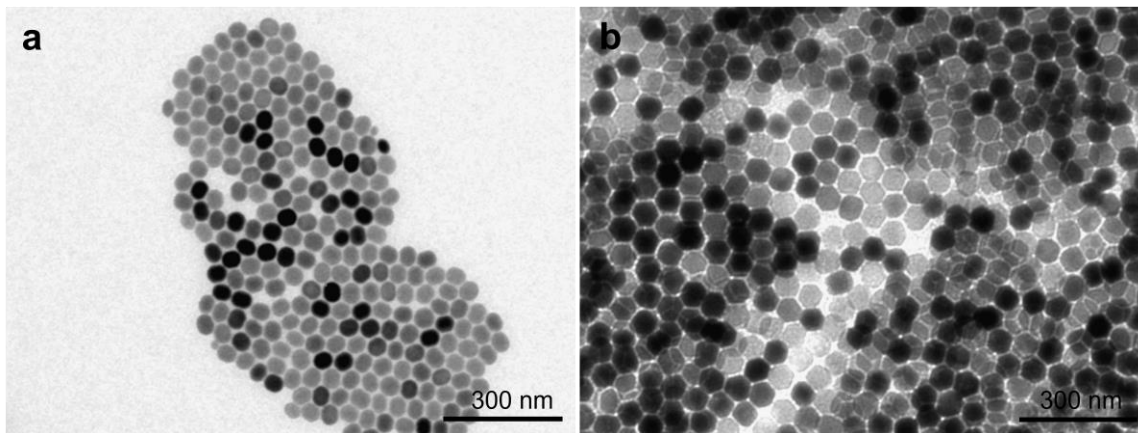


**Figure A.1.2.:** The transmission electron microscopy (TEM) image of UCNP reveals a higher magnification of view, with a scale bar set at 50 nm.

Upconverting nanoparticles (UCNP) exhibit unique luminescent properties due to their special electronic structure and energy level distribution. When these nanoparticles are exposed to excitation light, electrons are excited to higher energy states, and then they return to lower energy states by emitting photons through a radiative process, resulting in luminescence[132, 133]. For UCNP, the excitation light at different wavelengths leads to different energy level transitions, generating emission light at different wavelengths. Although the position of the maximum emission peak is typically fixed, the variation in luminescent intensity is due to transitions between different energy levels under excitation light of varying wavelengths[35]. This versatility makes UCNP widely applicable in areas such as biosensing and bioimaging. As illustrated in Figure A.1.3., we employed various wavelengths of excitation light to stimulate the UCNP. Remarkably, we observed that the excitation light at 794 nm resulted in the most intense emission light. Correspondingly, UCNP also have a strong absorption peak at 794 nm (Figure A.1.4.), which also corresponds to the fact that under the excitation of 794 nm laser, the emission peak intensity of UCNP is the highest.

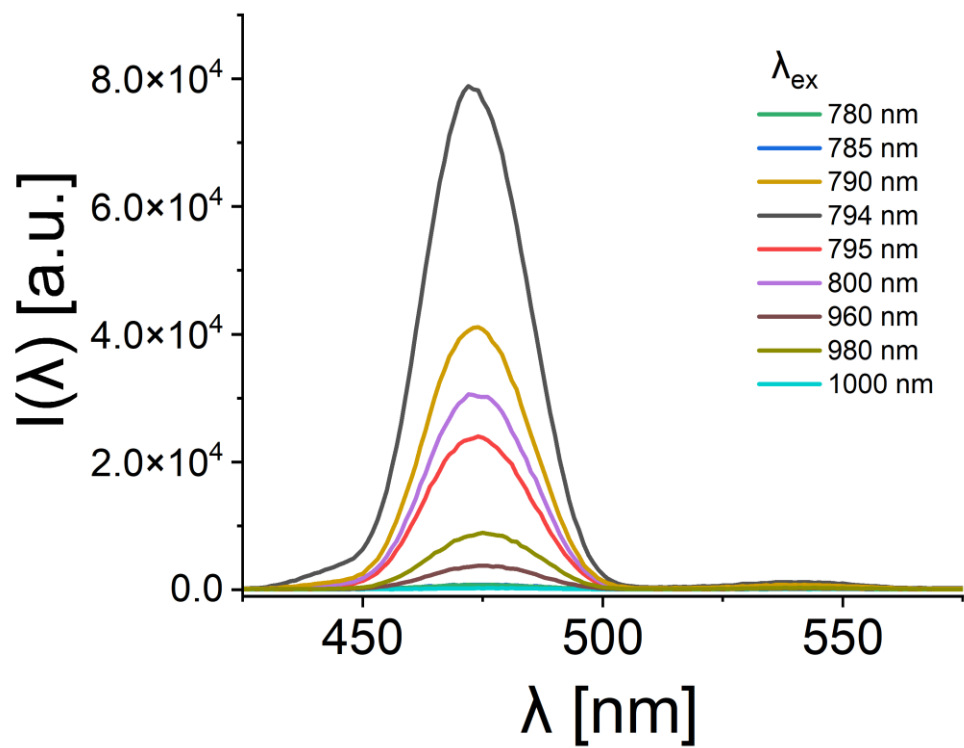


**Figure A.1.3.:** Upconversion luminescence spectra of UCNPs under variable laser excitation.

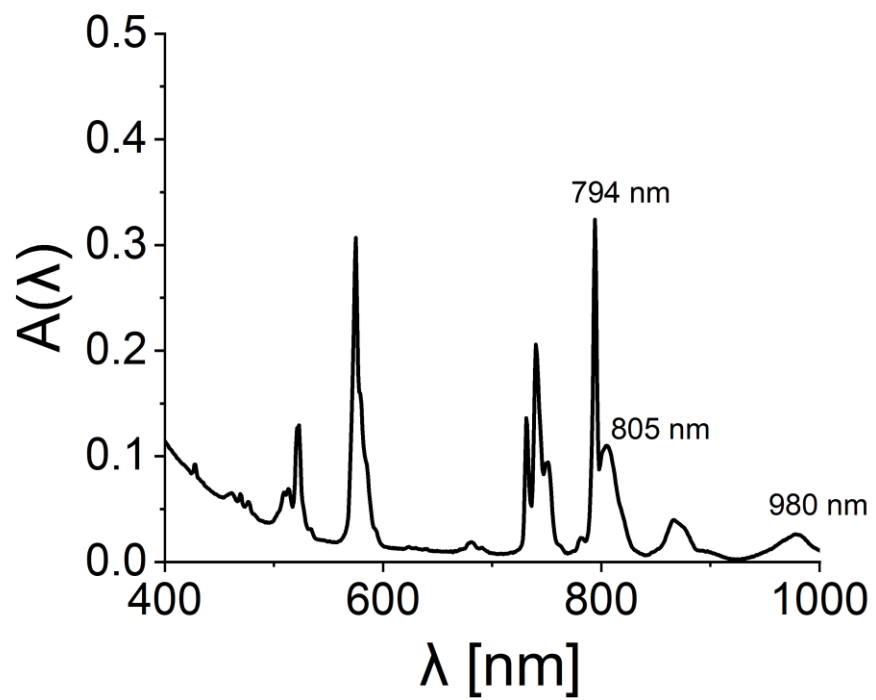









Figure A.1.4.: UV-vis spectra of UCNP.















## List of Hazardous Substances

### List of Chemicals and GHS Classifications.

Substance	Signal word	GHS-symbols	Hazard statements	Precautionary statements
Chloroauric Acid	Danger		H290 - H302 - H314 - H373 - H411	P260 - P273 - P280 - P303 + P361 + P353 - P305 + P351 + P338 - P314
Chloroform	Danger		H302 - H315 - H319 - H331 - H336 - H351 - H361d - H372	P202 - P301 + P312 - P302 + P352 - P304 + P340 + P311 - P305 + P351 + P338 - P308 + P313
Cadmium oxide	Danger		H330 - H341 - H350 - H361fd - H372 - H410	P202 - P260 - P264 - P270 - P273 - P304 + P340 + P310
Hexylphosphonic acid	Warning		H315 - H319	P264 - P280 - P302 + P352 - P305 + P351 + P338 - P332 + P313 - P337 + P313
Trioctylphosphine oxide	Danger		H315 - H318 - H412	P264 - P273 - P280 - P302 + P352 - P305 + P351 + P338 - P332 + P313
Trioctylphosphine	Danger		H314	
Selenium	Danger		H301 + H331 - H373 - H413	P260 - P264 - P273 - P301 + P310 - P304 +

				P340 + P311 - P314
1-octadecene	Danger		H304	P301 + P310 - P331 - P405 - P501
Diethylzinc solution	Danger		H225 - H250 - H260 - H304 - H314 - H336 - H361f - H373 - H411	P210 - P231 + P232 - P280 - P301 + P330 + P331 - P303 + P361 + P353 - P304 + P340 + P310 - P305 + P351 + P338 - P370 + P378
Hexamethyldisilathiane	Danger		H226 - H301 + H311 + H331	P210 - P233 - P280 - P301 + P310 - P303 + P361 + P353 - P304 + P340 + P311
Hydrochloric acid	Danger		H290 - H314 - H335	P234 - P261 - P271 - P280 - P303 + P361 + P353 - P305 + P351 + P338
Nitric acid	Danger		H272 - H290 - H314 - H331	P210 - P220 - P280 - P303 + P361 + P353 - P304 + P340 + P310 - P305 + P351 + P338
Ethanol	Danger		H225 - H319	P210 - P233 - P240 - P241 - P242 - P305 + P351 + P338
1- dodecanethiol	Danger		H314 - H317 - H410	P261 - P272 - P273 - P280 - P303 + P361 +

				P353 - P305 + P351 + P338
N,N-Dimethyldodecylamine	Danger		H302 - H314 - H410	P270 - P273 - P280 - P301 + P312 - P303 + P361 + P353 - P305 + P351 + P338
Gadolinium(III) chloride	Warning		H315	P264 - P280 - P302 + P352 - P332 + P313 - P362 + P364
Thulium(III) chloride	Warning		H315 - H319 - H335	P261 - P264 - P271 - P280 - P302 + P352 - P305 + P351 + P338
Neodymium(III) chloride	Warning		H315 - H319 - H335	P261 - P264 - P271 - P280 - P302 + P352 - P305 + P351 + P338
Ytterbium(III) chloride	Warning		H315	P264 - P280 - P302 + P352 - P332 + P313 - P362 + P364
Cyclohexane	Danger		H225 - H304 - H315 - H336 - H410	P210 - P233 - P273 - P301 + P310 - P303 + P361 + P353 - P331
Sodium trifluoroacetate	Warning		H411	P273 - P391 - P501
Ammonium chloride	Warning		H302 - H319	P264 - P270 - P280 - P301 + P312 - P305 + P351 + P338 - P337 + P313

Sodium hydroxide	Danger		H290 - H314	P234 - P260 - P280 - P303 + P361 + P353 - P304 + P340 + P310 - P305 + P351 + P338
Methanol	Danger		H225 - H301 + H311 + H331 - H370	P210 - P233 - P280 - P301 + P310 - P303 + P361 + P353 - P304 + P340 + P311
Tetrahydrofuran	Danger		H225 - H302 - H319 - H335 - H336 - H351	P202 - P210 - P233 - P301 + P312 - P305 + P351 + P338 - P308 + P313
Toluene	Danger		H225 - H304 - H315 - H336 - H361d - H373 - H412	P202 - P210 - P273 - P301 + P310 - P303 + P361 + P353 - P331

## **Acknowledgements**

My Ph.D. journey is reaching its culmination, and in this moment, I wish to express profound gratitude to my supervisor, Prof. Dr. Wolfgang J. Parak, whose generous mentorship enabled me to delve into compelling research for my doctoral studies. I am deeply thankful for his unwavering guidance, encouragement, and support. His expertise, patience, and dedication were pivotal in shaping this research and navigating me through its challenges.

I extend my gratitude to my co-supervisor, Prof. Dr. Nils Huse, for his invaluable insights and suggestions throughout my Ph.D. studies and thesis development. I am also grateful for his support at the technical level, which has provided tremendous help in the SEM testing part of my work.

I am sincerely appreciative of Dr. Florian Schulz for his meticulous guidance and expert support, which have facilitated my academic growth and enriched my experience. His assistance in testing TEM samples and patiently teaching me SEM techniques has been invaluable. I am also grateful to Dr. Indranath Chakraborty for his guidance and support during the initial year of my Ph.D. journey.

Thanks to Stefen Werner for kindly taking the TEM images, and thanks Dr. Yang Liu and Dr. Bing Qi for teaching me the operation of ICP-MS. Thanks to Maria Pozzi for teaching me the operation of two photon microscopy.

Furthermore, I wish to acknowledge the colleagues of the Biophotonik Group, whose companionship has provided warmth and solace during our shared academic endeavors in a foreign land. Thanks to my group friends Dr. Ferdinand Otto, Kaiwei Lin, Marie-Charlot Dalchow, Maya Luongo, Yuxuan Han, Nils Dageförde, Marvin Skiba, Jinrui Li, Wenbo Wang, Xin Liu, Ben Otange, Juan Jesus Barrios, Sarodi Jonak Dutta and Martin Sosniok for the

companionship and encouragement. Together, we have faced academic challenges, celebrated achievements, and forged enduring friendships. Special thanks to Chenxi Yang for always providing me with emotional support and experimental assistance during PhD study.

I am sincerely thankful to the Chinese Scholarship Council (CSC) and the University of Hamburg for their financial support throughout my Ph.D. studies. Their assistance has been invaluable and deeply appreciated.

I extend heartfelt thanks to myself for the unwavering dedication and efforts invested in this journey, enriching the experience. Additionally, I express my deepest appreciation to my beloved parents for their boundless support, both emotionally and financially, enabling me to wholeheartedly pursue my academic aspirations.

In conclusion, I am profoundly grateful for this invaluable experience. The journey has been marked by challenges and accomplishments, and I will forever cherish the years devoted to pursuing my doctoral degree in Germany.

## Reference

1. Hoffmann, M., et al., *SARS-CoV-2 cell entry depends on ACE2 and TMPRSS2 and is blocked by a clinically proven protease inhibitor*. *cell*, 2020. **181**(2): p. 271-280. e8.
2. Pardi, N., et al., *mRNA vaccines—a new era in vaccinology*. *Nature reviews Drug discovery*, 2018. **17**(4): p. 261-279.
3. Neuwelt, A., et al., *Iron-based superparamagnetic nanoparticle contrast agents for MRI of infection and inflammation*. *AJR. American journal of roentgenology*, 2015. **204**(3): p. W302.
4. Bashir, M.R., et al., *Emerging applications for ferumoxytol as a contrast agent in MRI*. *Journal of Magnetic Resonance Imaging*, 2015. **41**(4): p. 884-898.
5. Riedinger, A., et al., *Subnanometer local temperature probing and remotely controlled drug release based on azo-functionalized iron oxide nanoparticles*. *Nano letters*, 2013. **13**(6): p. 2399-2406.
6. Ferrari, M., *Cancer nanotechnology: opportunities and challenges*. *Nature reviews cancer*, 2005. **5**(3): p. 161-171.
7. Sun, Q., et al., *Rational design of cancer nanomedicine: nanoproperty integration and synchronization*. *Advanced materials*, 2017. **29**(14): p. 1606628.
8. Pelaz, B., et al., *Diverse applications of nanomedicine*. *ACS nano*, 2017. **11**(3): p. 2313-2381.
9. Zhu, D., et al., *Design of Disintegrable Nanoassemblies to Release Multiple Small-Sized Nanoparticles*. *Advanced Drug Delivery Reviews*, 2023: p. 114854.
10. Allen, T.M. and P.R. Cullis, *Liposomal drug delivery systems: from concept to clinical applications*. *Advanced drug delivery reviews*, 2013. **65**(1): p. 36-48.
11. Bonduelle, C., et al., *Synthesis and self-assembly of “tree-like” amphiphilic glycopolypeptides*. *Chemical communications*, 2012. **48**(67): p. 8353-8355.
12. Garnier, S. and A. Laschewsky, *New amphiphilic diblock copolymers: surfactant properties and solubilization in their micelles*. *Langmuir*, 2006. **22**(9): p. 4044-4053.
13. Anselmo, A.C. and S. Mitragotri, *Nanoparticles in the clinic: An update*. *Bioengineering & translational medicine*, 2019. **4**(3): p. e10143.
14. Feliu, N. and W.J. Parak, *Developing future nanomedicines*. *Science*, 2024. **384**(6694): p. 385-386.
15. Torchilin, V.P., *Drug targeting*. *European Journal of Pharmaceutical Sciences*, 2000. **11**: p. S81-S91.
16. Maeda, H., et al., *Tumor vascular permeability and the EPR effect in macromolecular therapeutics: a review*. *Journal of controlled release*, 2000. **65**(1-2): p. 271-284.

17. Maeda, H., et al., *Improvement of pharmacological properties of protein-drugs by tailoring with synthetic polymers*. Journal of bioactive and compatible polymers, 1988. **3**(1): p. 27-43.
18. Golombek, S.K., et al., *Tumor targeting via EPR: Strategies to enhance patient responses*. Advanced drug delivery reviews, 2018. **130**: p. 17-38.
19. Fang, J., W. Islam, and H. Maeda, *Exploiting the dynamics of the EPR effect and strategies to improve the therapeutic effects of nanomedicines by using EPR effect enhancers*. Advanced drug delivery reviews, 2020. **157**: p. 142-160.
20. Maeda, H., *Toward a full understanding of the EPR effect in primary and metastatic tumors as well as issues related to its heterogeneity*. Advanced drug delivery reviews, 2015. **91**: p. 3-6.
21. Torchilin, V.P., *Micellar nanocarriers: pharmaceutical perspectives*. Pharmaceutical research, 2007. **24**: p. 1-16.
22. Torchilin, V.P., *PEG-based micelles as carriers of contrast agents for different imaging modalities*. Advanced drug delivery reviews, 2002. **54**(2): p. 235-252.
23. Huang, X., et al., *The landscape of mRNA nanomedicine*. Nature Medicine, 2022. **28**(11): p. 2273-2287.
24. Anderson, M.L., et al., *Colloidal gold aerogels: Preparation, properties, and characterization*. Langmuir, 1999. **15**(3): p. 674-681.
25. Bratescu, M.A., et al., *Size-controlled gold nanoparticles synthesized in solution plasma*. The Journal of Physical Chemistry C, 2011. **115**(50): p. 24569-24576.
26. Bastús, N.G., J. Comenge, and V. Puntes, *Kinetically controlled seeded growth synthesis of citrate-stabilized gold nanoparticles of up to 200 nm: size focusing versus Ostwald ripening*. Langmuir, 2011. **27**(17): p. 11098-11105.
27. Polte, J.r., et al., *Mechanism of gold nanoparticle formation in the classical citrate synthesis method derived from coupled in situ XANES and SAXS evaluation*. Journal of the American Chemical Society, 2010. **132**(4): p. 1296-1301.
28. Jana, N.R., L. Gearheart, and C.J. Murphy, *Seeding growth for size control of 5–40 nm diameter gold nanoparticles*. Langmuir, 2001. **17**(22): p. 6782-6786.
29. Fenger, R., et al., *Size dependent catalysis with CTAB-stabilized gold nanoparticles*. Physical Chemistry Chemical Physics, 2012. **14**(26): p. 9343-9349.
30. Caballero-Díaz, E., et al., *The toxicity of silver nanoparticles depends on their uptake by cells and thus on their surface chemistry*. Particle & Particle Systems Characterization, 2013. **30**(12): p. 1079-1085.
31. Brandenberger, C., et al., *Quantitative evaluation of cellular uptake and trafficking of plain and polyethylene glycol-coated gold nanoparticles*. Small, 2010. **6**(15): p. 1669-1678.



32. Pelaz, B., et al., *Surface functionalization of nanoparticles with polyethylene glycol: effects on protein adsorption and cellular uptake*. ACS nano, 2015. **9**(7): p. 6996-7008.
33. Johnston, B.D., et al., *Colloidal stability and surface chemistry are key factors for the composition of the protein corona of inorganic gold nanoparticles*. Advanced Functional Materials, 2017. **27**(42): p. 1701956.
34. Qian, H., et al., *Quantum sized gold nanoclusters with atomic precision*. Accounts of chemical research, 2012. **45**(9): p. 1470-1479.
35. Nirmal, M. and L. Brus, *Luminescence photophysics in semiconductor nanocrystals*. Accounts of chemical research, 1999. **32**(5): p. 407-414.
36. Loynachan, C.N., et al., *Renal clearable catalytic gold nanoclusters for in vivo disease monitoring*. Nature nanotechnology, 2019. **14**(9): p. 883-890.
37. Rossetti, R., S. Nakahara, and L.E. Brus, *Quantum size effects in the redox potentials, resonance Raman spectra, and electronic spectra of CdS crystallites in aqueous solution*. The Journal of Chemical Physics, 1983. **79**(2): p. 1086-1088.
38. Tang, J. and R. Marcus, *Mechanisms of fluorescence blinking in semiconductor nanocrystal quantum dots*. The Journal of chemical physics, 2005. **123**(5).
39. Berger, L.I., *Semiconductor materials*. 2020: CRC press.
40. Walling, M.A., J.A. Novak, and J.R.E. Shepard, *Quantum dots for live cell and in vivo imaging*. International journal of molecular sciences, 2009. **10**(2): p. 441-491.
41. Medintz, I.L., et al., *Quantum dot bioconjugates for imaging, labelling and sensing*. Nature materials, 2005. **4**(6): p. 435-446.
42. Mirkin, C.A. and S.H. Petrosko, *Inspired Beyond Nature: Three Decades of Spherical Nucleic Acids and Colloidal Crystal Engineering with DNA*. 2023, ACS Publications.
43. García de Arquer, F.P., et al., *Semiconductor quantum dots: Technological progress and future challenges*. Science, 2021. **373**(6555): p. eaaz8541.
44. Cabral, H., et al., *Accumulation of sub-100 nm polymeric micelles in poorly permeable tumours depends on size*. Nature nanotechnology, 2011. **6**(12): p. 815-823.
45. Mitchell, M.J., et al., *Engineering precision nanoparticles for drug delivery*. Nature reviews drug discovery, 2021. **20**(2): p. 101-124.
46. Blanco, E., H. Shen, and M. Ferrari, *Principles of nanoparticle design for overcoming biological barriers to drug delivery*. Nature biotechnology, 2015. **33**(9): p. 941-951.
47. Yan, Y., et al., *Engineering particles for therapeutic delivery: prospects and challenges*. ACS nano, 2012. **6**(5): p. 3663-3669.

48. Champion, J.A. and S. Mitragotri, *Shape induced inhibition of phagocytosis of polymer particles*. *Pharmaceutical research*, 2009. **26**: p. 244-249.
49. Christian, D.A., et al., *Flexible filaments for in vivo imaging and delivery: persistent circulation of filomicelles opens the dosage window for sustained tumor shrinkage*. *Molecular pharmaceutics*, 2009. **6**(5): p. 1343-1352.
50. Huang, L., et al., *Nanoparticle Spikes Enhance Cellular Uptake via Regulating Myosin IIA Recruitment*. *ACS nano*, 2023.
51. Lundqvist, M., et al., *Nanoparticle size and surface properties determine the protein corona with possible implications for biological impacts*. *Proceedings of the National Academy of Sciences*, 2008. **105**(38): p. 14265-14270.
52. Monopoli, M.P., et al., *Physical– chemical aspects of protein corona: relevance to in vitro and in vivo biological impacts of nanoparticles*. *Journal of the American Chemical Society*, 2011. **133**(8): p. 2525-2534.
53. Wolfram, J., et al., *The nano-plasma interface: Implications of the protein corona*. *Colloids and Surfaces B: Biointerfaces*, 2014. **124**: p. 17-24.
54. Behr, J.-P., *The proton sponge: a trick to enter cells the viruses did not exploit*. *Chimia*, 1997. **51**(1-2): p. 34-34.
55. Akinc, A., et al., *Exploring polyethylenimine -mediated DNA transfection and the proton sponge hypothesis*. *The Journal of Gene Medicine: A cross-disciplinary journal for research on the science of gene transfer and its clinical applications*, 2005. **7**(5): p. 657-663.
56. Smith, M.W. and M. Gumbleton, *Endocytosis at the blood–brain barrier: from basic understanding to drug delivery strategies*. *Journal of drug targeting*, 2006. **14**(4): p. 191-214.
57. Degors, I.M., et al., *Carriers break barriers in drug delivery: endocytosis and endosomal escape of gene delivery vectors*. *Accounts of chemical research*, 2019. **52**(7): p. 1750-1760.
58. Behzadi, S., et al., *Cellular uptake of nanoparticles: journey inside the cell*. *Chemical society reviews*, 2017. **46**(14): p. 4218-4244.
59. Yameen, B., et al., *Insight into nanoparticle cellular uptake and intracellular targeting*. *Journal of controlled release*, 2014. **190**: p. 485-499.
60. Souri, M., et al., *Engineered strategies to enhance tumor penetration of drug-loaded nanoparticles*. *Journal of Controlled Release*, 2022. **341**: p. 227-246.
61. Miao, L. and L. Huang, *Exploring the tumor microenvironment with nanoparticles*. *Nanotechnology-Based Precision Tools for the Detection and Treatment of Cancer*, 2015: p. 193-226.
62. Nakamura, Y., et al., *Nanodrug delivery: is the enhanced permeability and retention effect sufficient for curing cancer?* *Bioconjugate chemistry*, 2016. **27**(10): p. 2225-2238.

63. Wolfbeis, O.S., *An overview of nanoparticles commonly used in fluorescent bioimaging*. Chemical Society Reviews, 2015. **44**(14): p. 4743-4768.
64. Erathodiyil, N. and J.Y. Ying, *Functionalization of inorganic nanoparticles for bioimaging applications*. Accounts of chemical research, 2011. **44**(10): p. 925-935.
65. Selvan, S.T., et al., *Functional and multifunctional nanoparticles for bioimaging and biosensing*. Langmuir, 2010. **26**(14): p. 11631-11641.
66. Slowing, I.I., et al., *Mesoporous silica nanoparticles for drug delivery and biosensing applications*. Advanced Functional Materials, 2007. **17**(8): p. 1225-1236.
67. Doria, G., et al., *Noble metal nanoparticles for biosensing applications*. Sensors, 2012. **12**(2): p. 1657-1687.
68. Wilczewska, A.Z., et al., *Nanoparticles as drug delivery systems*. Pharmacological reports, 2012. **64**(5): p. 1020-1037.
69. Cho, K., et al., *Therapeutic nanoparticles for drug delivery in cancer*. Clinical cancer research, 2008. **14**(5): p. 1310-1316.
70. Brigger, I., C. Dubernet, and P. Couvreur, *Nanoparticles in cancer therapy and diagnosis*. Advanced drug delivery reviews, 2012. **64**: p. 24-36.
71. Petros, R.A. and J.M. DeSimone, *Strategies in the design of nanoparticles for therapeutic applications*. Nature reviews Drug discovery, 2010. **9**(8): p. 615-627.
72. Lucky, S.S., K.C. Soo, and Y. Zhang, *Nanoparticles in photodynamic therapy*. Chemical reviews, 2015. **115**(4): p. 1990-2042.
73. Lu, J., et al., *Biocompatibility, biodistribution, and drug -delivery efficiency of mesoporous silica nanoparticles for cancer therapy in animals*. Small, 2010. **6**(16): p. 1794-1805.
74. Lademann, J., et al., *Nanoparticles—an efficient carrier for drug delivery into the hair follicles*. European Journal of Pharmaceutics and Biopharmaceutics, 2007. **66**(2): p. 159-164.
75. Sur, S., et al., *Recent developments in functionalized polymer nanoparticles for efficient drug delivery system*. Nano-Structures & Nano-Objects, 2019. **20**: p. 100397.
76. Zhang, B., et al., *Human serum albumin-based doxorubicin prodrug nanoparticles with tumor pH-responsive aggregation-enhanced retention and reduced cardiotoxicity*. Journal of materials chemistry B, 2020. **8**(17): p. 3939-3948.
77. Gros, F. and S. Muller, *The role of lysosomes in metabolic and autoimmune diseases*. Nature Reviews Nephrology, 2023. **19**(6): p. 366-383.
78. Zhang, C., et al., *Enzyme-responsive peptide dendrimer-gemcitabine conjugate as a controlled-release drug delivery vehicle with enhanced antitumor efficacy*. Acta biomaterialia, 2017. **55**: p. 153-162.

79. Yang, Y., et al., *Drug conjugate-based anticancer therapy-Current status and perspectives*. Cancer Letters, 2023. **552**: p. 215969.
80. Cun, X., et al., *A novel strategy through combining iRGD peptide with tumor-microenvironment-responsive and multistage nanoparticles for deep tumor penetration*. ACS applied materials & interfaces, 2015. **7**(49): p. 27458-27466.
81. Bernkop-Schnürch, A., *Strategies to overcome the polycation dilemma in drug delivery*. Advanced drug delivery reviews, 2018. **136**: p. 62-72.
82. Sun, Q., et al., *Integration of nanoassembly functions for an effective delivery cascade for cancer drugs*. Advanced materials, 2014. **26**(45): p. 7615-7621.
83. Xu, P., et al., *Shrapnel nanoparticles loading docetaxel inhibit metastasis and growth of breast cancer*. Biomaterials, 2015. **64**: p. 10-20.
84. Xiong, X., et al., *A NIR light triggered disintegratable nanoplatform for enhanced penetration and chemotherapy in deep tumor tissues*. Biomaterials, 2020. **245**: p. 119840.
85. Hühn, J., et al., *Selected standard protocols for the synthesis, phase transfer, and characterization of inorganic colloidal nanoparticles*. Chemistry of Materials, 2017. **29**(1): p. 399-461.
86. Weng, B., et al., *Stabilizing ultrasmall Au clusters for enhanced photoredox catalysis*. Nature communications, 2018. **9**(1): p. 1543.
87. Skirtach, A.G., A.M. Yashchenok, and H. Möhwald, *Encapsulation, release and applications of LbL polyelectrolyte multilayer capsules*. Chemical Communications, 2011. **47**(48): p. 12736-12746.
88. Soldan, G., et al., *Gold doping of silver nanoclusters: a 26-Fold enhancement in the luminescence quantum yield*. Angewandte Chemie, 2016. **128**(19): p. 5843-5847.
89. Šikalo, Š., et al., *Dynamic contact angle of spreading droplets: Experiments and simulations*. Physics of Fluids, 2005. **17**(6).
90. Mansfield, E., A. Kar, and S.A. Hooker, *Applications of TGA in quality control of SWCNTs*. Analytical and bioanalytical chemistry, 2010. **396**: p. 1071-1077.
91. Mansfield, E., et al., *Determination of nanoparticle surface coatings and nanoparticle purity using microscale thermogravimetric analysis*. Analytical chemistry, 2014. **86**(3): p. 1478-1484.
92. Wilhelm, S., et al., *Water dispersible upconverting nanoparticles: effects of surface modification on their luminescence and colloidal stability*. Nanoscale, 2015. **7**(4): p. 1403-1410.
93. Ganas, C., et al., *Biodegradable capsules as non-viral vectors for in vitro delivery of PEI/siRNA polyplexes for efficient gene silencing*. Journal of Controlled Release, 2014. **196**: p. 132-138.

94. Ashraf, S., et al., *Zwitterionic surface coating of quantum dots reduces protein adsorption and cellular uptake*. *Nanoscale*, 2016. **8**(41): p. 17794-17800.
95. Ma, X., et al., *Colloidal gold nanoparticles induce changes in cellular and subcellular morphology*. *ACS nano*, 2017. **11**(8): p. 7807-7820.
96. Kulkarni, S.A. and S.-S. Feng, *Effects of particle size and surface modification on cellular uptake and biodistribution of polymeric nanoparticles for drug delivery*. *Pharmaceutical research*, 2013. **30**: p. 2512-2522.
97. Rana, S., et al., *Folic acid conjugated Fe<sub>3</sub>O<sub>4</sub> magnetic nanoparticles for targeted delivery of doxorubicin*. *Dalton Transactions*, 2016. **45**(43): p. 17401-17408.
98. Lazaro, I.A., et al., *Selective surface PEGylation of UiO-66 nanoparticles for enhanced stability, cell uptake, and pH-responsive drug delivery*. *Chem*, 2017. **2**(4): p. 561-578.
99. Liang, M., et al., *Cellular uptake of densely packed polymer coatings on gold nanoparticles*. *ACS nano*, 2010. **4**(1): p. 403-413.
100. Peng, Q., et al., *Mechanisms of phospholipid complex loaded nanoparticles enhancing the oral bioavailability*. *Molecular pharmaceutics*, 2010. **7**(2): p. 565-575.
101. Kettler, K., et al., *Cellular uptake of nanoparticles as determined by particle properties, experimental conditions, and cell type*. *Environmental toxicology and chemistry*, 2014. **33**(3): p. 481-492.
102. He, C., et al., *Effects of particle size and surface charge on cellular uptake and biodistribution of polymeric nanoparticles*. *Biomaterials*, 2010. **31**(13): p. 3657-3666.
103. Pouton, C.W., et al., *Polycation-DNA complexes for gene delivery: a comparison of the biopharmaceutical properties of cationic polypeptides and cationic lipids*. *Journal of controlled release*, 1998. **53**(1-3): p. 289-299.
104. Yang, S., et al., *Cellular uptake of self-assembled cationic peptide-DNA complexes: multifunctional role of the enhancer chloroquine*. *Journal of Controlled Release*, 2009. **135**(2): p. 159-165.
105. Slowing, I.I., et al., *Mesoporous silica nanoparticles as controlled release drug delivery and gene transfection carriers*. *Advanced drug delivery reviews*, 2008. **60**(11): p. 1278-1288.
106. Kessler, R., *Engineered nanoparticles in consumer products: understanding a new ingredient*. 2011, National Institute of Environmental Health Sciences.
107. Kim, J., Y. Piao, and T. Hyeon, *Multifunctional nanostructured materials for multimodal imaging, and simultaneous imaging and therapy*. *Chemical Society Reviews*, 2009. **38**(2): p. 372-390.

108. Stark, W.J., *Nanoparticles in biological systems*. Angewandte Chemie International Edition, 2011. **50**(6): p. 1242-1258.
109. Su, Y., et al., *Design strategies and applications of circulating cell-mediated drug delivery systems*. ACS biomaterials science & engineering, 2015. **1**(4): p. 201-217.
110. Chen, B., et al., *Current multistage drug delivery systems based on the tumor microenvironment*. Theranostics, 2017. **7**(3): p. 538.
111. Scicluna, M.C. and L. Vella-Zarb, *Evolution of nanocarrier drug-delivery systems and recent advancements in covalent organic framework–drug systems*. ACS Applied Nano Materials, 2020. **3**(4): p. 3097-3115.
112. Kim, J.S., et al., *Imaging of transient structures using nanosecond in situ TEM*. Science, 2008. **321**(5895): p. 1472-1475.
113. Willets, K.A., *Surface-enhanced Raman scattering (SERS) for probing internal cellular structure and dynamics*. Analytical and bioanalytical chemistry, 2009. **394**: p. 85-94.
114. de Jonge, N., et al., *Resolution and aberration correction in liquid cell transmission electron microscopy*. Nature Reviews Materials, 2019. **4**(1): p. 61-78.
115. Ross, F.M., *Opportunities and challenges in liquid cell electron microscopy*. Science, 2015. **350**(6267): p. aaa9886.
116. Lechene, C., et al., *High-resolution quantitative imaging of mammalian and bacterial cells using stable isotope mass spectrometry*. Journal of biology, 2006. **5**: p. 1-30.
117. Rao, J., A. Dragulescu-Andrasi, and H. Yao, *Fluorescence imaging in vivo: recent advances*. Current opinion in biotechnology, 2007. **18**(1): p. 17-25.
118. Emptage, N.J., *Fluorescent imaging in living systems*. Current opinion in pharmacology, 2001. **1**(5): p. 521-525.
119. Maška, M., et al., *The Cell Tracking Challenge: 10 years of objective benchmarking*. Nature Methods, 2023. **20**(7): p. 1010-1020.
120. Watson, P., A.T. Jones, and D.J. Stephens, *Intracellular trafficking pathways and drug delivery: fluorescence imaging of living and fixed cells*. Advanced drug delivery reviews, 2005. **57**(1): p. 43-61.
121. Stewart, M.D., et al., *Dual fluorescent protein reporters for studying cell behaviors in vivo*. genesis, 2009. **47**(10): p. 708-717.
122. Liedl, T., et al., *Fluorescent nanocrystals as colloidal probes in complex fluids measured by fluorescence correlation spectroscopy*. Small, 2005. **1**(10): p. 997-1003.
123. Carrillo-Carrion, C., et al., *Taking Advantage of Hydrophobic Fluorine Interactions for Self-Assembled Quantum Dots as a Delivery Platform for Enzymes*. Angewandte Chemie International Edition, 2018. **57**(18): p. 5033-5036.

124. Dahan, M., P. Alivisatos, and W.J. Parak, *Quantum Dots: Inorganic Fluorescent Probes for Single-Molecule Tracking Experiments in Live Cells*, in *Single Particle Tracking and Single Molecule Energy Transfer*. 2009, Wiley Online Library. p. 67-96.
125. Carrillo-Carrion, C., et al., *Triple-labeling of polymer-coated quantum dots and adsorbed proteins for tracing their fate in cell cultures*. ACS nano, 2019. **13**(4): p. 4631-4639.
126. Peng, X., et al., *Shape control of CdSe nanocrystals*. Nature, 2000. **404**(6773): p. 59-61.
127. Peng, Z.A. and X. Peng, *Mechanisms of the shape evolution of CdSe nanocrystals*. Journal of the American Chemical Society, 2001. **123**(7): p. 1389-1395.
128. Zhou, J., et al., *Ideal CdSe/CdS core/shell nanocrystals enabled by entropic ligands and their core size-, shell thickness-, and ligand-dependent photoluminescence properties*. Journal of the American Chemical Society, 2017. **139**(46): p. 16556-16567.
129. Pereira, M.I.A., et al., *Resazurin-based assay to evaluate cell viability after quantum dot interaction*. Quantum Dots: Applications in Biology, 2020: p. 213-221.
130. Yusof, N.S.M. and M. Ashokkumar, *Ultrasonic transformation of micelle structures: Effect of frequency and power*. Ultrasonics sonochemistry, 2015. **24**: p. 8-12.
131. Feng, M., et al., *Highly erbium-doped nanoplatform with enhanced red emission for dual-modal optical-imaging-guided photodynamic therapy*. Inorganic Chemistry, 2018. **57**(23): p. 14594-14602.
132. Chen, X., et al., *Photon upconversion in core-shell nanoparticles*. Chemical Society Reviews, 2015. **44**(6): p. 1318-1330.
133. Han, S., et al., *Enhancing luminescence in lanthanide-doped upconversion nanoparticles*. Angewandte Chemie International Edition, 2014. **53**(44): p. 11702-11715.

## **Eidesstattliche Versicherung/Declaration on Oath**

Hiermit versichere ich an Eides statt, die vorliegende Dissertationsschrift selbst verfasst und keine anderen als die angegebenen Hilfsmittel und Quellen benutzt zu haben.

Hamburg. 02.05.2024

Miso Feng